institut für
theoretische physik

Influence of Time Delayed Feedback on the Dynamics of Temporal Localized Structures

Master Thesis

Submitted by

Thomas Seidel

September 20, 2020

First examiner: *Priv.-Doz. Dr. Svetlana Gurevich*

Second examiner: *Prof. Dr. Julien Javaloyes*

Westfälische Wilhelms-Universität Münster
Fachbereich Physik
Institut für theoretische Physik

Contents

1. Introduction

Localized structures (LSs) have been observed in a wide variety of systems in nature such as water waves [WKR84; MFS87], vegetation patterns [Mer+04], semiconductor devices [Nie+92], as plasma spots of gas discharge systems [AP01], in vibrated granular materials [UMS96] and optics [AA05; Sei+20], just to mention a few. These structures are considered to be localized as their correlation range is much shorter than the size of the system. LSs can either be *dissipative* or *conservative* depending on the specific system in which they occur. In contrast with the conservative case, in which a given set of parameters for the governing propagation equation generally leads to an infinite number of soliton solutions, the attractor in a dissipative system is a fixed localized solution [GA12].

This thesis addresses dissipative LSs found in the output of a *mode-locked* (ML) laser which can generate ultra short pulses with high repetition rates [Hau00]. There are applications in a wide variety of field including optical data communication, optical clocking, metrology, medical imaging and surgery [TEK88; DHA91; Loe+96; UHH02; Kel03]. Semiconductor ML lasers are of particular interest, especially for telecommunications applications [Bim+06; Kun+07], as they are relatively easy to manufacture, have a small footprint, are integrable and can be electrically pumped [Jau16].

Localization of states can occur in different forms, namely temporal [SJG18], spatial [Nie+92], topological [Mad+19] and vectorial [Pes+04]. Temporal and spatial LSs can be analyzed in similar frameworks. However, an important difference is that space is usually symmetrical, i.e., shows a left-right/up-down symmetry. Due to spontaneous symmetry breaking, spatial LSs can move in the symmetrical domain. On the other hand, temporal dynamics is not symmetrical and thus shows a parity symmetry breaking before-after the passing of a pulse. This is because when a pulse passes, it depletes the active material gain that only recovers on a given time scale as discussed in [Jav+16]. The pulses analyzed in this thesis are temporal LSs.

1.1. The Principle of Mode-Locking

ML can usually be achieved by two different techniques: *active mode-locking* (AML) and *passive mode-locking* (PML). In lasers with AML the losses or the pump current are modulated and the frequency is chosen such that it is resonant

with the modes of laser cavity [Hau00]. This approach leads to a very regular train of pulses, however, the pulse width is limited by the speed of the external modulator.

Shorter pulses can be achieved by using PML lasers. They consist of a laser amplifier providing gain and a nonlinear loss element, typically a saturable absorber. There are also PML techniques that do not involve a saturable absorber. For example in [Jav+07] a mode-locking technique that utilises the polarisation degrees of freedom of light is discussed. In the typical setup, the gain and absorber elements are placed inside of the optical cavity as shown in fig. 1.1. The gain section is electrically pumped, thereby generating an inversion of charge carriers, and the absorber section has a reverse bias applied to it [Der+92]. In order to understand how PML achieves pulsed emission, it is helpful to consider the evolution of the electric field of a pulse, the gain and the losses [Jau16], which is displayed in fig. 1.2. In most of the cavity when there is no pulse, the losses (green dashed-dotted line) are higher than the gain (red dashed line). This means that there are net losses and the electric field (blue lien) is not amplified. When a pulse arrives, both the gain and the loss get depleted. For the leading edge of the pulse there are still net losses so that the pulse gets shortened. However, the loss element gets depleted faster than the gain which opens a window of amplification marked with shadowed regions in fig. 1.2. Therefore, the center of the pulse gets amplified. The trailing edge of the pulse gets damped as the loss section recovers faster than the gain so that there are net losses again.

1.2. Time Delayed Feedback

Time delayed feedback is one of the widely used techniques to control the behavior of dynamical systems [SKH16]. Besides optical systems [SL93; LK80], applications can be found in, e.g., electronics [Jus+00] and neuroscience [RP04], among others. With regard to PML lasers, time delayed feedback can be used to produce more regular patterns and stabilize certain states of the system [SL93]. However, a system with time delayed feedback exhibits more degrees of freedom and as a consequence, the dynamics can become more complex compared to the original system. This can lead, e.g., to the formation of complex temporal patterns [YG14].

Figure (1.1) shows a schematic setup of a PML laser with time delayed feedback. In the main cavity of length τ_1 a gain and saturable absorber elements are placed.

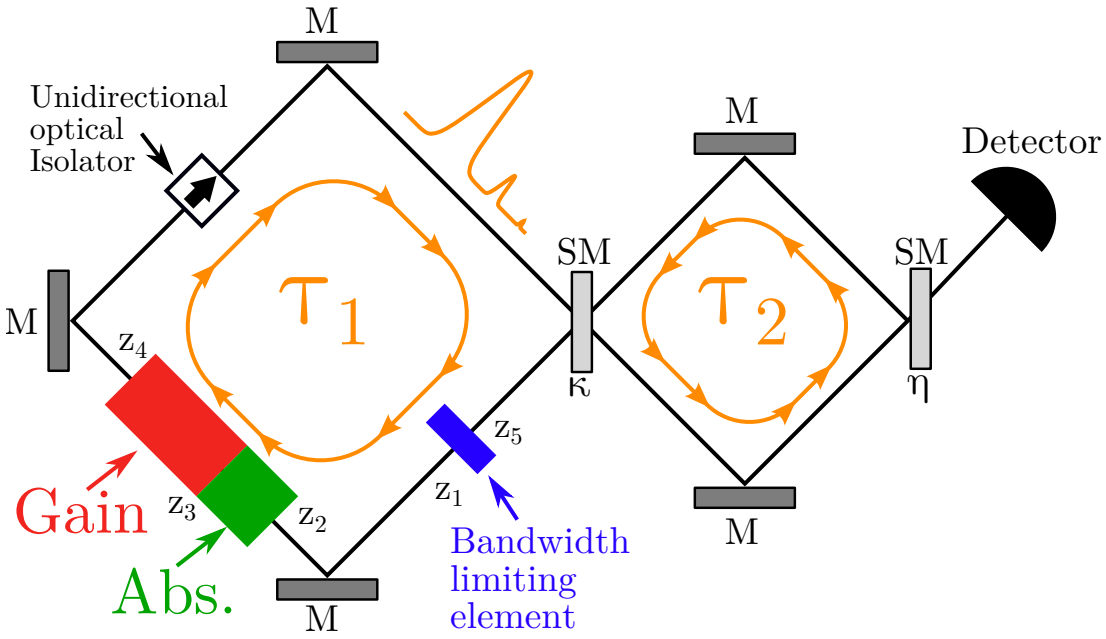

Figure 1.1: Schematic sketch of the experimental setup. It consists of two cavities with round-trip times τ_1 and τ_2, respectively, which are depicted as squares confined by mirrors (M). The length of the cavities L_i are proportional to the round-trip times τ_i via $L_i = c\tau_i$ where c is the speed of light. Therefore, τ_i is also referred to as the length of the respective cavity. In the main cavity of length τ_1 a gain and a saturable absorber sections are placed, in which optical pulses are created via passive mode-locking. The unidirectional optical isolator ensures that the pulses only propagate in one direction. The bandwidth limiting element ensures that only certain laser modes are amplified as others are suppressed. The markers z_1-z_5 denote the endpoint (or starting point) of each section in the main cavity. The two cavities are connected by a semitransparent mirror (SM) which reflects a fraction of $\sqrt{\kappa}$ of the electric field. In the second cavity τ_2 a semitransparent mirror with reflectivity η is placed, i.e., a fraction of η of the optical power is fed back into the main cavity τ_1. The rest of the optical power leaves the setup and can be detected by the detector. Note that τ_2 does not necessarily need to be smaller than τ_1.

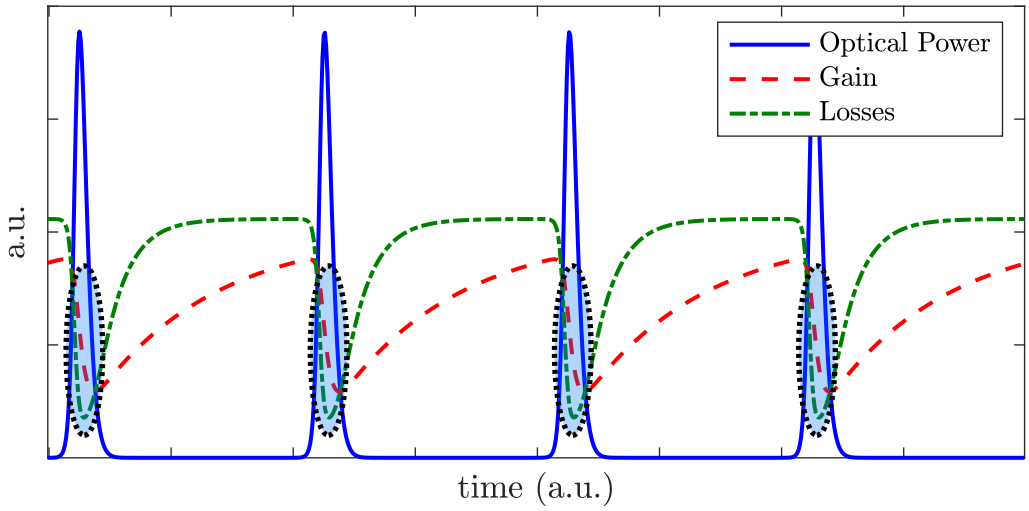

Figure 1.2: Schematic of the time evolution of the (blue) electric field, (red dashed) gain and (green dashed-dotted) losses in a passively mode-locked semiconductor laser. Inside the windows of amplification, marked by the shadowed dotted ovals, the gain is higher than the losses such that the center of the pulse gets amplified. The edges of the pulses are shortened by the dominant losses.

For specific gain and absorber parameters and in the regime in which the gain recovery time is much shorter than the round-trip time τ_1, the so-called *long cavity regime*, the pulses become temporal LSs which can be individually addressed and modified to generate almost arbitrary pulse patterns [Mar+14]. The bandwidth limiting element ensures that only certain laser modes are amplified as others are suppressed. The unidirectional optical isolator prevents the electric field from propagating in different directions such that interferences of forward and backward moving fields do not need to be considered. After each round-trip a fraction of κ of the intensity remains in the main cavity. This is realized with a semitransparent mirror (SM). The time delayed feedback is implemented by an additional loop of length τ_2. It feeds a fraction of η of the electric field back into the main cavity.

1.3. Outline

The thesis is structured as follows. First, a brief theoretical background on dynamical systems, bifurcation theory and the numerical methods used in this thesis is given in chapter 2. Next, in chapter 3, a model describing the dynamics of a PML laser with time delayed feedback is presented. This chapter also includes a

derivation of the mathematical description of the dynamics in form of delayed differential equations. In the following chapter 4, this model will be analyzed using numerical path continuation and direct numerical simulations (DNS). In particular, the influence of the feedback rate, the feedback delay and the linewidth enhancement factors on the dynamics of LSs are studied in detail. In the end of this chapter, LSs consisting of multiple pulses – so-called harmonic solutions – are introduced. It is analyzed how the system behaves when a satellite pulse created by time delayed feedback is placed close to a main pulse. Harmonic solutions are also the main focus of chapter 5 where it is investigated how time delayed feedback can be used to create trains of coherent pulses. This is done in a statistical analysis where also the influence of noise is studied. A summary of the thesis along with a discussion of open questions and possible direction of future work is given in chapter 6.

2. Theoretical Preliminaries

The following chapter shall introduce the basic theoretical concepts used in this thesis. Further, some analytical methods are presented.

2.1. Complex Systems with Delay

Many phenomena observed in nature and lab experiments can be described by *complex systems*. Their dynamics are governed by *dynamical systems* which model the temporal evolution of certain quantities. Dynamical systems are grouped into different classes depending on whether time is discrete or continuous and whether the systems are spatially extended [Thi18]. In all cases, $\boldsymbol{x}(t)$ is a n-dimensional vector which defines the state of the system at time t. The following dynamical systems are based on *initial value problems* where the state at a given point in time t_0 needs to be given. For *iterative maps*, time is a discrete variable at points $t_n,\ n = \mathbb{N}$ and $\boldsymbol{x}_n := \boldsymbol{x}(t_n)$ consists of n discrete variables. For a given state $\boldsymbol{x}_0$, one obtains all states at later times by the map

$$\boldsymbol{x}_{n+1} = \boldsymbol{F}(\boldsymbol{x}_n, t_n). \tag{2.1}$$

Next, for *continuous dynamical systems* time is continuous and $\boldsymbol{x}_i,\ i = 1, ...n$ describes discrete variables. The dynamics are described by n first order *ordinary differential equations* (ODEs)

$$\dot{\boldsymbol{x}} = \boldsymbol{F}(\boldsymbol{x}, t). \tag{2.2}$$

Last, *spacially extended systems* are continuous in time and in space, i.e. $\boldsymbol{x}(\boldsymbol{r}, t)$, $r \in \mathbb{R}^d, d \in \mathbb{N}^+$ is a field. The time evolution is defined by n first order *partial differential equations* (PDEs)

$$\dot{\boldsymbol{x}} = \boldsymbol{D}(\boldsymbol{x}, t) \tag{2.3}$$

where $\boldsymbol{D}$ is a differential operator (or integro-differential operator), e.g., ∇^k, $\int \nabla^n$. However, when modeling real world systems, it is often necessary to consider the state of the system in the past, e.g., due to finite propagation times of the signals. This aspect is respected in the class of the so-called *delay-differential equations*

(DDEs). Formally, a DDE can be written as

$$\dot{\boldsymbol{x}} = \boldsymbol{F}(\boldsymbol{x}(t), \boldsymbol{x}(t-\tau_1), ..., \boldsymbol{x}(t-\tau_m), t) \tag{2.4}$$

for a system which depends on m delays $\tau_1, ..., \tau_m$. In more complex situations even state depended delays $\tau(\boldsymbol{x})$ are possible. An important consequence of the delay is, that initial conditions in eq. (2.4) cannot be regarded as points in the finite dimensional phase space but as functions in the interval $[-\max(\tau_1, ..., \tau_m), t_0)$. These can be seen as points in the infinite-dimensional phase space and eq. (2.4) describes their evolution. It is intuitive that for very small time delays the system behaves essentially like a finite-dimensional system or speaking formally $\boldsymbol{x}(t)$ approaches a certain finite-dimensional attractor or manifold [YG17].

2.2. The Concept of Pseudo-Space-Time

When considering long-delay systems, an important observation is that the time evolution is often periodic with the period $\tau+\delta$, where τ is the delay and δ defines a certain drift [YG17]. A typical time trace of a periodic signal as a solution of a DDE is presented in fig. 2.1. In order to better visualize the evolution of the whole period over the time span of many periods it makes sense to introduce the concept of *pseudo-space-time*. The idea is to interpret the solution of one period of the system as one dimensional "space". Then, the time trace can be cut into slices, each having the length of one period. These slices are called *round-trips*. In fig. 2.1 it can be seen, that the period of the periodic solution is approximately τ_1. The evolution then can be tracked in a space-time-like-diagram such as fig. 2.2a where each column stands for the time span of τ_1 of the time trace in fig. 2.1. This is emphasized by the inset which shows the profile along the dashed white line in fig. 2.2a. However, a residual drift can be observed which indicates that the period differs slightly from τ_1. The exact period can be computed using the autocorrelation-function of the time trace. The distance between peaks in the autocorrelated signal corresponds to the period T. Applying this method to the time trace shown in fig. 2.1 reveals that the period is $T = 100.04$ which is slightly larger than $\tau_1 = 100$. Plotting the corresponding pseudo-space-time-diagram (see fig. 2.2b) shows that the periodic solution does not change over the course of several round-trips and thus is periodic with the period $T = 100.04$.

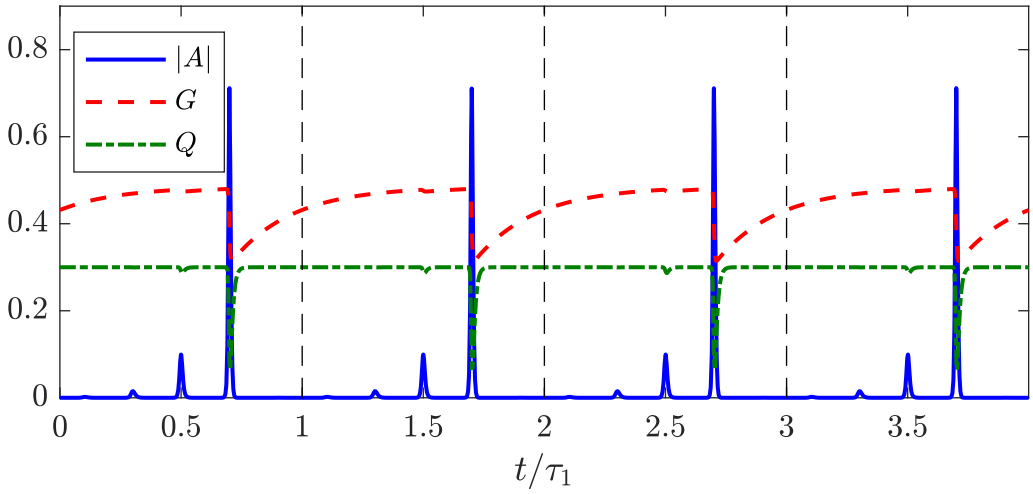

Figure 2.1: An exemplary periodic signal obtained from a DNS of the model presented in section 3. Time is normalized to τ_1 as the solution has a periodicity of approximately τ_1 as indicated by the black vertical dashed lines.

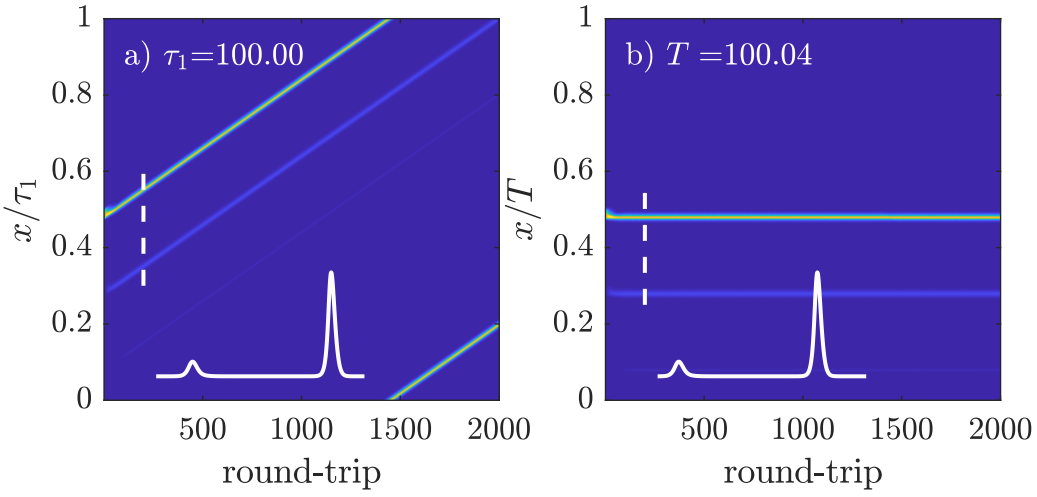

Figure 2.2: Pseudo-space-time-representation of the time trace shown in fig. 2.1. The time trace is split into slices of length a) of delay $\tau_1 = 100$ and b) of period $T = 100.04$, respectively. Each slice corresponds to one column in the space-time-representation and can be interpreted as one-dimensional pulse space. This is emphasized by the insets which show the profiles along the dashed white lines.

2.3. Linear Stability Analysis

An important aspect in the analysis of dynamical systems is to determine the stability of solutions, i.e., to find out whether small perturbations to a state are damped by the system or grow and thus destroy the state. First, the influence of delay on the linear stability analysis of fixed points is presented and next, it is deduced how to determine the stability of periodic solutions.

2.3.1. Linear Stability of Fixed Points

In the vicinity of a solution $\boldsymbol{s}(t)$ of a DDE $\dot{\boldsymbol{x}} = F(\boldsymbol{x}(t), \boldsymbol{x}(t-\tau))$ this system can be linearized. Thus, the ansatz $\boldsymbol{x}(t) = \boldsymbol{s}(t) + \boldsymbol{\delta}(t)$ is used where $\boldsymbol{\delta}(t)$ is a small perturbation to the system. This yields

$$\begin{aligned}
\frac{d}{dt}(\boldsymbol{s}(t) + \boldsymbol{\delta}(t)) &= \boldsymbol{F}(\boldsymbol{s}(t) + \boldsymbol{\delta}(t), \boldsymbol{s}(t-\tau) + \boldsymbol{\delta}(t-\tau)) && (2.5)\\
&= \boldsymbol{F}(\boldsymbol{s}(t), \boldsymbol{s}(t-\tau)) + \boldsymbol{A}(t)\boldsymbol{\delta}(t) + \boldsymbol{B}(t)\boldsymbol{\delta}(t-\tau) + \text{h.o.t.} && (2.6)\\
\Leftrightarrow\ \dot{\boldsymbol{\delta}} &= \boldsymbol{A}(t)\boldsymbol{\delta}(t) + \boldsymbol{B}(t)\boldsymbol{\delta}(t-\tau) + \text{h.o.t.} && (2.7)
\end{aligned}$$

where $\boldsymbol{A}(t) = \partial_1 \boldsymbol{F}(\boldsymbol{s}(t), \boldsymbol{s}(t-\tau))$ and $\boldsymbol{B}(t) = \partial_2 \boldsymbol{F}(\boldsymbol{s}(t), \boldsymbol{s}(t-\tau))$ are the Jacobians of $\boldsymbol{F}$ with respect to the first and the second argument evaluated at $\boldsymbol{s}(t)$ and $\boldsymbol{s}(t-\tau)$, respectively. In the easiest case the solution $\boldsymbol{s}(t)$ is stationary, i.e., time independent: $\boldsymbol{s}(t) = \boldsymbol{s_0}$. Such a solution is called *fixed point*. Then $\boldsymbol{A}$ and $\boldsymbol{B}$ are stationary as well. Further, the perturbation is given by an exponential function $\boldsymbol{\delta} = \boldsymbol{\epsilon} e^{\lambda t}$, $|\boldsymbol{\epsilon}| \ll 1$, which leads to the characteristic equation of the corresponding eigenvalue problem for λ

$$\det[-\lambda \mathbb{1} + \boldsymbol{A} + \boldsymbol{B} e^{-\lambda\tau}] = 0. \tag{2.8}$$

Equation (2.8) is transcendental, which, in general, possesses infinite number of complex nods which are called *eigenvalues* [YG17]. The fact that DDEs are of infinite-dimension can be seen at this point in the infinite number of eigenvalues. However, according to [Hal77] they are bound, i.e., $\mathrm{Re}(\lambda) < C\ \forall\lambda$, and accumulate solely at $-\infty$. Thus, in general, only a finite number of eigenvalues determines the linear stability of the solution. Further, the majority of eigenvalues lies on curves in the complex plane [LWY11] and the distance between the eigenvalues on these curves scales as $2\pi/\tau$ [YG17]. Hence, the longer the delay, the smaller the

distance between the eigenvalues on the curve and the more eigenvalues determine the stability. In contrast, in the limit of short delays, the system behaves as an ODE which is shown in the infinite distance between eigenvalues. Note that this derivation focused on systems with a single delay, however the same approach can be used if multiple delays are present.

2.3.2. Linear Stability of Periodic Solutions

This section follows the derivation of [Arg+15]. In complex systems with delay periodic solutions are common to occur. Therefore, it is important to look at how to determine their stability. The theoretical framework is provided by the *Floquet theory*. Again, one regards a perturbation $\boldsymbol{\delta}(t)$ of small magnitude to a solution $\boldsymbol{s}(t)$ of the dynamical system $\dot{\boldsymbol{x}} = \boldsymbol{F}(\boldsymbol{x})$. Here, assume that the solution is periodic with period T, i.e., $\boldsymbol{s}(t) = \boldsymbol{s}(t+T)$. Note that the theory does not fully exists for DDEs but the characteristic properties are defined similarly [Jau16]. In order to analyze DDEs one needs to discretize time for the length of the delay. The corresponding state vector then reads $\boldsymbol{y}(t) = (\boldsymbol{x}(t), \boldsymbol{x}(t-\delta_1), ..., \boldsymbol{x}(t-\delta_n), \boldsymbol{x}(t-\tau))$ where $0 < \delta_i < \delta_{i+1} < \tau \ \forall i = 1, ..., n$ for n discretization points. The equations of motion need to be rewritten accordingly. Thus, for simplification an autonomous system without delay is regarded. Using this ansatz $\boldsymbol{x}(t) = \boldsymbol{s}(t) + \boldsymbol{\delta}(t)$ yields

$$\begin{aligned} \dot{\boldsymbol{s}}(t) + \dot{\boldsymbol{\delta}}(t) &= \boldsymbol{F}(\boldsymbol{s}(t) + \boldsymbol{\delta}(t)) \\ &= \boldsymbol{F}(\boldsymbol{s}(t)) + \underbrace{\left.\frac{\partial \boldsymbol{F}(\boldsymbol{x}(t))}{\partial \boldsymbol{x}}\right|_{\boldsymbol{s}(t)}}_{=:\boldsymbol{D}(t)} \boldsymbol{\delta}(t) + \text{h.o.t.} \qquad (2.9) \\ \Leftrightarrow \ \dot{\boldsymbol{\delta}}(t) &= \boldsymbol{D}(t)\boldsymbol{\delta}(t). \qquad (2.10) \end{aligned}$$

Here, $\boldsymbol{D}(t)$ is a matrix with periodic coefficients and it possesses the same period T as the solution $\boldsymbol{s}(t)$. Now, the idea is to use the periodicity of $\boldsymbol{D}(t)$ which provides a reduction to a system with constant coefficients. This can be done, by looking at the system at discrete points in time $t = 0, T, 2T, 3T, ...$ and checking whether perturbations grow or fade away. Geometrically, this corresponds to a Poincaré section. Thus, the corresponding Poincaré map provides the stability information of the system.

In order to find the Poincaré map the fundamental solutions $\boldsymbol{\varphi}_i, \ i = 1, ..., n$

(where n is the dimension of the system) of the linearized system eq. (2.10) need to be found. Each state of the system can be created by a superposition of the fundamental solutions:

$$\begin{aligned} \boldsymbol{x}(t) &= c_1\boldsymbol{\varphi}_1(t) + ... + c_n\boldsymbol{\varphi}_n(t) \\ &= \boldsymbol{\Phi}(t)\boldsymbol{c}, \end{aligned} \tag{2.11}$$

where $\boldsymbol{\phi}(t) = [\boldsymbol{\varphi}_1(t) \ ... \ \boldsymbol{\varphi}_n(t)]$ and $\boldsymbol{c} = [c_1, ..., c_n]$. The fundamental solution $\boldsymbol{\varphi}_i$ shall be normalized such that the initial condition lies on a n-dimensional hypersphere of radius 1. Mathematically, this means

$$\boldsymbol{\Phi}(0) = \mathbb{1}. \tag{2.12}$$

For each solution $\boldsymbol{x}(t)$, $\boldsymbol{x}(t+T)$ also is a solution and thus can be represented by the system of fundamental solutions. Hence, one can establish a constant $n \times n$-matrix $\boldsymbol{C}$ with

$$\boldsymbol{\Phi}(t+T) = \boldsymbol{\Phi}(t)\boldsymbol{C}, \tag{2.13}$$

i.e., $\boldsymbol{C}$ maps $\boldsymbol{\Phi}(t)$ onto $\boldsymbol{\Phi}(t+T)$ and thus describes a Poincaré map. Using eq. (2.12) yields

$$\boldsymbol{\Phi}(T) = \boldsymbol{\Phi}(0)\boldsymbol{C} = \boldsymbol{C}. \tag{2.14}$$

This determines $\boldsymbol{C}$ which is called the *monodromy matrix*. Geometrically, this means that initially the fundamental solutions lie on a unit hypersphere and after one revolution this hypersphere is deformed into an ellipsoid which semi-axes correspond to the eigenvalues λ_i of the monodromy matrix. These are called *Floquet multipliers*. If all Floquet multipliers satisfy $|\lambda_i| < 1 \ \forall i = 1, ..., n$, the ellipsoid lies within the unit hypersphere and the perturbations will fade away over time. On the other hand, if $|\lambda_i| > 1$ for at least one $i = 1, ..., n$ the system is unstable and perturbations will grow in time. Note that each autonomous system has at least one Floquet multiplier $\exists i : \lambda_i = 1$ belonging to the translation along the periodic orbit. Generally, the monodromy matrix cannot be found analytically, however numerically it can be determined if eq. (2.10) is integrated over one period. Remember that a system with delay is of infinite dimension and

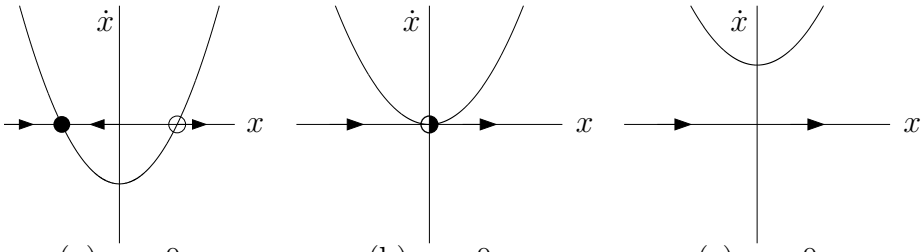

(a) $r < 0$ (b) $r = 0$ (c) $r > 0$

Figure 2.3: Phase diagram of eq. (2.15) for different values of the control parameter r. The circles highlight fixed points. A filled circle stands for a stable, an empty one for an unstable and a half filled for a metastable fixed point. The arrows indicate the direction of the velocity field.

thus the number of Floquet multipliers is infinite as well. Hence, one generally uses numerically methods to determine the Floquet multipliers which limits the number of Floquet multipliers to the number of discretization points.

2.4. Bifurcations of Fixed Points

A bifurcation occurs when a small change to a system parameter (the control parameter) causes a qualitative change in the system's behavior meaning that the stability of a fixed point changes. This can occur when different fixed points collide or when new attractors such as limit cycles emerge. The results of a bifurcation analysis can be summarized in a *bifurcation diagram* where the control parameter is plotted against a norm which defines the state of the system. All systems exhibiting a certain type of bifurcation are locally (around the equilibrium) topologically equivalent to the normal form of the bifurcation [Str94]. In the following, several local bifurcation types important for this thesis are presented.

2.4.1. Saddle-Node Bifurcation

In a *saddle-node bifurcation* (or *fold bifurcation*), a stable and an unstable solution annihilate at the bifurcation point. The normal form of a saddle-node bifurcation is given by

$$\dot{x} = x^2 + \mu, \tag{2.15}$$

where μ is a control parameter. Depending on the value of μ, three cases occur, which are visualized in the phase diagrams in fig. 2.3.

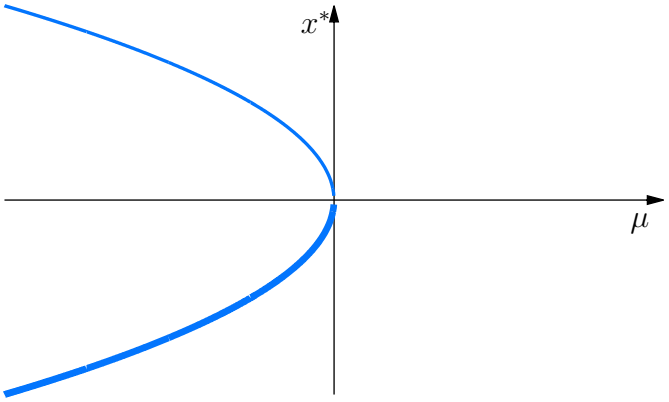

Figure 2.4: Bifurcation diagram of a saddle-node bifurcation found in eq. (2.15). For $\mu < 0$, two fixed points at $\pm\sqrt{|\mu|}$ exist. The thick line denotes the stable and the thin line the unstable fixed point, respectively.

For $\mu < 0$, two fixed points exist at $x^* = \pm\sqrt{|\mu|}$. To find their stability, the corresponding Jacobian is considered. In this case, it is simply the derivative with respect to time because eq. (2.15) is one dimensional

$$J = 2 \cdot x^*. \tag{2.16}$$

One finds that the fixed point at $x = -\sqrt{|\mu|}$ is stable while $x = \sqrt{|\mu|}$ is unstable. This can also be explained descriptively with the phase diagram (see fig. 2.3). Around the unstable fixed point, the velocities point away from the fixed point, meaning that a small perturbation would grow over time and thus the system changes its state. On the other hand, for the stable fixed point, the velocities point back towards the equilibrium such that a small perturbation would immediately be equalized by this reversing force. When μ is increased, the fixed points move towards each other and eventually for $\mu = 0$ they annihilate. For $\mu > 0$, no fixed points exist. The results are summarized in the bifurcation diagram in fig. 2.4.

2.4.2. Hopf Bifurcation

The *Hopf bifurcation* (or *Andronov-Hopf bifurcation*) is triggered by two complex conjugate eigenvalues crossing the imaginary axis. In this point, a fixed point changes its stability and at the same time a periodic solution emerges with a frequency close to the imaginary part of the eigenvalues which cross the imaginary axis. Two types of Hopf bifurcations are differentiated: *supercritical* and *subcrit-*

ical. First, consider a system which reaches its equilibrium through a damped oscillation and the damping rate depends on a parameter μ which can turn the decay into a growth for some critical value μ_c (see fig. 2.5). Then, at $\mu = \mu_c$ a supercritical Hopf bifurcation occurs. Formally, such a system can be written in polar coordinates as

$$\dot{r} = \mu r - r^3, \tag{2.17}$$

$$\dot{\varphi} = \omega + b\rho^2, \tag{2.18}$$

where the parameter μ controls the stability of the fixed point $r^* = 0$, ω defines the frequency of infinitesimal oscillations and b describes the dependence of the frequency on the amplitude. Rewriting the system in Cartesian coordinates simplifies to find the eigenvalues:

$$\dot{x} = \mu x - \omega y + \mathcal{O}(x^2, y^2) \tag{2.19}$$

$$\dot{y} = \omega x + \mu y + \mathcal{O}(x^2, y^2). \tag{2.20}$$

Finally, one sees that in the origin the Jacobian matrix

$$J = \begin{pmatrix} \mu & -\omega \\ \omega & \mu \end{pmatrix} \tag{2.21}$$

has the complex conjugated eigenvalues $\lambda_\pm = \mu \pm i\omega$ and thus the critical value for the system is $\mu = 0$.

An example for a system showing a subcritical Hopf bifurcation is given similarly but this time the cubic term r^3 is destabilizing:

$$\dot{r} = \mu r + r^3 - r^5, \tag{2.22}$$

$$\dot{\varphi} = \omega + br^2. \tag{2.23}$$

The fixed points are $r^* = 0$ and $r^* = \sqrt{\frac{1}{2} \pm \sqrt{\mu + \frac{1}{4}}}$. For $-\frac{1}{4} < \mu < 0$ two limit cycles exist, one is stable, the other one unstable (see fig. 2.6). For $\mu \nearrow 0$ the amplitude of the unstable limit cycle becomes smaller until it disappears for $\mu = 0$. Here, the fixed point in the center changes its stability. The corresponding

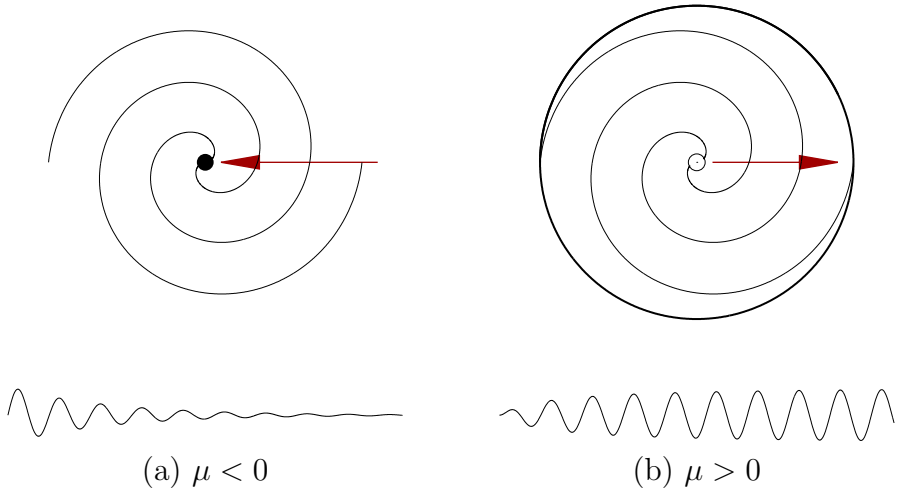

(a) $\mu < 0$ (b) $\mu > 0$

Figure 2.5: Phase diagram of a supercritical Hopf bifurcation (upper) for μ below and above the critical value $\mu_c = 0$ and (lower) schematic sketch of the time evolution of the oscillation dynamics. In (a) the oscillation is damped such that the system is attracted (indicated by the red arrow) to the stable equilibrium in the centre (filled circle). In (b) the amplitude of the oscillation increases which means that the origin in the phase diagram and the according spiral becomes unstable (empty circle) and drifts towards a limit cycle [Str94].

bifurcation diagram is displayed in fig. 2.8.

In both cases, sub- and supercritical, the amplitude of the emerging limit cycle scales as $\sqrt{\mu}$. To examine whether a Hopf bifurcation is sub- or supercritical can be decided by an analytical criterion [GH83], but it is easier to perform simulations and check the limit cycles which appear around the Hopf bifurcation [Str94].

2.5. Bifurcations of Cycles

So far, bifurcations of fixed points are analyzed. However, also periodic solutions can be involved in bifurcations as seen in section 2.4.2. In the following, several bifurcation types will be presented in which limit cycles interact with each other. These bifurcations are triggered by Floquet multipliers crossing the unit circle. The different possibilities are summarized in fig. 2.7.

2.5.1. Saddle-Node Bifurcation of Limit Cycles

A saddle-node bifurcation can not only occur when two fixed points collide but also when an unstable and a stable limit cycle annihilate in a bifurcation point.

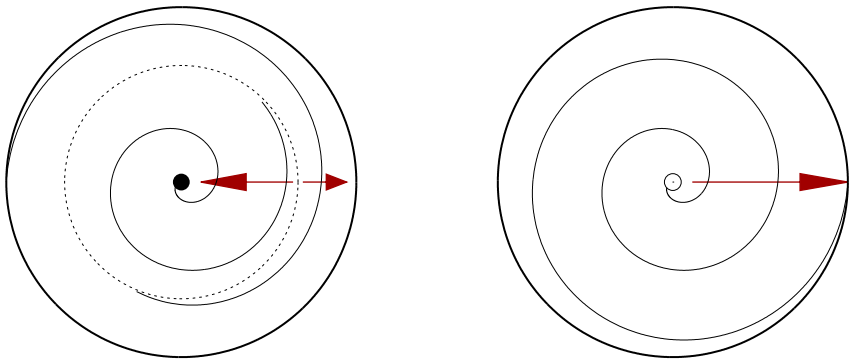

(a) $-\frac{1}{4} < \mu < 0$ (b) $\mu > 0$

Figure 2.6: Phase diagram of a subcritical Hopf bifurcation with μ below and above the critical value. In (a) one sees that there are two attractors, a stable limit cycle (thick line) and a stable fixed point in the origin (filled circle). In between, an unstable limit cycle is located (dashed line). The red arrows indicate the respective attracting force. For increasing μ, the unstable limit cycle tightens like a noose around the stable fixed point until eventually, for $\mu = 0$, the amplitude of the unstable cycle is zero, which leaves the origin unstable. At this point, the large-amplitude limit cycle is the only attractor [Str94].

In that case, a real Floquet multiplier crossing the unit cycle at $+1$ (see fig. 2.7a). An example for a system exhibiting such a bifurcation is given in eqs. (2.22) and (2.23) which is the same system that exhibits a subcritical Hopf bifurcation. For $\mu < -\frac{1}{4}$ no limit cycles exist, however, for $\mu = -\frac{1}{4}$ a stable and an unstable limit cycle emerge at $r = \sqrt{\frac{1}{2} \pm \sqrt{\mu + \frac{1}{4}}}$ as shown in fig. 2.6a. Note that the resulting limit cycles have an amplitude and period of $\mathcal{O}(1)$. The corresponding full bifurcation diagram is displayed in fig. 2.8.

2.5.2. Torus Bifurcation

A *torus bifurcation* can be described as a Hopf bifurcation of periodic solutions. Therefore, it is also referred to as secondary Hopf bifurcation. At the bifurcation point a pair of complex conjugate Floquet multipliers leave the unit circle (see fig. 2.7c). Thus, the limit cycle changes its stability and at the same time a solution with an additional periodicity emerges. The name torus is inspired by the fact that the system oscillates with two frequencies so that the phase space can be visualized on a torus. If the frequencies have a common multiple than the motion on the torus will be periodic. Otherwise the trajectory completely fills

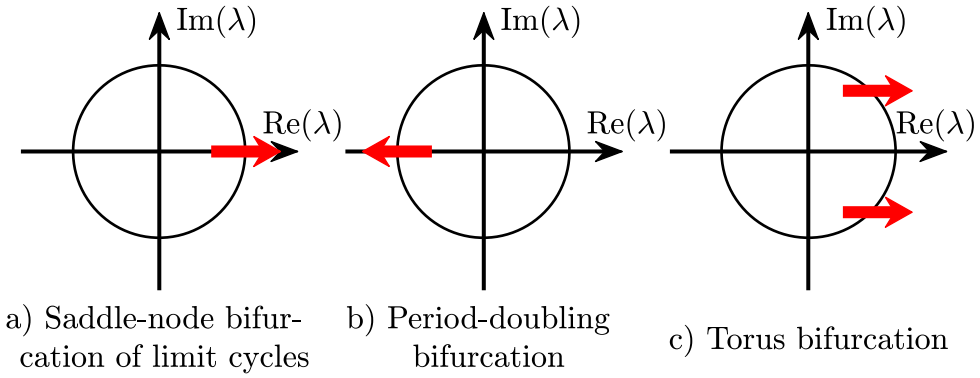

Figure 2.7: Possible bifurcation scenarios in which a periodic solution can loose its stability. As the Floquet multipliers are either real or pairs of complex conjugate values there are three possibilities. a) A saddle-node bifurcation of limit cycles occurs when a Floquet multiplier crosses the unit circle at $+1$. b) A Floquet multiplier crosses the unit circle at -1 which triggers a period-doubling bifurcation. c) A pair of complex conjugate Floquet multipliers leaving the unit circle results in a torus bifurcation.

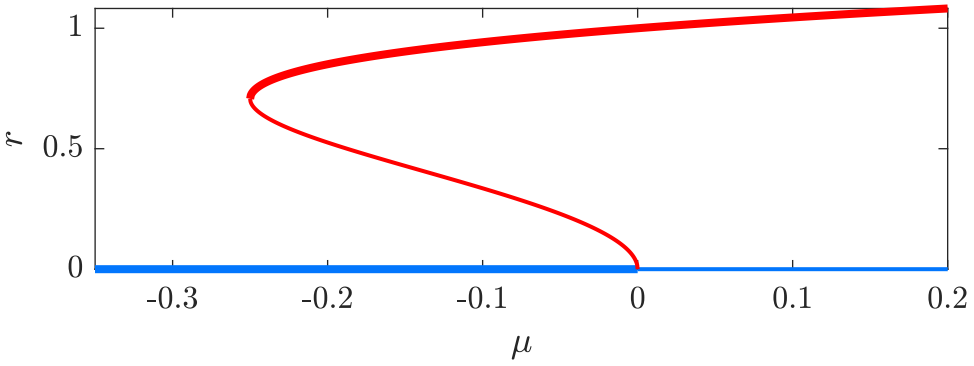

Figure 2.8: Full bifurcation diagram of eqs. (2.22) and (2.23). Thick lines stand for stable solution while thin lines correspond to unstable solutions. Blue lines are fixed points and red lines limit cycles. For $\mu = 0$ the fixed point $r^* = 0$ changes stability and an unstable limit cycle emerges in a subcritical Hopf bifurcation. This limit cycle collides with another periodic solution at $\mu = -\frac{1}{4}$ in a saddle-node bifurcation of limit cycles.

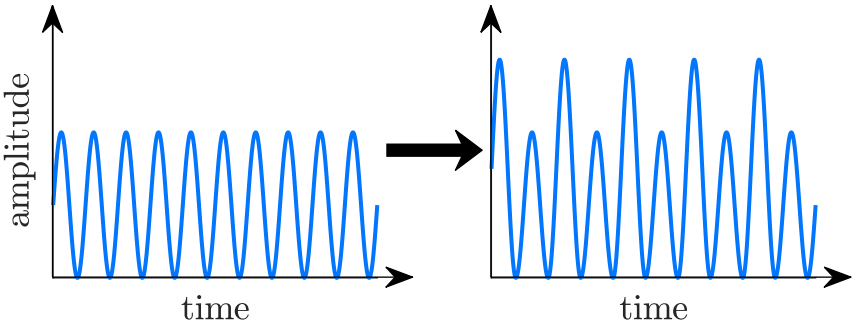

Figure 2.9: Illustration of a state before (left) and after (right) a period-doubling bifurcation occurs.

the surface of the torus. Like the Hopf bifurcation, a torus bifurcation can be sub- or supercritical.

2.5.3. Period-Doubling Bifurcation

In a *period-doubling bifurcation* (also called *flip bifurcation*) a real Floquet multiplier crosses the unit circle at -1 (see fig. 2.7b). This means that a small perturbation of magnitude ϵ results in a perturbation $-\epsilon$ after one period T. The sign of the perturbation changes with each period resulting in a state of period $2T$. A possible scenario is illustrated in fig. 2.9 where the amplitude in every second period is doubled after a period-doubling bifurcation occurred. At the same time the original limit cycle changes its stability. Like Hopf and torus bifurcations, period-doubling bifurcations can be sub- or supercritical depending on whether the emerging limit cycle is stable or not.

2.6. Global Bifurcations

In a local bifurcation the phase diagram is changed locally around a fixed point and thus they can be detected by local approximations such as linearization. In contrast, when a global bifurcation occurs the phase space is changed globally which is why local approximations cannot detect them.

An example for a global bifurcation is the *SNIPER bifurcation* (acronym for **S**addle-**N**ode **I**nfinite **Per**iod). Consider the following two dimensional system in polar coordinates

$$\dot{r} = r(1 - r^2), \tag{2.24}$$

$$\dot{\theta} = \mu - \sin\theta, \tag{2.25}$$

where $\mu > 0$. In the radial direction the obvious fixed points are $r^* = 0$ and $r^* = 1$. For $t \to \infty$ all trajectories (except $r^* = 0$) approach $r = 1$. For $\mu > 1$ the angular velocity can never reach zero so that a limit cycle with $r = 1$ forms. However, the angular velocity on the limit cycle has a slow part (around $\theta = \pi/2$) and a fast part (around $\theta = 3\pi/2$). Decreasing the parameter to $\mu \searrow 1$ slows down the angular velocity around $\theta = \pi/2$ further and further, until, for $\mu = 1$, two points of equilibrium form in a saddle-node bifurcation. Looking at the process in the other direction a limit cycle of amplitude $\mathcal{O}(1)$ emerges from a saddle-node bifurcation.

Topologically the so-called *homoclinic bifurcation* where a limit cycle collides with an unstable fixed point resembles the SNIPER bifurcation. Thus, it is difficult to distinguish the two. The key lies in the scaling behavior of the period of the limit cycles. The limit cycle emerging from a SNIPER bifurcation scales as $(\mu - \mu_c)^{-\frac{1}{2}}$ while the homoclinic bifurcation scales as $-\log(\mu - \mu_c)$ where μ_c is the parameter at which the bifurcation occurs [Str94]. The scaling behavior of the SNIPER bifurcation also contribute to its name as the period approaches ∞ for $\mu \to \mu_c$.

Note that a limit cycle can also be born in a saddle-node bifurcation of limit cycles. In that case the newly born periodic solution exhibits a secondary period similar to the scenario in a torus bifurcation.

2.7. Numerical Approximations with Delay Interpolation

In most cases it is not possible to express a solution of a nonlinear dynamical system in closed analytical form. However, there are numerical methods to approximate the solution. For initial value problems of DDEs the systems has to be initialized by function defined on an interval which has the length of the longest delay: $x_0(\theta),\ \theta \in [-\max(\tau_1, ..., \tau_N), 0)$. For a one-dimensional system the dynamics are governed by

$$\dot{x} = f(x(t), x(t - \tau_1), ..., x(t - \tau_N), t), \tag{2.26}$$

where N is the number of delays. However, the following approaches can easily be extended to systems with higher dimensions. The simplest numerical approach is the explicit *Euler method*. It uses the fact that the derivative of any point is known as it is governed by eq. (2.26). Thus, during a small increment in time Δt, the distance $f(x_0, x_{-M_1}, ..., x_{-M_N}, t_0) \cdot \Delta t, M_i = \lfloor \frac{\tau_i}{h} \rfloor$ is covered assuming that the flux does not change during Δt. Eventually, this is only an approximation but for a sufficiently small increment the error which is being made becomes negligible. Hence, the position $x(t_0+\Delta t)$ is approximately $x_0+f(x_n, x_{n-M_1}, ..., x_{n-M_N}, t_0)\cdot\Delta t$. This step can be applied iteratively so that

$$x_{n+1} = x(t_{n+1}) = x_n + f(x_n, x_{n-M_1}, ..., x_{n-M_n}, t_n) \cdot \Delta t, \tag{2.27}$$

where $t_n = t_0 + n\Delta t$. Basically, the Euler method describes a Taylor expansion of first order in each point, meaning that the error made in each step, referred to as the *local truncation error*, is $\mathcal{O}(\Delta t^2)$. It can be shown that the *global truncation error* (the error between the exact solution $x(t_n)$ and the approximate solution x_n) is $\mathcal{O}(\Delta t)$ [Str94]. Therefore, the Euler method is first order of accuracy. Naively, one could say that in order to increase the accuracy of the numerical method one should just decrease Δt. However, this makes the computation very intense which one wants to avoid.

Thus, methods of higher orders are needed. This can be achieved, e.g., by appropriately combining the derivatives at several different points over the time step interval. This approach is realized by the *family of Runge-Kutta methods*. In particular, for the *forth order Runge-Kutta method* with the usual Butcher tableau applied to eq. (2.26), the next step from a given solution x_n is

$$x_{n+1} = x_n + \frac{1}{6}(k_1 + 2k_2 + 2k_3 + k_4)\Delta t \tag{2.28}$$

with

$$k_1 = f(x_n, x_{n-M_1}, ..., x_{n-M_N}, t_n), \tag{2.29}$$

$$k_2 = f(x_n + \frac{1}{2}k_1\Delta t, x_{n-M_1+\frac{1}{2}}, ..., x_{n-M_N+\frac{1}{2}}, t_n + \frac{1}{2}\Delta t), \tag{2.30}$$

$$k_3 = f(x_n + \frac{1}{2}k_2\Delta t, x_{n-M_1+\frac{1}{2}}, ..., x_{n-M_N+\frac{1}{2}}, t_n + \frac{1}{2}\Delta t), \tag{2.31}$$

$$k_4 = f(x_n + k_3\Delta t, x_{n-M_1+1}, ..., x_{n-M_N+1}, t_n + \Delta t). \tag{2.32}$$

The scheme is visualized in (see fig. 2.10). The local truncation error is $\mathcal{O}(\Delta t^5)$ while the global truncation error is $\mathcal{O}(\Delta t^4)$ [Gur18]. This means that when, e.g., a step size of $h/2$ is used, the global truncation error is $(1/2)^4 = 1/16$ of the error made for a step size h.

Note that the introduction of delay poses a problem. In eqs. (2.30) and (2.31) the states of the system at half steps $x_{n-M_i+\frac{1}{2}}$ are needed in order to retain forth-order accuracy. To address this issues, fourth-order Hermite interpolation is used, i.e., a third order polynomial

$$x(t) = a_0 + a_1 t + a_2 t^2 + a_3 t^3 \tag{2.33}$$

$$x'(t) = a_1 + 2a_2 t + 3a_3 t^2 \tag{2.34}$$

that crosses the known points at x_{n-M_i} and x_{n-M_i+1} with the corresponding known derivatives x'_{n-M_i} and x'_{n-M_i+1} needs to be found. Choosing the origin such that $x_{n-M_i+\frac{1}{2}}$ is at $t = 0$ simplifies the problem as only the constant coefficient needs to be found:

$$x_{n-M_i+\frac{1}{2}} = a_0 + a_1 0 + a_2 0 + a_3 0 = a_0. \tag{2.35}$$

Then, the known points x_{n-M_i} and x_{n-M_i+1} are located at $t = \pm\frac{\Delta t}{2}$ which results in the following conditions:

$$x_{n-M_i} = a_0 - a_1\frac{\Delta t}{2} + a_2\frac{\Delta t^2}{4} - a_3\frac{\Delta t^3}{8}, \tag{2.36}$$

$$x_{n-M_i+1} = a_0 + a_1\frac{\Delta t}{2} + a_2\frac{\Delta t^2}{4} + a_3\frac{\Delta t^3}{8}, \tag{2.37}$$

$$x'_{n-M_i} = a_1 - 2a_2\frac{\Delta t}{2} + 3a_3\frac{\Delta t^2}{4}, \tag{2.38}$$

$$x'_{n-M_i+1} = a_1 + 2a_2\frac{\Delta t}{2} + 3a_3\frac{\Delta t^2}{4}. \tag{2.39}$$

Adding eqs. (2.36) and (2.37) and subtracting eqs. (2.38) and (2.39) yields

$$2a_0 + 2a_2\frac{\Delta t^2}{4} = x_{n-M_i+1} + x_{n-M_i}, \tag{2.40}$$

$$4a_2\frac{\Delta t}{2} = x'_{n-M_i+1} - x'_{n-M_i}. \tag{2.41}$$

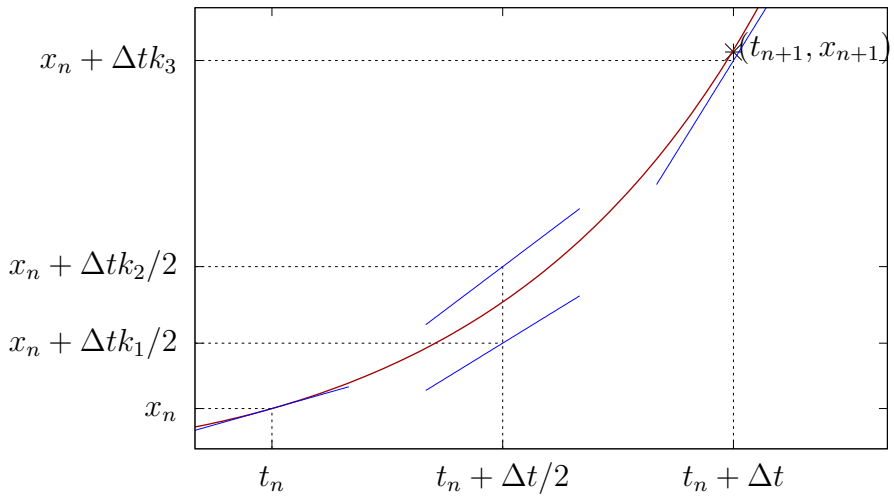

Figure 2.10: Visualization of the fourth-order Runge-Kutta method. The red line describes the course of $x(t)$, the blue lines are the slopes k_i given by eqs. (2.29) to (2.32). The star denotes the next step x_{n+1} after combining the information of all k_i.

Combining eqs. (2.35), (2.40) and (2.41) finally gives

$$x_{n-M_i+\frac{1}{2}} = \frac{x_{n-M_i} + x_{n-M_i+1}}{2} + \frac{\Delta t}{8}\left(x'_{n-M_i} - x'_{n-M_i+1}\right). \tag{2.42}$$

This method requires that for the length of each delay not only the state of the system needs to be saved but also its derivative which is available straight from the Runge-Kutta method in eq. (2.32). Further, note that the procedure has to be repeated for all delays τ_i.

One could conclude that using Runge-Kutta methods of higher orders improves the accuracy for a given step size. However, to achieve a higher order eq. (2.26) has to be evaluated at more substeps called *stages*, e.g., the forth-order Runge-Kutta method has four stages (see eqs. (2.29) to (2.32)). Thus, increasing the order only makes sense up to some limit given by the so-called *Butcher barrier*. It states that the amount of stages m grows faster than the order p. In other words, for $m \geq 5$, there are no Runge-Kutta methods with the convergence order $p = m$ [Gur18]. Indeed, to reach order five, $m = 6$ is required. Therefore, the forth-order Runge-Kutta method is generally regarded as the best trade-off between a fast computation speed and a low error [Str94].

2.8. Numerical Path Continuation

Numerical path continuation is a very useful tool in the analysis of dynamical systems because it allows one to examine the behavior of the solutions in the parameter space and hence, to follow the stable and unstable solution branches. Furthermore, bifurcations can be detected which offers the possibility to find new solution branches. Finally, bifurcation points can be tracked in higher dimensional parameter spaces which allows to perform two-parameter-continuation. Depending on what kind of dynamical system is analyzed, different software packages are available. Since the dynamical system in this thesis is described by DDEs, the `MATLAB` package `DDE-BIFTOOL` [ELR02; Sie+14] is used. In the following, the necessary steps to follow a branch in the parameter space are presented.

Let $\dot{\boldsymbol{x}} = \boldsymbol{f}(\boldsymbol{x}, \mu)$ be a system of n differential equations with one control parameter μ and $\boldsymbol{x}_0^* = (x_{0,1}^*, x_{0,2}^*, ..., x_{0,n}^*)$ is a solution for $\mu = \mu_0$. The solution $\boldsymbol{x}_0^*$ is called an *initial guess* and can be obtained, e.g., from direct numerical simulations. Now, one wants to compute the solution $\boldsymbol{x}_1^*$ for the parameter $\mu_1 = \mu_0 + \Delta\mu$. Therefore, the tangent of the curve $\boldsymbol{x}^*(\mu)$ at $(\boldsymbol{x}_0^*, \mu_0)$ is used in order to make a first prediction $\boldsymbol{x}_1^{*(0)}$ at μ_1 [Thi17]:

$$\boldsymbol{x}_1^{*(0)} = \boldsymbol{x}_0^* + \Delta\mu \left.\frac{\partial \boldsymbol{x}^*}{\partial \mu}\right|_{(\boldsymbol{x}_0^*, \mu_0)}. \tag{2.43}$$

The slope can easily be computed when differentiating $\boldsymbol{f}(\boldsymbol{x}^*(\mu), \mu) = 0$:

$$\begin{aligned} &\left[\underbrace{\frac{\partial \boldsymbol{f}}{\partial \boldsymbol{x}}}_{\text{Jacobian}} \frac{\partial \boldsymbol{x}}{\partial \mu} + \frac{\partial \boldsymbol{f}}{\partial \mu}\right]_{(\boldsymbol{x}_0^*, \mu_0)} = 0 \\ \Leftrightarrow \quad &\left.\frac{\partial \boldsymbol{x}}{\partial \mu}\right|_{(\boldsymbol{x}_0^*, \mu_0)} = -\left[\left(\frac{\partial \boldsymbol{f}}{\partial \boldsymbol{x}}\right)^{-1} \cdot \frac{\partial \boldsymbol{f}}{\partial \mu}\right]\Bigg|_{(\boldsymbol{x}_0^*, \mu_0)}. \end{aligned} \tag{2.44}$$

The approximation $\boldsymbol{x}_1^{*(0)}$ of the solution $\boldsymbol{x}_1^*$ is supposed to satisfy $\boldsymbol{f}(\boldsymbol{x}_1^{*(0)}, \mu_1) = 0$ but since a linear approximation is used, the error is expected to be significant. Thus, the next step is to "improve" the guess for $\boldsymbol{x}_1^*$. This can be achieved with *Newton's method* which can compute roots of functions up to an arbitrary order. The iteration is given by

$$\boldsymbol{x}_1^{*(n+1)} = \boldsymbol{x}_1^{*(n)} - \left(\frac{\partial \boldsymbol{f}}{\partial \boldsymbol{x}}\right)^{-1}\Bigg|_{(\boldsymbol{x}_1^{*(n)},\mu_0)} \cdot \boldsymbol{f}\left(\boldsymbol{x}_1^{*(n)}\right). \tag{2.45}$$

Then one can return to change μ, find the root for the new parameter and continue to follow the solution branch.

This method is unproblematic until the branch approaches a fold at some $\mu = \mu_\mathrm{f}$, which is a bifurcation type that occurs frequently. The problem is that for $\mu < \mu_\mathrm{f}$, two solutions exist while there is none for $\mu > \mu_\mathrm{f}$ [Thi17]. To follow the branch around the fold, a parameter which is unique along the branch is needed. The issue is addressed with the *pseudo-arclength continuation* of which only the general idea is presented at this point. The control parameter μ is interpreted as an additional element of the extended solution $\boldsymbol{y^*} = (\boldsymbol{x}^*, \mu)$. Instead of μ, the new control parameter is the arclength s, which can be approximated locally with Pythagoras' theorem:

$$|\boldsymbol{x}^*|^2 + (\Delta\mu)^2 = (\Delta s)^2. \tag{2.46}$$

This condition $\boldsymbol{p}(\boldsymbol{x}^*, \mu, s)$ supplements $\boldsymbol{f}(\boldsymbol{x}^*, \mu)$ so that the extended system can be introduced

$$\boldsymbol{E}(\boldsymbol{y^*}, s) = \begin{pmatrix} \boldsymbol{f}(\boldsymbol{x}^*, \mu) \\ \boldsymbol{p}(\boldsymbol{x}^*, \mu, s) \end{pmatrix}. \tag{2.47}$$

The next steps are equivalent to the described method above. In order to compute the solution at $s_{j+1} = s_j + \Delta s$, a tangent of the curve $\boldsymbol{y^*}(s)$ at $(\boldsymbol{y}_j^*, s_j)$ is used as a predictor for $\boldsymbol{y}_{j+1}^{*(0)}$. To find the root $\boldsymbol{y}_{j+1}^*$ up to the desired exactness, Newton's method is applied [Thi17].

3. Mode-Locked Laser Model with Delayed Feedback

In this chapter a set of DDEs describing passive mode-locking in a ring laser, are deduced following the derivation in [VT05]. Further, these equations are extended by an additional term describing time delayed feedback. Finally, the lasing threshold for this model is analytically calculated.

3.1. Mathematical Description

Previous attempts to describe laser systems with passive mode-locking were conducted via PDEs by New [New74] and Haus [Hau75]. However, they relied on the strong assumptions of small gain and loss per cavity round trip which questions their ability to properly describe real laser systems. In contrast, [VT05] derives a set of DDEs to describe a system which does not rely on such approximations and only adopt the assumption of ring-cavity geometry and unidirectional lasing.

At first, the additional feedback loop is neglected. The basic idea is to split the main cavity in fig. 1.1 into five sections: the gain element ($z_3 < z < z_4$), the absorber element ($z_2 < z < z_3$), the bandwidth limiting element ($z_5 < z < z_1 + L$ where L is the length of the cavity) and the parts between the bandwidth limiting element and gain ($z_4 < z < z_5$) and absorber elements ($z_1 < z < z_2$), respectively. The last two mentioned sections are passive. In each of these sections, the dynamics are governed by different equations which need to be combined to describe the dynamic of the system for a full round-trip. First, in the gain and absorber sections, one considers the so-called traveling wave equations which describe a slowly changing electrical field $E(t, z)$ [TLO94]

$$\frac{\partial E(t,z)}{\partial z} + \frac{1}{v}\frac{\partial E(t,z)}{\partial t} = \frac{g_r \Gamma_r}{2}(1 - i\alpha_r)[N_r(t,z) - N_r^{tr}]E(t,z), \tag{3.1}$$

$$\frac{\partial N_r(t,z)}{\partial t} = J_r - \gamma_r N_r(t,z) - v g_r \Gamma_r [N_r(t,z) - N_r^{tr}]|E(t,z)|^2, \tag{3.2}$$

where the subscript r stands for the gain ($r = g$) and absorber ($r = a$) sections, $N_{g,a}$ are the carrier densities in the respective sections, $N_{g,a}^{tr}$ are the carrier densities evaluated at the transparency threshold, v is the (constant) light group velocity and J_g is the injection current in the gain section (for the absorber $J_a = 0$).

The parameters $\alpha_{g,a}$, $g_{g,a}$, $\Gamma_{g,a}$ and $\gamma_{g,a}$ are, respectively, linewidth enhancement factors, differential gains, transverse nodal fill factors and carrier density relaxation rates in the gain and absorber section. The evolution of the electric field in the passive sections is governed by

$$\frac{\partial E(t,z)}{\partial z} + \frac{1}{v}\frac{\partial E(t,z)}{\partial t} = 0 \tag{3.3}$$

and the dynamics in the bandwidth limiting element can be described in Fourier space

$$\hat{E}(\omega, z_1 + L) = \hat{f}(\omega)\hat{E}(\omega, z_5). \tag{3.4}$$

Here, $\hat{f}(\omega)$ describes the line shape in the bandwidth limiting element.

Equations (3.1),(3.2) and (3.3) can be simplified by a nondimensionalization $(t,z) \to (\tau,\zeta)$ where $\tau = \gamma_a(t - z/v)$ is the retarded time divided by the absorber relaxation time and $\zeta = z\gamma_a/v$ is the normalized coordinate along the cavity axis. With these transformations, eqs. (3.1) and (3.2) become

$$\frac{\partial A(\tau,z)}{\partial \zeta} = \frac{1}{2}(1 - i\alpha_{g,a})n_{g,a}(\tau,z)A(\tau,z), \tag{3.5}$$

$$\frac{\partial n_g(\tau,z)}{\partial \tau} = j_g - \Gamma n_g(\tau,z) - n_g(\tau,z)|A(\tau,z)|^2, \tag{3.6}$$

$$\frac{\partial n_a(\tau,z)}{\partial \tau} = j_a - n_a(\tau,z) - s n_a(\tau,z)|A(\tau,z)|^2. \tag{3.7}$$

Here, $A(\tau,\zeta) = E(t,z)\sqrt{v g_g \Gamma_a/\gamma_a}$, $n_{g,a}(\tau,\zeta) = v g_{g,a}\Gamma_{g,a}[N_{g,a}(t,z) - N^{tr}_{g,a}]/\gamma_a$, $j_g = v g_g \Gamma_g (J_g - \gamma_g N^{tr}_g)/\gamma_a^2$, $j_a = v g_g \Gamma_g N^{tr}_a/\gamma_a$ and $\Gamma = \gamma_g/\gamma_a$. The parameter $s = (g_a\Gamma_a)/(g_g\Gamma_g)$ is the ratio of the saturation intensities in the gain and absorber sections. The passive section described in eq. (3.3) transforms as

$$\frac{\partial A(\tau,\zeta)}{\partial \zeta} = 0. \tag{3.8}$$

Solving eqs. (3.4) to (3.8) yields the transformation of the electric field amplitude in each section. According to eq. (3.8), the relations in the passive sections between input and output are

$$A(\tau, \zeta_2) = A(\tau, \zeta_1), \tag{3.9}$$
$$A(\tau, \zeta_5) = A(\tau, \zeta_4), \tag{3.10}$$

where $\zeta_k = \frac{z_k \gamma_a}{v}, k = 1, ..., 5$. Next, the transformation in the gain and absorber sections is analyzed by integrating eq. (3.5) over ζ_2 to ζ_3 and ζ_3 to ζ_4. This yields

$$A(\tau, \zeta_4) = \exp\left(\frac{1 - i\alpha_g}{2} G(\tau)\right) A(\tau, \zeta_3), \tag{3.11}$$
$$A(\tau, \zeta_3) = \exp\left(\frac{1 - i\alpha_a}{2} Q(\tau)\right) A(\tau, \zeta_2), \tag{3.12}$$
$$\text{where } G(\tau) = \int_{\zeta_3}^{\zeta_4} n_g(\tau, \zeta) d\zeta \tag{3.13}$$
$$\text{and } Q(\tau) = -\int_{\zeta_2}^{\zeta_3} n_a(\tau, \zeta) d\zeta. \tag{3.14}$$

Here, the dimensionless quantities $G(\tau)$ and $Q(\tau)$ describe the gain and loss introduced by the absorber and gain sections [AO89]. Their dynamics can be described by integrating eqs. (3.6) and (3.7) over ζ_2 to ζ_3 and ζ_3 to ζ_4. Also, from eq. (3.5) the relation

$$\int_{\zeta_{2,3}}^{\zeta_{3,4}} n_{g,a}(\tau, \zeta) |A(\tau, \zeta)|^2 d\zeta = -|A(\tau, \zeta_{3,4})|^2 + |A(\tau, \zeta_{2,3})|^2 \tag{3.15}$$

can be obtained. Combining all of this yields

$$\partial_\tau G(\tau) = g_0 - \Gamma G(\tau) - |A(\tau, \zeta_4)|^2 + |A(\tau, \zeta_3)|^2, \tag{3.16}$$
$$\partial_\tau Q(\tau) = q_0 - G(\tau) + s|A(\tau, \zeta_3)|^2 - s|A(\tau, \zeta_2)|^2, \tag{3.17}$$
$$\text{where } g_0 = \int_{\zeta_3}^{\zeta_4} j_g d\zeta \tag{3.18}$$
$$\text{and } q_0 = \int_{\zeta_2}^{\zeta_3} j_a d\zeta. \tag{3.19}$$

In the time domain, the dynamics in the bandwidth limiting element described by eq. (3.4) can be rewritten as

$$A(\tau, \zeta_1 + T) = \int_{-\infty}^{\tau} f(\tau - \theta) A(\theta, \zeta_5) d\theta, \tag{3.20}$$

where $T = \frac{\gamma_a L}{v}$ is the normalized round-trip time. Defining $A(\tau) \coloneqq A(\tau, \zeta_1)$ and combining everything by inserting eqs. (3.9) to (3.12) in eq. (3.20) and using periodic boundaries, i.e., $A(\tau, \zeta + T) = A(\tau + T, \zeta)$, yields

$$A(\tau + T) = \int_{-\infty}^{\tau} f(\tau - \theta) R(\theta) A(\theta) d\theta, \tag{3.21}$$

$$\text{where } R(\theta) = \sqrt{\kappa} \exp\left[\frac{1 - i\alpha_g}{2} G(\theta) - \frac{1 - i\alpha_a}{2} Q(\theta)\right]. \tag{3.22}$$

Here, κ is the fraction of the intensity remaining in the cavity after each round-trip. Finally, only a specific form of the bandwidth limiting element needs to be chosen. A Lorentzian shape $f(\tau) = \gamma \exp[(-\gamma + i\Omega)\tau]$ is used in this case. After changing the coordinates $A \to A \exp(i\Omega\tau)$ and renaming $\tau \to t$ and $T \to \tau_1$, this reads

$$\frac{\dot{A}}{\gamma} = R(t - \tau_1) A(t - \tau_1) - A(t), \tag{3.23}$$

$$\text{where } R(\theta) = \sqrt{\kappa} \exp\left[\frac{1 - i\alpha_g}{2} G(\theta) - \frac{1 - i\alpha_a}{2} Q(\theta) - i\varphi\right] \tag{3.24}$$

$$\text{and } \varphi = \Omega\tau_1. \tag{3.25}$$

Finally, the additional time delayed feedback needs to be considered. According to fig. 1.1, it is the state of the electric field at $t - \tau_2$ of strength η and with a relative phase of Ω. Thus, the final equations of motion read

$$\frac{\dot{A}}{\gamma} = R(t - \tau_1) A(t - \tau_1) - A(t) + \eta e^{i\Omega} A(t - \tau_2), \tag{3.26}$$

$$\dot{G} = g_0 - \Gamma \cdot G - e^{-Q}\left(e^{G} - 1\right)|A|^2, \tag{3.27}$$

$$\dot{Q} = q_0 - Q - s\left(1 - e^{-Q}\right)|A|^2, \tag{3.28}$$

where $R(\theta)$ is defined in eq. (3.24) and eqs. (3.27) and (3.28) are obtained from eqs. (3.16) and (3.17) by using eqs. (3.9) to (3.12).

3.2. Lasing Threshold

This derivation follows section 3.2.1 in [Jau16]. Below a certain threshold value for the pump rate, a semiconductor laser remains in the *off state* as the losses cannot be compensated. The off state is the trivial steady state solution (i.e., $A = 0, \dot{G} = \dot{Q} = 0$) of eqs. (3.26) to (3.28) which reads

$$A = 0, \tag{3.29}$$
$$G = \frac{g_0}{\Gamma}, \tag{3.30}$$
$$Q = q_0. \tag{3.31}$$

At the threshold pump rate, this solution becomes unstable in a Hopf bifurcation from where the so-called *continuous wave (CW)* solutions emerge. These solutions have the form $A(t) = A_0 \cdot e^{i\omega t}$. Substituting this into eq. (3.26) leads to

$$\frac{i\omega}{\gamma} = \sqrt{\kappa} \exp\left[\frac{1 - i\alpha_g}{2} G - \frac{1 - i\alpha_a}{2} Q - i\varphi\right] e^{-i\omega\tau_1} - 1 + \eta e^{i\Omega} e^{-i\omega\tau_2}, \tag{3.32}$$

where G and Q are the steady state solutions of eqs. (3.27) and (3.28) and thus fulfill

$$\dot{G} = 0 = g_0 - \Gamma \cdot G - e^{-Q}\left(e^G - 1\right)|A_0|^2 \tag{3.33}$$
$$\text{and } \dot{Q} = 0 = q_0 - Q - s\left(1 - e^{-Q}\right)|A_0|^2. \tag{3.34}$$

Separating eq. (3.32) into its real and imaginary parts yields

$$1 = \sqrt{\kappa} \exp\left[\frac{1}{2}(G - Q)\right] \cdot \cos\left(\frac{1}{2}(\alpha_g G - \alpha_a Q) + \varphi + \omega\tau_1\right) + \eta \cos(\Omega - \omega\tau_2), \tag{3.35}$$

$$\frac{\omega}{\gamma} = -\sqrt{\kappa} \exp\left[\frac{1}{2}(G - Q)\right] \cdot \sin\left(\frac{1}{2}(\alpha_g G - \alpha_a Q) + \varphi + \omega\tau_1\right) + \eta \sin(\Omega - \omega\tau_2). \tag{3.36}$$

Squaring and summing eqs. (3.35) and (3.36) then gives

$$1+\frac{\omega^2}{\gamma^2}+\eta^2-2\eta\left(\frac{\omega}{\gamma}\sin\left(\Omega-\omega\tau_2\right)+\cos\left(\Omega-\omega\tau_2\right)\right)=\kappa e^{G-Q}. \tag{3.37}$$

One can also regard eq. (3.36) divided by eq. (3.35):

$$\begin{aligned}\frac{\omega}{\gamma}=&\frac{-\tan\left(\frac{1}{2}(\alpha_g G-\alpha_a Q)+\varphi+\omega\tau_1\right)}{1+\frac{\eta\cos(\Omega-\omega\tau_2)}{\sqrt{\kappa}\exp\left[\frac{1}{2}(G-Q)\right]\cos\left(\frac{1}{2}(\alpha_g G-\alpha_a Q)+\varphi+\omega\tau_1\right)}}\\&+\frac{\tan(\Omega-\omega\tau_2)}{1+\frac{\sqrt{\kappa}\exp\left[\frac{1}{2}(G-Q)\right]\cos\left(\frac{1}{2}(\alpha_g G-\alpha_a Q)+\varphi+\omega\tau_1\right)}{\eta\cos(\Omega-\omega\tau_2)}}.\end{aligned} \tag{3.38}$$

Equations (3.33), (3.34), (3.37) and (3.38) are a set of four transcendental equations for the four variables A_0, G, Q and ω. There are various solutions for different values of the frequency ω and the intensity $|A|^2$, each corresponding to different lasing modes. Each mode should fulfill eqs. (3.33), (3.34), (3.37) and (3.38) at its lasing threshold for $A_0 = 0$ as the CW solutions bifurcate from the off state. Rearranging eq. (3.33) and using eqs. (3.34) and (3.37) yields the mode-dependent threshold pumping rate:

$$\begin{aligned}g_{0,\mathrm{th}}=&\Gamma\left\{q_0-\ln(\kappa)+\ln\left[1+\frac{\omega^2}{\gamma^2}+\eta^2\right.\right.\\&\left.\left.-2\eta\left(\frac{\omega}{\gamma}\sin\left(\Omega-\omega\tau_2\right)+\cos\left(\Omega-\omega\tau_2\right)\right)\right]\right\},\end{aligned} \tag{3.39}$$

where ω still fulfills eq. (3.38). In the following bifurcation analysis, $\varphi = \Omega = 0$ is chosen. Then the threshold reaches a minimum for $\omega = 0$. Here, a stable branch of CW solutions emerges from which eventually the mode-locked solutions in form of pulses bifurcate. All modes corresponding to higher values of ω bifurcate from the off state when it is already unstable, and are unstable as well. Thus, the threshold value is defined as

$$g_{0,\mathrm{th}}=\Gamma\left[q_0-\ln(\kappa)+2\cdot\ln(1-\eta)\right]. \tag{3.40}$$

In the following, if not stated differently, a normalized gain value $g = g_0/g_{0,\mathrm{th}}$ is used.

4. Mode-Locked Laser Dynamics

In this chapter the dynamics of a PML semiconductor laser with time delayed feedback is analyzed using the model presented in chapter 3. The dynamics are studied via direct numerical simulations and performing numerical path continuation in order to find bifurcation points of the DDE model given in eqs. (3.26) to (3.28). The numerical path continuation is carried out using the software package `DDE-BIFTOOL`. This package also allows to determine the eigenvalues and Floquet multipliers and thereby find the stability of solutions.

4.1. From Direct Numerical Simulations to Numerical Path Continuation

The first step in the analysis is to conduct DNSs using the methods presented in section 2.7. When operating below the lasing threshold, the off-state ($A = 0, G = g_0/\Gamma, Q = q_0$) is a stable fixed point as shown in section 3.2. For proper parameters, additional periodic solutions in form of pulses are found. Both solutions can exist for the same parameter set which means that the system is *bistable*. The system needs to be kicked in order for a pulse to arise from the off state. For this use case it is sufficient to initialize the system with a narrow square pulse and after a few round-trips the system settles on a stable attractor. Depending on the initial condition and the applied parameter set the solution can consist of different numbers of pulses in the cavity. Solutions with a single pulse per round-trip are the *fundamental mode-locked* (FML) solutions, while states with multiple equidistant pulses per round-trip are called *harmonic mode-locked* (HML) solutions. In the following HML solutions with n pulses are referred to as HML_n. Figures 2.1 and 2.2 show the results of a DNS of a FML solution for the parameter set $(\gamma, \kappa, \Gamma, q_0, \alpha_g, \alpha_a, \eta, \tau_1, \tau_2, s, g, \varphi, \Omega) = (10, 0.8, 0.04, 0.3, 1.5, 0.5, 0.006, 100, 80, 10, 0.95, 0, 0)$. Throughout this thesis the parameters $\gamma, \kappa, \Gamma, q_0, s, \varphi$ and Ω will be kept at these values if not stated differently. The influence of time delayed feedback can be seen in both figures in form of a train of satellite pulses behind the main pulse.

In order to analyze these solutions in parameter space one needs to feed them into a continuation program which is `DDE-BIFTOOL` in this case. As the solution is periodic the profile of a whole period needs to be extracted. In addition, the period T needs to be found which can be realized by computing the autocorrela-

tion of the whole time trace. This information is given DDE-BIFTOOL as an initial guess which is refined until the desired accuracy is reached. In this process the mesh, on which the profile is given, is adapted. Initially, it is given on a mesh with constant spacing as the result is obtained from a DNS with constant step size. In order to improve computational speed it makes sense to refine the mesh where the solution changes quickly, i.e., where pulses are located, and widen the spacing where the solution remains approximately constant. This is realized by defining a grid of n interval points. Between the interval points the solution is a polynomial of degree d. Thus, in total the solution is stored in a mesh of $d \cdot n + 1$ points. Throughout this thesis $n = 100$ and $d = 5$ are chosen.

4.2. Emergence of Localized Structures

Figures 2.1 and 2.2 are obtained in the localized regime below the lasing threshold. This section shall highlight how these periodic solutions are born and how the solutions become localized. Note that in this section time delayed feedback is neglected for simplification, however, the mechanism is analogue when feedback is added. In section 3.2 it is shown that at $g = 1$ the off-state becomes unstable. In this bifurcation the CW solution emerges. When increasing the gain further, the CW branch undergoes several Hopf bifurcations in each of which a periodic solution is born. The periodic solutions correspond to states with different numbers of equidistant pulses per round-trip. The FML, HML_2 and HML_3 branches are displayed in fig. 4.1a where the Hopf bifurcations are marked by orange dots.

The dynamics of the bifurcation points on the CW branch is controlled by the feedback length τ_1. Figure 4.2 shows the branch of the FML solution for different cavity lengths τ_1. Panel a) shows that for $\tau_1 = 30$ the FML solution emerges in a subcritical Hopf bifurcation while in panel b) for $\tau_1 = 40$ the Hopf bifurcation is supercritical. Increasing the cavity's length leads to a detachment of the branch from the CW branch (fig. 4.2c) as the Hopf bifurcation on the CW branch collides with another Hopf bifurcation from where an unstable FML solution emerges. When τ_1 is increased further the whole branch shifts towards smaller gain values and eventually, FML solutions exist below the lasing threshold (fig. 4.2d). In this case the solutions are localized.

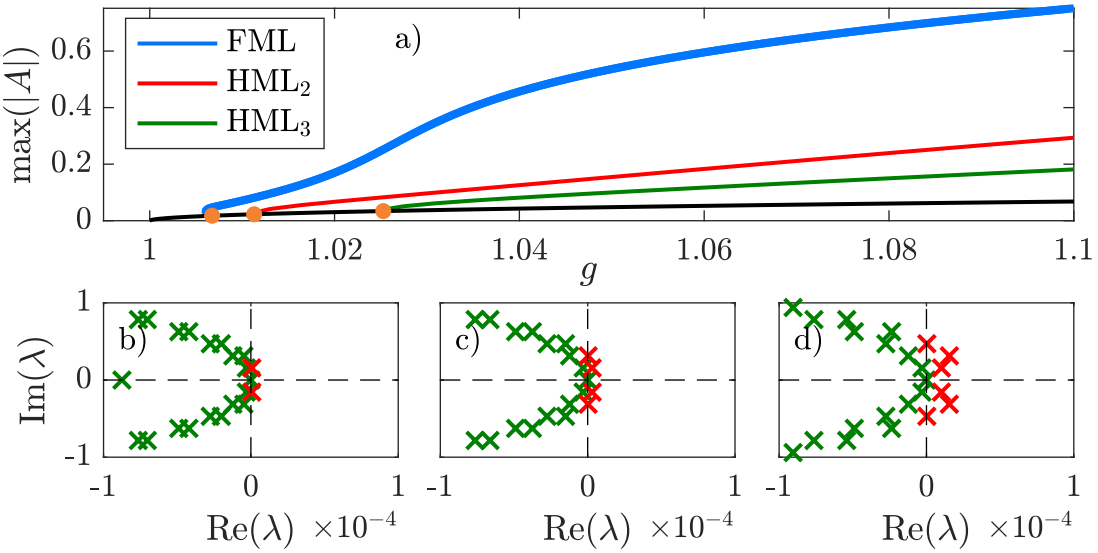

Figure 4.1: Bifurcation diagram of eqs. (3.26) to (3.28). Panel a) shows the emergence of mode-locked pulses from the CW solution (black line). Branches for solutions with (blue) one, (red) two and (green) three pulses per round-trip are displayed. Each solution is born in a Hopf bifurcation (orange dot) on the CW branch. Higher harmonic solutions are born via the same mechanism. Panels b)-d) show the eigenvalue spectrum at the Hopf bifurcations marked in a). At each Hopf bifurcation a pair of complex conjugate eigenvalues crosses the imaginary axis. The used parameters are $(\alpha_g, \alpha_a, \eta, \tau_1, s) = (0.5, 0.3, 0, 40, 5)$.

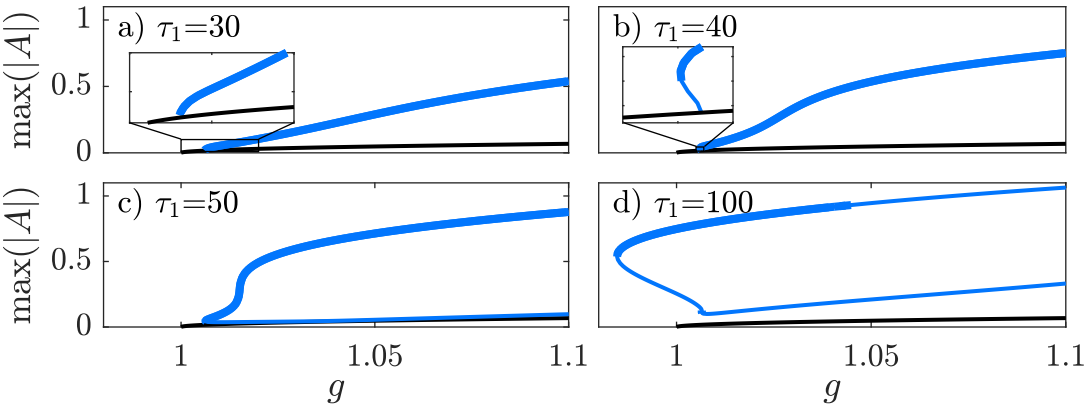

Figure 4.2: Bifurcation diagram of the FML solution of eqs. (3.26) to (3.28) for different values of τ_1. One can see the transition from a super- to a subcritical Hopf bifurcation on the CW branch in the insets of panels a) and b). Panels c) and d) show the detachment of the FML branch from the CW branch. In d) FML solutions exist below the lasing threshold such that one can speak of temporal LSs. Parameters as in fig. 4.1.

4.3. Influence of the Time Delayed Feedback

The introduction of time delayed feedback creates a train of satellite pulses for each pulse as shown in fig. 2.1. The position of satellites is determined by the length of the feedback loop τ_2 in relation to the length of the cavity τ_1 and their size is controlled by the feedback rate η. Figure 4.3 shows bifurcation diagrams in g of a FML solution in the localized regime for different values of η. The solution profile along each branch can be found as an animation in the supplementary material in appendix A. For high feedback rates ($\eta = 0.0109, 0.0105, 0.009$) the branches form closed loops and the LSs loose their stability in a Hopf bifurcation. These loops become smaller as larger η is. This indicates that feedback can have a destabilizing influence on the LSs and if the feedback is too strong no LSs exist at all. For weaker feedback, the range of existence of the LSs increases and they loose their stability in a Saddle-Node bifurcation (marked with F_s in fig. 4.3) instead of a Hopf bifurcation. In section 4.4 it is shown that the Saddle-Node bifurcation is in fact a SNIPER bifurcation and the destabilizing influence of the feedback is explained further. Weaker feedback also leads to a more complex dynamic at the low-power end of the branch (see $\eta = 0.004$ in fig. 4.3). In the limit of no feedback the SNIPER bifurcation disappears and the LSs loose their stability in a Hopf bifurcation again. This result is expected as in this case the system becomes equivalent to the system analyzed in [Mar+14; SJG18]. Intuitively, the satellites inherit their phase from the corresponding pulse. However, it is found that varying the feedback phase Ω has no influence on the stability of the LSs.

4.4. Scaling of the Period at the SNIPER-bifurcation

Figure 4.3 shows that in a certain parameter range FML solutions with satellites loose their stability in a Saddle-Node bifurcation. The value of the gain at which this bifurcation occurs will be referred to as the critical value $g_{0,cr}$. For g larger than $g_{0,cr}$ no stable localized FML solutions can be found. For a better understanding of the scenario, direct numerical simulations are performed in this regime. Figure 4.4 shows space-time diagrams for different values of the gain. It can be seen that for all three cases the location of the pulse jumps inside the cavity. The pulses always jump to the location where the satellite lived before. Hence, the satellite replaces the main pulse until it is replaced by its satellite and so on. This happens as by increasing the gain the satellites grow and deplete

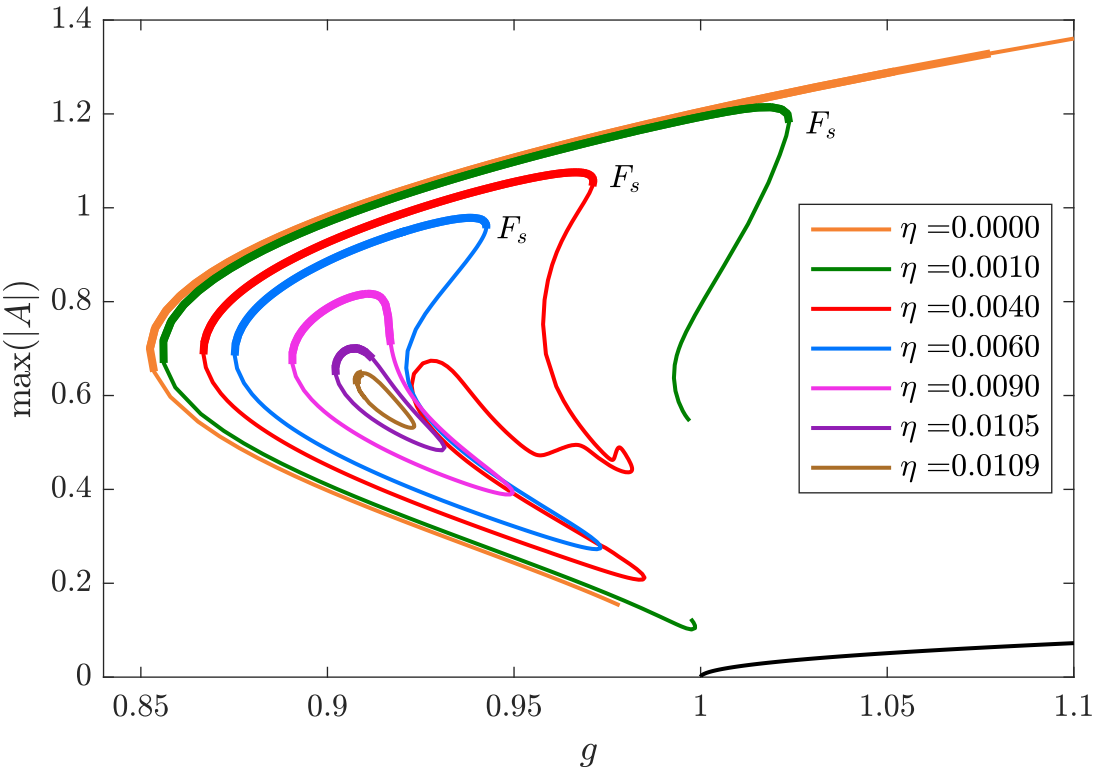

Figure 4.3: Bifurcation diagram of eqs. (3.26) to (3.28) of a FML solution for different values of η. Thick lines denote stable LSs while thin lines stand for unstable LSs. The thin black line in the bottom right is the CW branch for $\eta = 0.001$. Its stability is omitted in the plot. The branches for $\eta = 0.001$ and $\eta = 0$ end abruptly as `DDE-BIFTOOL` runs into numerical problems during their continuation. The solution profile along each branch can be found as an animation in the supplementary material in appendix A. Larger η decrease the range of existence and and thus, range of stability of the LSs. The branches for $\eta = 0.006, 0.004, 0.001$ loose their stability in a SNIPER bifurcation marked with F_s while on the other branches a Hopf bifurcation occurs. The used parameters are $(\alpha_g, \alpha_a, \tau_1, \tau_2, s) = (0, 0, 100, 80, 10)$. Note that as η changes also the value of the lasing threshold and hence, the norm of the axis of abscissas shifts by a small value for each branch.

the gain stronger such that the gain cannot fully recover before the main pulse arrives. This results in shrinking of the main pulse until, after a certain amount of round-trips, the satellite grows and becomes the new main pulse while the previous main pulse disappears. The insets in fig. 4.4c visualize the different steps of the process. Animations are provided in appendix A for a better visualization. The amount of time each pulse exists as a main pulse is referred to as the lifetime of a pulse. Comparing the three panels in fig. 4.4 indicates that the lifetime of the pulses is influenced by the gain. Figure 4.5 shows the time trace representation of fig. 4.4a from where the lifetime can easily be read of. Note that the replacement process is not triggered by noise but is inherent to the system. Therefore, the lifetime of the pulses is not arbitrary. It remains constant for each value of g in fig. 4.4. Hence, the solutions are periodic with the fundamental period T and as a secondary period with the lifetime of the pulses. Due to the lifetime being in the magnitude of several round-trips it is not possible to continue this solution with `DDE-BIFTOOL`. DNSs are used instead to track the solution in parameter space and find the bifurcation point where the solutions originate. This is visualized in fig. 4.6 where the FML branch is plotted together with results from DNSs such as fig. 4.5. It can be seen that the oscillating solutions originate in the Saddle-Node bifurcation F_s. Therefore, the bifurcation is global and its type cannot be determined by local approximation but by analyzing the scaling behavior of the period (the lifetime of the pulses in this case) as a function of the distance to the bifurcation point. In fig. 4.7 the lifetime of the pulses is plotted against the distances from the critical value $g_{0,cr}$ for different values of α_g and α_a. In both cases it can be seen that the data scales as $(g_0 - g_{0,cr})^{-1/2}$ which means that the bifurcation is a SNIPER bifurcation. If the data would scale as $-\log(g_0 - g_{0,cr})$ it would be a homoclinic bifurcation.

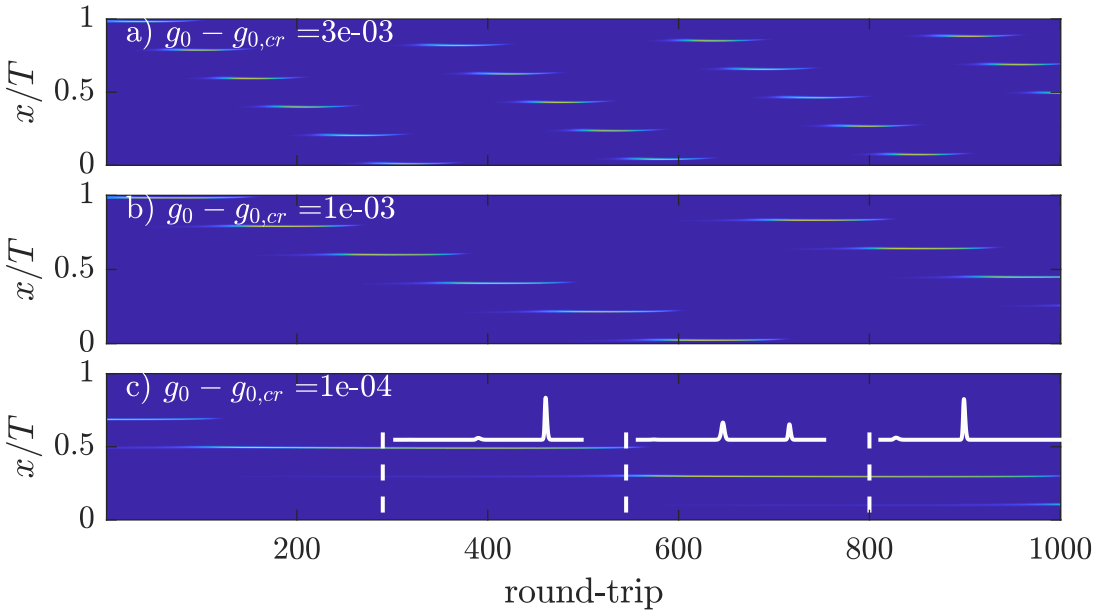

Figure 4.4: Space-time representation of a FML solution above the critical point $g_{0,cr} = 0.856 \cdot g_{0,\text{th}}$ where the SNIPER bifurcation occurs. The colorplot encodes the intensity $I = |A|^2$. One can observe that the lifetime of a pulse depends on the distance to the critical point. The insets in panel c) shall help to visualize the replacement process. Other parameters are $(\alpha_g, \alpha_a, \eta, \tau_1, \tau_2) = (0.01, 0, 0.006, 100, 80)$. The evolution of the solution along each space-time diagram can be found as an animation in the supplementary material in appendix A.

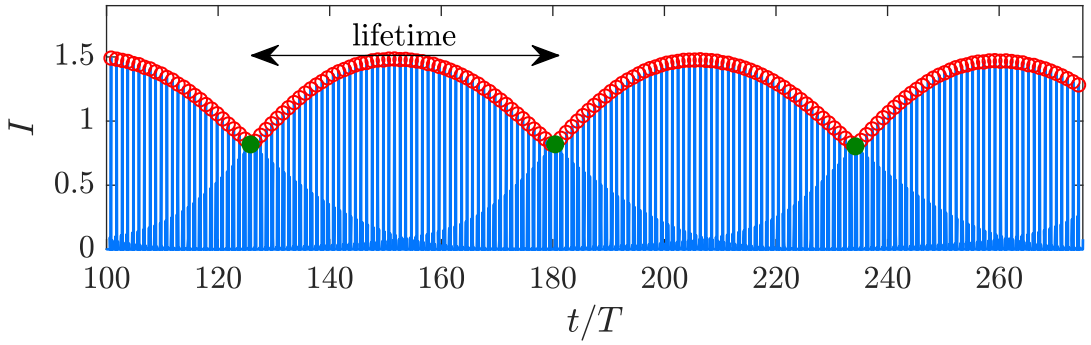

Figure 4.5: Extract of the dynamics presented in fig. 4.4a. The red circles indicate the maximal intensity in each round-trip while the green circles stand for the minimum of these maxima. Speaking differently, the green circles mark the points in time when the satellite pulses become larger than the main pulses. The distance between two of these points corresponds to the lifetime of a pulse which is analyzed in fig. 4.7.

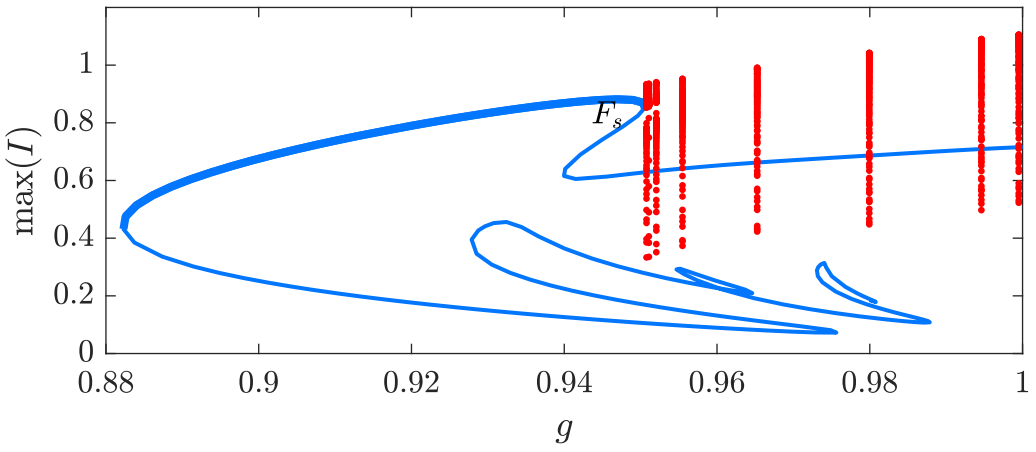

Figure 4.6: Bifurcation diagram of a FML solution of eqs. (3.26) to (3.28) for $(\alpha_g, \alpha_a, \eta, \tau_1, \tau_2) = (0.8, 0.5, 0.006, 100, 80)$. The blue line is obtained from path continuation while the red dots are results from DNSs and stand for the maximum intensity in each round-trip (compare red circles in fig. 4.5). The DNSs are conducted above the critical point F_s in the regime of satellite instability as shown in fig. 4.4.

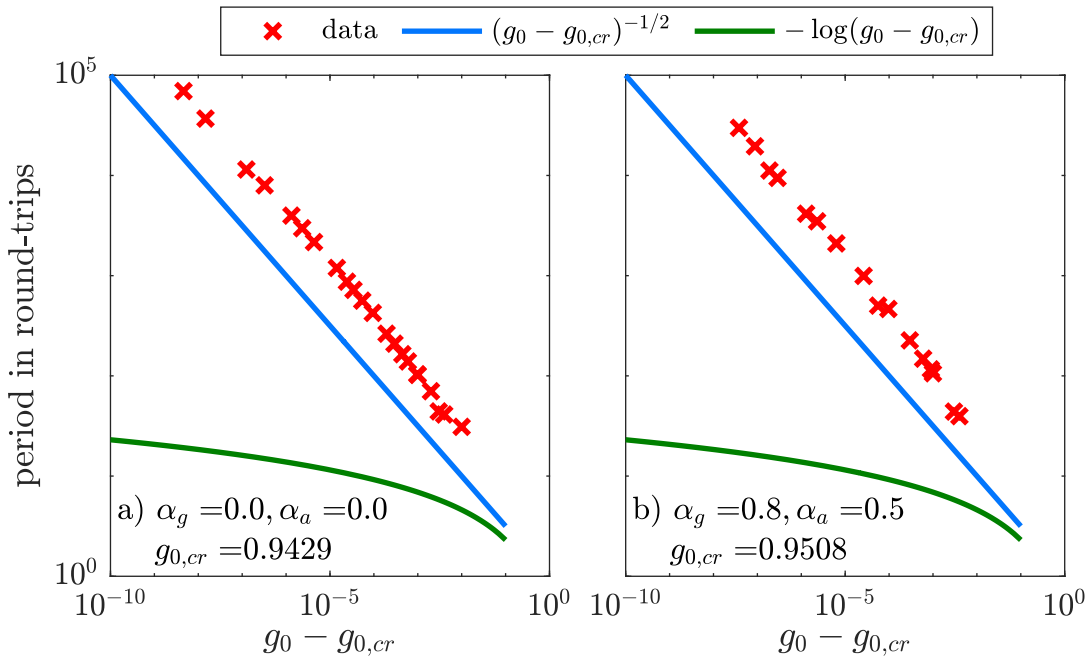

Figure 4.7: Lifetime of pulses as a function of the distance to the critical point $g_{0,cr}$ at which the global bifurcation (F_s in figs. 4.3 and 4.6) occurs. The lines correspond to the theoretically predicted scaling behavior for a homoclinic (green) as well as for a SNIPER (blue) bifurcation. One can see that the scaling of the lifetime is as $(g_0 - g_{0,cr})^{-1/2}$ which confirms that it is a SNIPER bifurcation. Parameters are $(\tau_1, \tau_2, \eta) = (100, 80, 0.006)$.

4.5. Excitability

In section 4.4 it is shown that the system can exhibit a satellite instability in which a pulse is recursively replaced by its satellite when operating the laser above the critical point $g_{0,cr}$. With no noise added to the system the lifetime of the pulses is approximately constant (see fig. 4.4). However, when introducing noise to the system the satellite instability exhibits dynamical behavior characteristics of excitable systems. The laser is operated close, yet below, the critical point $g_{0,cr}$. In order to trigger the replacement process of a main pulse a satellite must become sufficiently large such that the main pulse experiences less amplification and eventually shrinks. Noise can help or hinder this replacement process by adding or subtracting energy, respectively. In fig. 4.8 an exemplary run for a single pulse is displayed in both space-time and time trace representation. Due to the added noise the pulse eruptions become irregular and as a consequence the pulses have different lifetimes.

In fig. 4.9a statistical distribution of the length of the lifetime is displayed. For this, 3017 pulses are analyzed in the same way as presented in fig. 4.8. Because the replacement of the main pulse by its satellite takes a certain amount of time as growing and shrinking does not happen instantaneous, there is a lower border for the lifetime which is why very short survival length are not present. The rest of the statistics reveal that longer lifetimes are exponentially less likely to occur compared to shorter ones. Note that in this case an Euler method is used instead of a Runge-Kutta 4 scheme for the time integration because it is more robust against noise.

4.6. Two-Parameter Bifurcation Analysis

In fig. 4.3 it is shown that depending on the feedback rate the FML solution either looses its stability in a SNIPER or in a Hopf bifurcation. However, the transition between SNIPER and Hopf bifurcation can not only be triggered by varying η but also the linewidth enhancement factors α_g and α_a. These parameters are of relevance as generally in real-life systems they are non-zero.

Figure 4.10 shows bifurcation diagrams in g of a FML solution for different values of α_g while keeping $\alpha_a = 0$. It can be seen that for $\alpha_g = 0.1$ an additional unstable branch, which is not connected to the FML branch, exists. On this branch lies a Saddle-Node bifurcation F_a which collides with the main branch

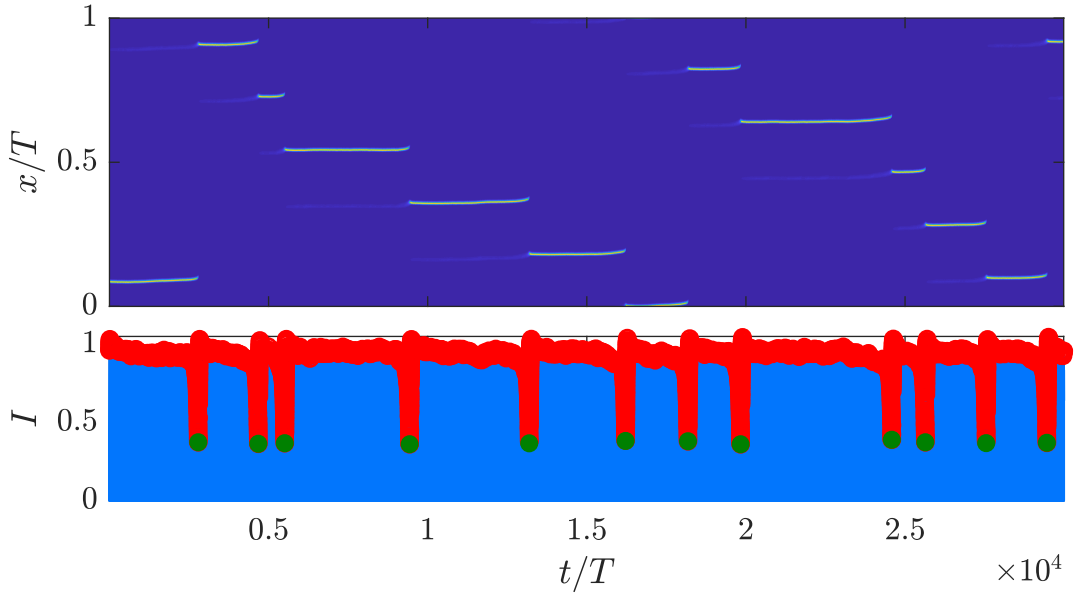

Figure 4.8: (Upper) Space-time and (lower) time representation of the evolution of a single initial pulse for the parameter set $(\alpha_g, \alpha_a, \eta, \tau_1, \tau_2, s, g) = (0.8, 0.5, 0.006, 100, 80, 10, 0.95)$ and noise of amplitude 8×10^{-3} obtained from a DNSs using an Euler method. In the lower plot the red circles denote the maximum in each round-trip. The green circles mark the minima of these points and thus, the points where the satellite pulse becomes larger than the main pulse (compare to fig. 4.5). Consequently, the distance between the green circles describes the lifetime of each pulse. The plotted data is only a small extract of a long simulation which analyses the lifetime of 3017 pulses. A statistical distribution of the different lifetimes can be seen in fig. 4.9.

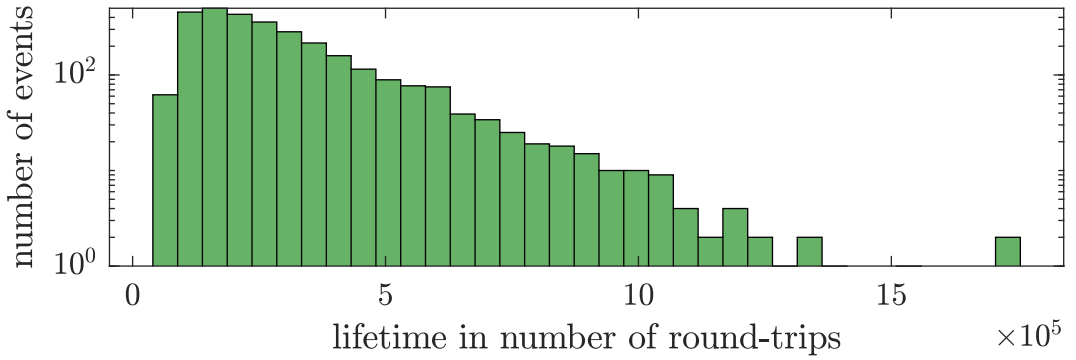

Figure 4.9: Statistical distribution of the lifetime of the pulses close the critical value $g_{0,\mathrm{cr}} = 0.9508$ in presence of noise. Very short lifetimes do not occur because the replacement process of a pulse takes a certain amount of time. Longer lifetimes are exponentially less likely to occur compared to shorter lifetimes. On the logarithmic scale the decay of the lifetime is approximately linear. Parameters as in fig. 4.8.

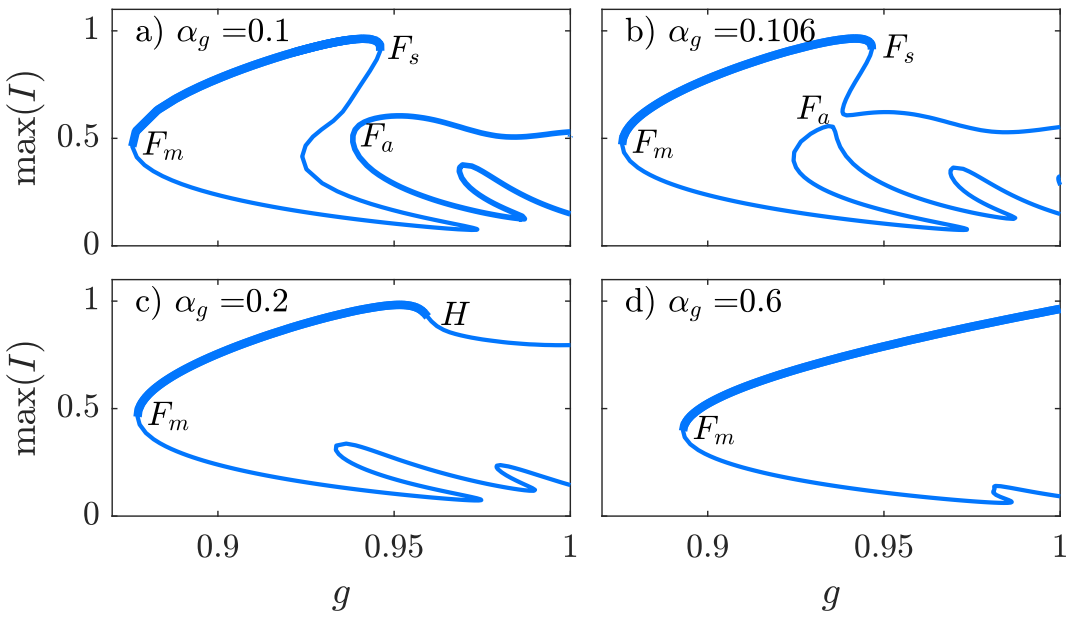

Figure 4.10: Bifurcation diagram of eqs. (3.26) to (3.28) for different values of α_g showing the transition between the SNIPER bifurcation denoted by F_s and Hopf bifurcation marked with H. The main fold F_m and the additional fold F_a are marked for reference in following figures. The used parameters are $(\alpha_a, \eta, \tau_1, \tau_2, s) = (0, 0.006, 100, 80, 10)$.

(see fig. 4.10b). The SNIPER bifurcation F_s remains unaffected by that. After a further increase to $\alpha_g = 0.2$ the SNIPER bifurcation F_s and the additional fold F_a have collided as well which enables a Hopf bifurcation denoted by H to form. With growing α_g the Hopf bifurcation moves towards larger gain values.

In order to track the bifurcation points quantitatively the two parameter plane (α_g, g) is regarded. Figure 4.11a,b shows the (α_g, g)-plane for different values of α_a. Note that only the main bifurcations points seen in fig. 4.10 are displayed because the dynamics becomes very complex especially on the unstable parts of the branches. For $\alpha_a = 0$ in fig. 4.11a the features discussed previously can be found as F_s and F_a collide in a so-called *cusp* bifurcation. The inset gives a zoomed view on the region of the cusp bifurcation and shows that the Hopf branch does not originate at the exact tip of the cusp but very close to it. Also, on the F_a branch there is another cusp bifurcation which lies exactly horizontal in the (α_g, g)-plane and corresponds to the collision between the branches in fig. 4.10a,b.

In fig. 4.11b the (α_g, g)-plane is displayed for $\alpha_a = 0.5$. The dynamics look very similar to the case $\alpha_a = 0$ in fig. 4.11a but the region of the SNIPER bifurcation is

shifted towards larger values of α_g. Between $\alpha_g \approx 0.5$ and $\alpha_g \approx 0.9$ the SNIPER bifurcation appears. Below and above this region the stability of the LSs is limited to the right by a Hopf bifurcation which originates in both cases close to a cusp of Saddle-Node bifurcations. This mechanism is completely analogue to the case $\alpha_a = 0$. Therefore, varying α_a corresponds to shifting the SNIPER bifurcation "up and down" in the (α_g, g_0)-plane.

Analogously, the left-right-shift can be triggered by changing η as seen in figs. 4.11b,c,d. In fig. 4.11c where $\eta = 0.004$, the region of the SNIPER bifurcation as well as the Hopf bifurcation occur at larger values of g compared to 4.11b where $\eta = 0.006$. This result corresponds to the findings in fig. 4.3 where it can be seen that the range of existence of LSs decreases when increasing η. As before, the SNIPER bifurcation collides with another fold in a cusp from where Hopf bifurcations emerge.

For $\eta = 0.009$ in fig. 4.11d there are more significant changes to the bifurcation diagram. First, a cusp-bifurcation appears on the Hopf branch for larger α_g. Next, the dynamics around the cusp bifurcations in which the SNIPER bifurcation emerges change as indicated by the insets. On the upper cusp, the Hopf bifurcation coexists with the SNIPER bifurcation much longer with respect to α_g compared to 4.11b and at the lower cusp bifurcation a second cusp bifurcation appears very close to the first one. The destabilizing bifurcations (SNIPER and Hopf bifurcation) move towards smaller gain values while the main fold F_m shifts to larger g resulting in a decreased range of stability.

A similar effect to increasing the feedback rate can be achieved by moving the satellite closer to the main pulse but still leaving pulse and satellite visible separately as shown in figs. 4.12g,h,i. This is again visualized in the (α_g, g)-plane in fig. 4.12a,b,c. For $\tau_2 = 90$ and $\tau_2 = 95$ the branches stay qualitatively similar to fig. 4.11b as all main features (F_m, F_s, F_a and H) and the corresponding cusps are still present. However, quantitatively the cusps around F_a move much closer towards each other. This behavior is similar to fig. 4.11d. For $\tau_2 = 97$ the cusps disappear and now the F_a branch goes all the way down to $\alpha_g = 0$. Again, this is very similar to fig. 4.11d. Further, comparing fig. 4.11b with fig. 4.12c reveals, that the range of stability decreases for larger τ_2 as F_s moves towards smaller g. However, that change is not as significant compared to an increased feedback rate as in fig. 4.11d. Moving the satellite even closer to the main pulse leads to a complex regime that will later be discussed in more detail.

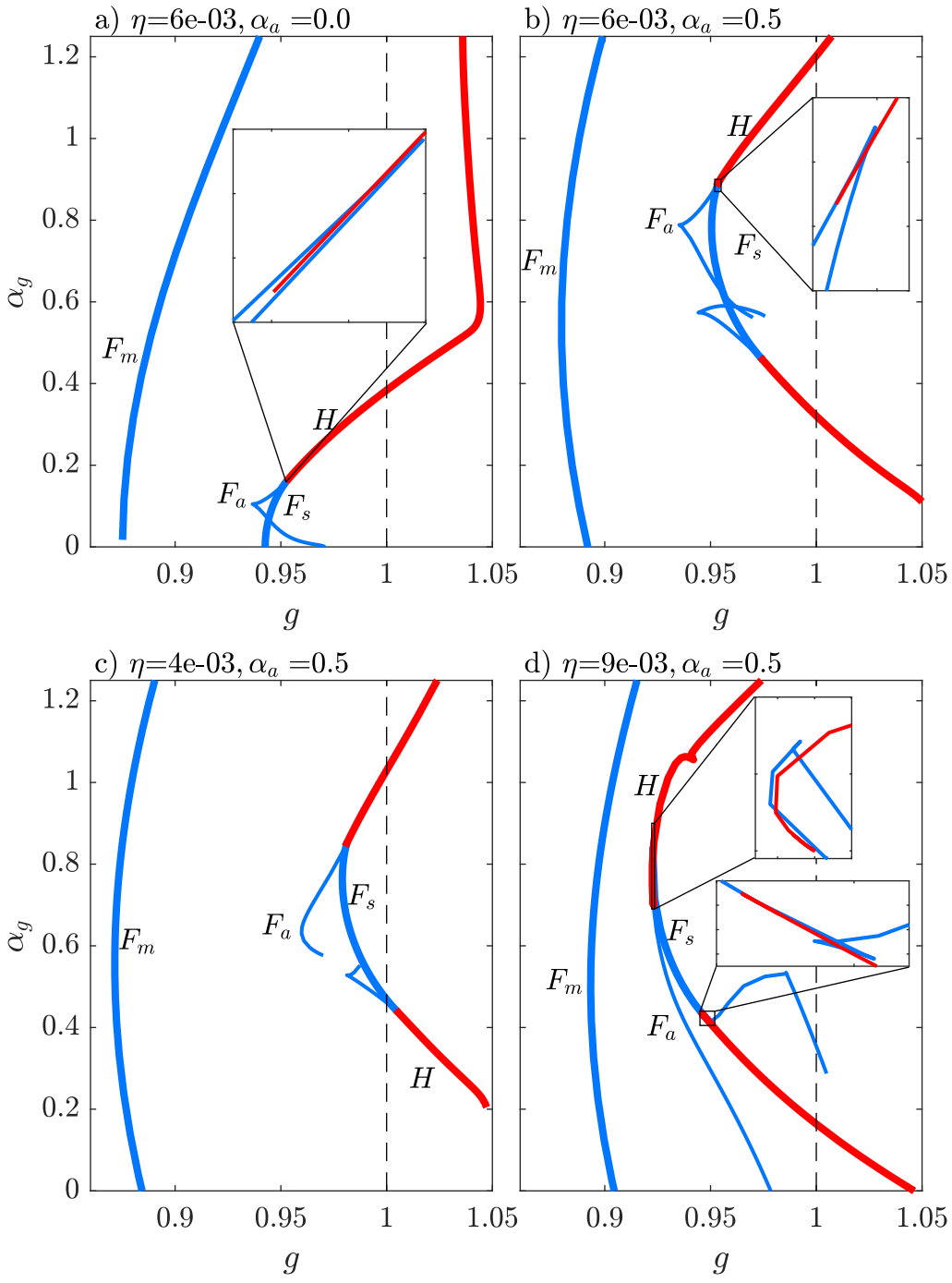

Figure 4.11: (α_g, g)-plane of eqs. (3.26) to (3.28) for different values of α_a and η, other parameters as in fig. 4.10. Blue lines stand for Saddle-Node bifurcations while red lines denote Hopf-bifurcations. The annotations refer to fig. 4.10 and explain which line corresponds to which bifurcation point. Thick lines denote the boundaries of stability for the FML solution. The insets give zoomed views on the area of cusp bifurcations and show that the Hopf bifurcation does not originate at the tip of the cusp. Further, one can see that α_a can be used to shift the dynamics up and down while η triggers a left and right movement.

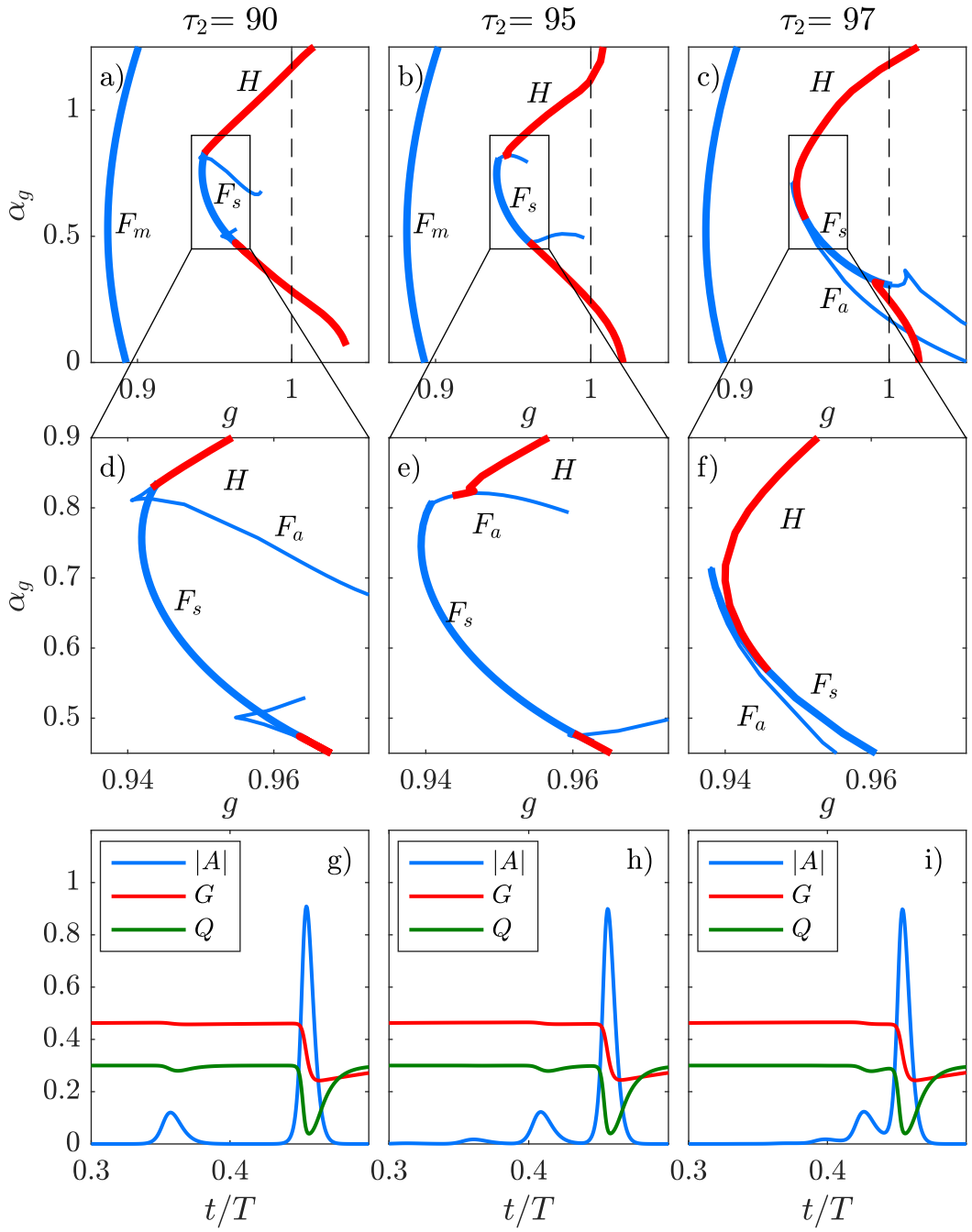

Figure 4.12: (α_g, g)-plane of eqs. (3.26) to (3.28) for FML solutions with $\tau_2 = 90$, $\tau_2 = 95$ and $\tau_2 = 97$. Other parameters are $(\alpha_a, \eta, \tau_1, s) = (0.5, 0.006, 100, 10)$. The thick lines denote the borders of stable LSs. The middle row of plots give a zoomed view of the area around the SNIPER bifurcation of the respective plot above. Note that for comparison in fig. 4.11b the same parameters have been used with $\tau_2 = 80$. The lowest panels show the profiles obtained from a direct numerical simulation for $g = 0.9, \alpha_g = 0.6$ and indicate that pulse and satellite are visible separately for $\tau_2 = 90, 95$ and begin to merge for $\tau_2 = 97$.

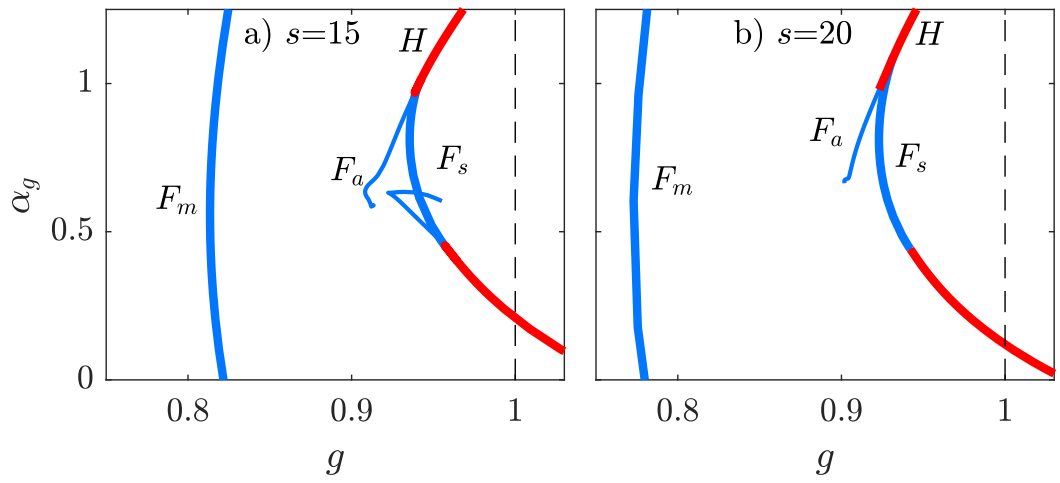

Figure 4.13: (α_g, g)-plane of eqs. (3.26) to (3.28) for FML solutions with $s = 15$ and $s = 20$. Blue lines stand for Saddle-Node bifurcations while red lines denote Hopf bifurcations. The used parameters are $(\alpha_a, \eta) = (0.5, 0.006)$. Note that for comparison in fig. 4.11b the same parameters have been used with $s = 10$. The thick lines denote the borders of stable LSs.

Another way to increase the range of stability is increasing the parameter s. If s is increased to $s = 15$ and $s = 20$, respectively, the range of stable LSs is increased significantly. The (α_g, g)-planes for $s = 15$ and $s = 20$ are displayed in fig. 4.13. The main fold F_m (as marked in figs. 4.10 and 4.11) shifts towards smaller g while the rest of the SN and Hopf bifurcations remain (approximately) at the same gain values.

4.7. Harmonic Solutions and Multistability

In the previous sections FML branches are analyzed in broad detail. However, in fig. 4.1 the existence of harmonic solutions is shown. These solutions consist of multiple pulses per round-trip and coexist with the FML branch. Hence, the system is multistable and the initial condition decides on which attractor the system settles.

In the first step feedback is turned off in order to gain a basic understanding of the HML branches. Figure 4.14a shows the according bifurcation diagram in g for harmonic solutions with up to five pulses per round-trip. First, it can be seen that the absolute value of the electric field becomes smaller as more pulses are in the cavity. This is because the gain does not fully recover before the next

pulse arrives and therefore provides less amplification. As more pulses are in the cavity as less the gain can recover. Next, the HML branches gain stability in a Hopf bifurcation which is in contrast to the FML branch where a Saddle-Node bifurcation stabilizes the branch.

When introducing time delayed feedback to the system the location of the satellite pulse plays an important role in the dynamics of the HML branches. So far, the satellites are placed further away from other pulses such that there is no direct interaction between pulses and satellites. However, when regarding a HML solution with five pulses in a cavity of length $\tau_1 = 100$ and the feedback delay is $\tau_2 = 80$ each pulse sits on a satellite of a neighboring pulse. This influence can be seen in fig. 4.14b where, as a result of this resonant feedback, the range of stability for the HML branch with five pulses is increased compared to fig. 4.14a. Also, the pulse intensity increases as the feedback reinforces the pulse. On the other hand, for non-resonant feedback, the range of stability decreases as feedback enables the instability to form in which a pulse is replaced by its satellite. This is described in section 4.4. As a result, the range of stability decreases as can be seen for the HML_2 and HML_3 branches in fig. 4.14b compared to fig. 4.14a.

The same mechanisms apply when choosing $\tau_2 = 50$ as seen in fig. 4.14c. In this case, the HML_2 and HML_4 branches are favored due to resonant feedback. A further effect which becomes visible is the second order feedback for the FML branch. For $\tau_1 = 100$ and $\tau_2 = 50$ a pulse sits on the second order satellite of the previous pulse which gives the branch a wider range of stability compared to fig. 4.14b. A further remark to fig. 4.14 is that stable harmonic solutions with more than four pulses only exist above the threshold and are therefore not truly localized. This can strongly be influenced by the parameter s. Figure 4.15 shows branches in g of a HML_5 solution for different values of s. For $s = 10$ the solution only exists above the threshold. However, increasing s moves the stable regions below the threshold and therefore creates LSs. This process also triggers a transition from a supercritical to a subcritical Hopf bifurcation on the CW branch similar to what is shown in fig. 4.2.

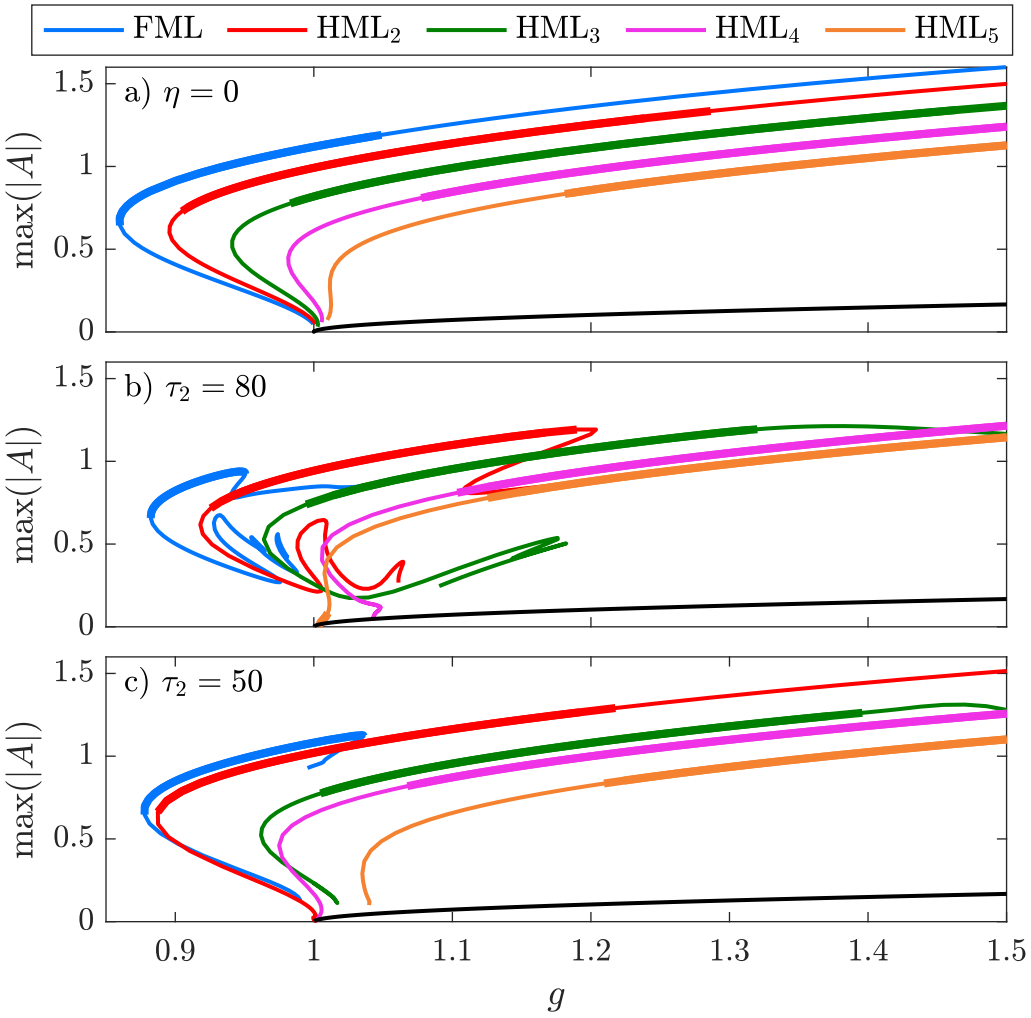

Figure 4.14: Bifurcation diagrams of eqs. (3.26) to (3.28) in g for the FML branch and harmonic solutions with two up to five pulses per round-trip. In panel a) feedback is turned off, while in b) and c) the location of satellites defined by τ_2 is changed. The black line at the bottom corresponds to the CW branch. The used parameters are $(\alpha_g, \alpha_a, \eta, \tau_1, s) = (0.8, 0.5, 0.006, 100, 10)$. Resonant feedback increases the range of stability of the respective branches as seen in b) for the HML_5 branch and in c) for the HML_2 branch.

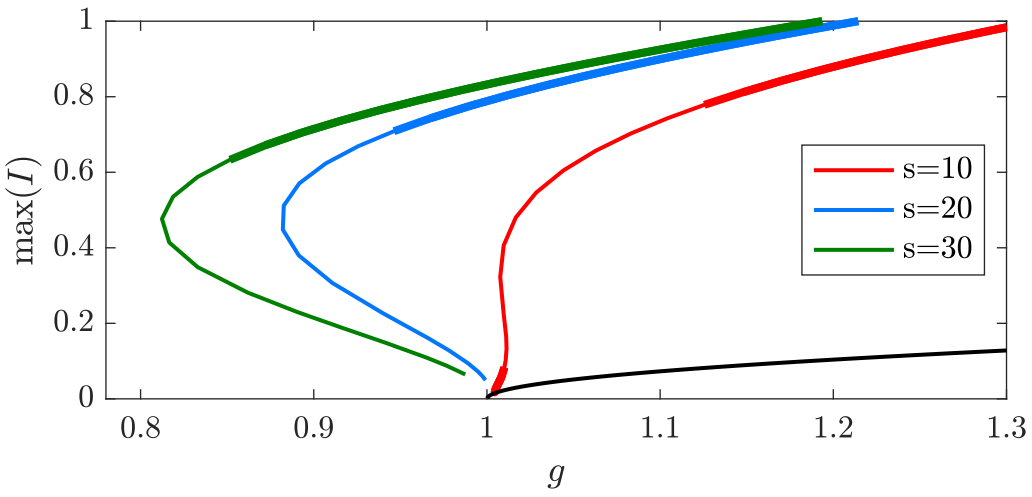

Figure 4.15: Bifurcation diagram of eqs. (3.26) to (3.28) in g of a HML_5 solution. Branches for different values of s are displayed. For $s = 10$ stable solutions exist only above the threshold. Increasing s moves the range of stability below the threshold. The used parameters are $(\alpha_g, \alpha_a, \eta, \tau_1, \tau_2) = (0.8, 0.5, 0.006, 100, 80)$.

4.8. Pulse Dynamics around the Resonances

Section 4.7 highlights that resonant feedback can increase the range of stability of the mode-locked states. Next, the transition from non-resonant to resonant needs to be understood. Therefore, it is instructive to regard the two parameter plane (τ_2, g) in fig. 4.16a. To help understanding the diagram, bifurcation diagrams in g for different values of τ_2 are shown in fig. 4.16b-g. Here, red lines stand for FML branches while green lines correspond to HML_2 branches. Starting at $\tau_2 = 146$, a stable region exists for both branches. However, that changes for $\tau_2 = 147$ where the HML_2 branch is unstable. Placing the satellite close to the main pulse does not give the gain enough time to fully recover and thus, the solution becomes unstable. The HML_2 branch regains stability for $\tau_2 = 149$. Values above the resonance at $\tau_2 = 150$ do not lead to unstable branches because a satellite which is placed behind the pulse (in temporal sense) does not "steal" amplification from the main pulse and therefore does not destabilize it.

Another important feature which emerges around the resonance is that the FML and HML_2 branches are connected by a period doubling (PD) bifurcation. To be more precise, the FML branch emerges from a point on the HML_2 branch just by doubling the period from $T \approx \tau_1/2$ to $T \approx \tau_1$. Thus, at this point, the solution profile consists of two pulses of same height. On the FML branch one of

the pulses grows and the other becomes its satellite while on the HML2 branch both pulses remain the same height. This corresponds exactly to the situation described in fig. 2.9. Animations of the solution profiles along all displayed branches are provided in appendix A. The PD bifurcation first emerges at $\tau_2 = 147$ on the low-power end of the branch. For $\tau_2 = 149$ the PD bifurcation is also on the high power end of the branch. In fact, it is the bifurcation in which the HML_2 branch gains stability. The PD bifurcation disappears for $\tau_2 > 151$. This can be seen in the (τ_2, g)-plane in fig. 4.16a. Here, the resonance is visible as the Saddle-Node bifurcations $F_{m,1}$ and $F_{m,2}$ (main folds of FML and HML_2 branches, respectively) shift to smaller values of g around $\tau_2 = 150$. $F_{m,2}$ is more affected because for the FML branch the resonance is only of second order. Interestingly, also a transition between SNIPER and Hopf bifurcations can be seen around the resonance where similar to fig. 4.11 the Hopf bifurcation emerges close to a cusp point of Saddle-Node bifurcations.

Figure 4.17 shows the (τ_2, g)-plane for a much wider range in τ_2 than before. Again, one can see the resonance of first order at $\tau_2 = 100$, of second order at $\tau_2 = 50$ and even third order at $\tau_2 = 66$ as bumps on the F_m branch. Generally, the SNIPER bifurcation F_s moves towards larger values of g the smaller τ_2 becomes creating a broader range of stable LSs which is similar to changing the feedback rate as seen in fig. 4.3. However, at the resonant values of $\tau_2 = 50, 66$, small kinks can be found on the branch. Naturally, both, the bumps on the F_m branch and kinks on the F_s branch, become smaller the higher the order is. Around the first order feedback at $\tau_2 = 100$, `DDE-BIFTOOL` ran into numerical problems while performing continuations of the destabilizing bifurcations. Therefore, this region is further analyzed with DNSs in section 5.2.4. Panels b)-d) in fig. 4.17 reveal another feature of the system which emerges at the resonance. The system prefers to be in a resonant state and therefore can adapt its properties (namely the period, intensity and pulse width) accordingly. For τ_2 slightly smaller than $\tau_1 = 100$, the period decreases, while for τ_2 slightly larger than $\tau_1 = 100$ the period increases. At the same time, the pulse width (defined as the full width at half maximum) becomes larger in both cases as the pulse wants to incorporate the satellite. A wider pulse results in a smaller maximum intensity as seen in fig. 4.17c. However, at perfect resonance at $\tau_2 \approx \tau_1$, the maximum intensity quickly increases while the pulse width decreases. The second and third order resonances reveal the same properties but with a smaller magnitude.

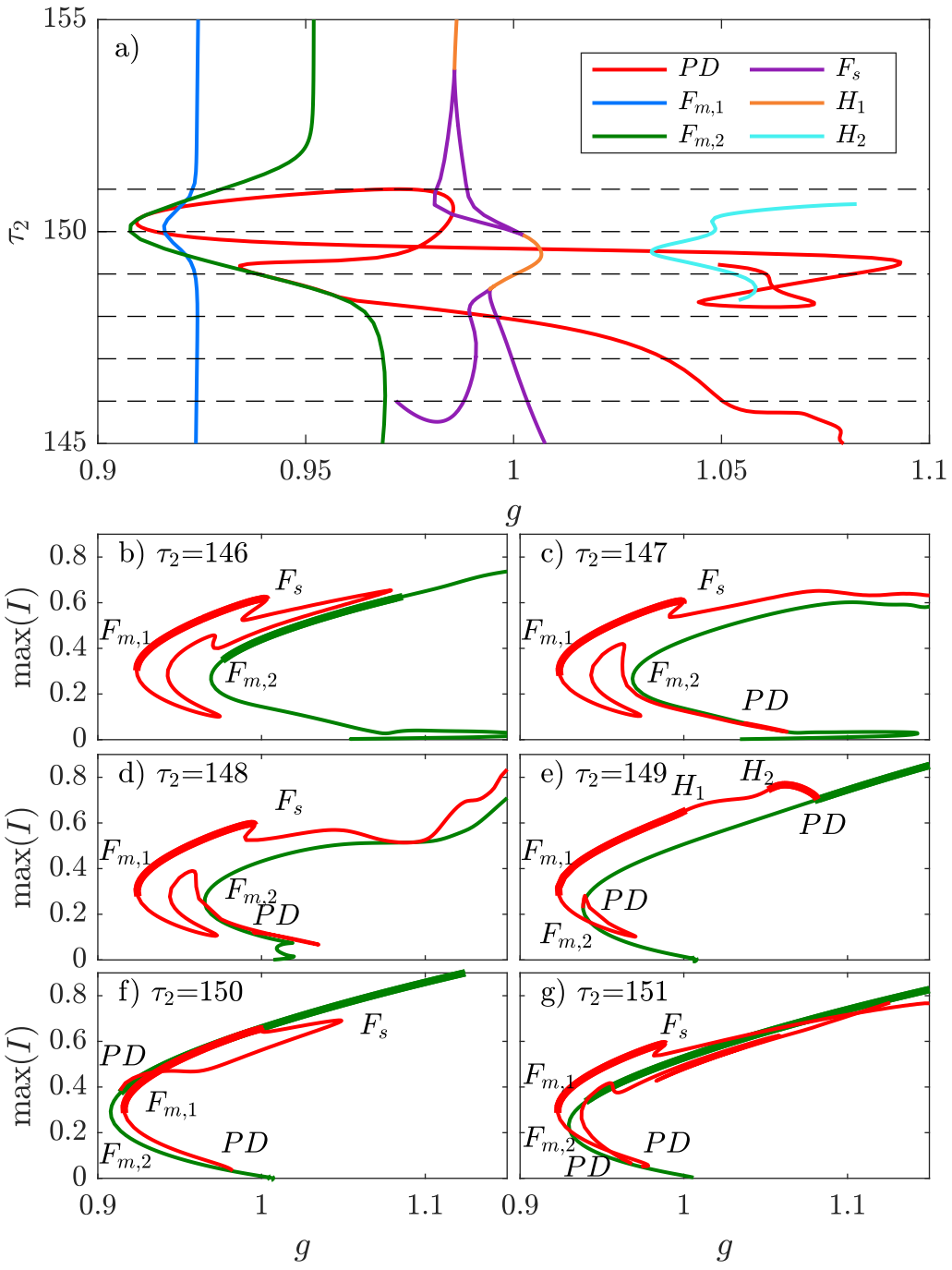

Figure 4.16: Bifurcation diagrams of eqs. (3.26) to (3.28). Panel a) shows the (τ_2, g)-plane around the area of resonant feedback. The branches shown correspond to a period doubling bifurcation (PD), the main folds of the FML and HML$_2$ branches ($F_{m,1}, F_{m,2}$), respectively, the SNIPER bifurcation (F_s), and two Hopf bifurcations (H_1, H_2). The dashed lines indicate the cross section at which the bifurcation diagrams in panels b)-g) are plotted. In these panels the bifurcation points mentioned above are marked. The red line stands for the FML branch, while the green line corresponds to the HML$_2$ branch. Thick lines denote stable solutions while thin lines stand for unstable states. The used parameters are $(\alpha_g, \alpha_a, \eta, \tau_1, s) = (1.5, 0.5, 0.009, 100, 10)$, other parameters as before. The solution profiles along each branch in b)-g) can be found as an animation in the supplementary material in appendix A.

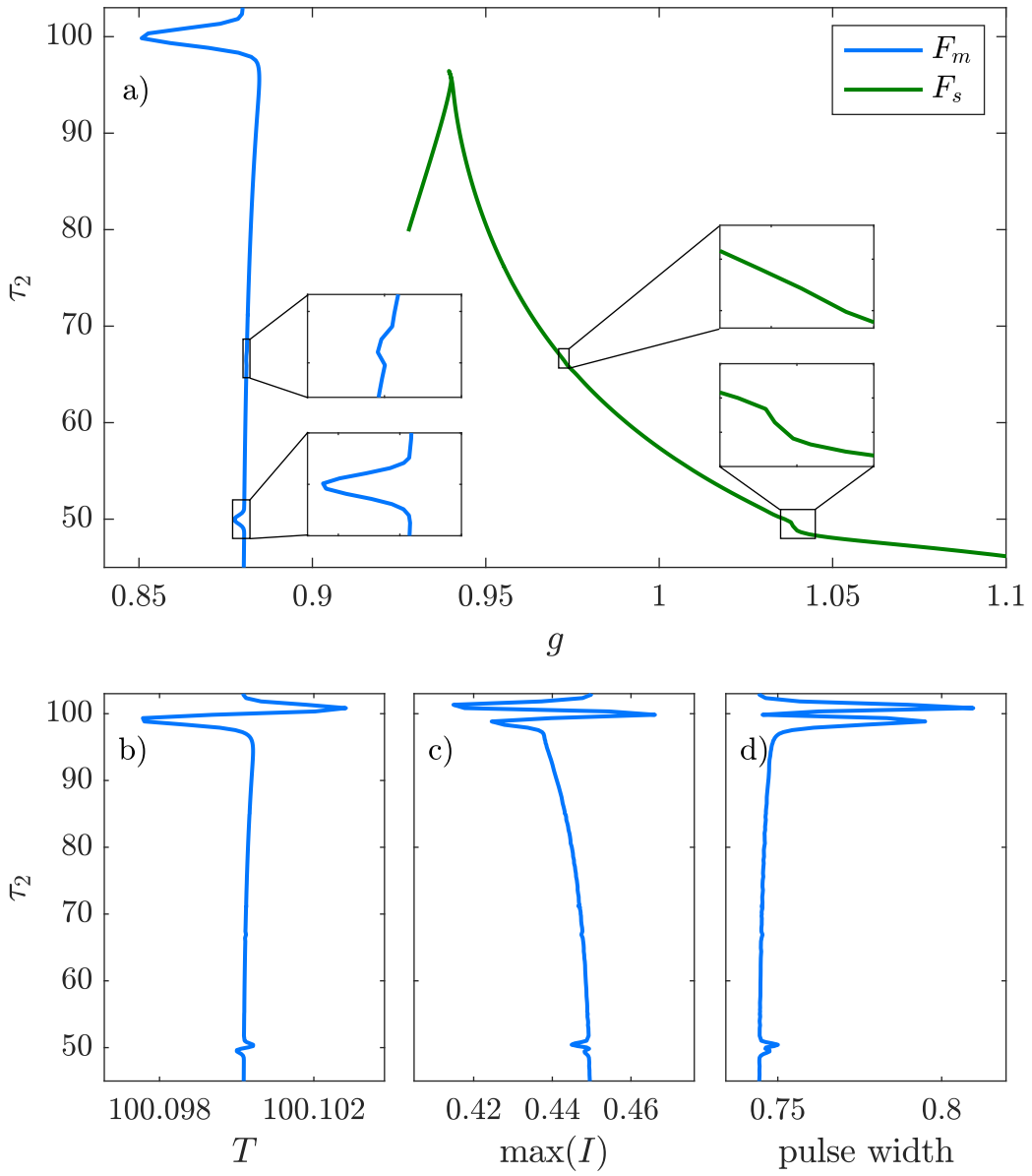

Figure 4.17: a) Evolution of the main fold (blue) and the SNIPER bifurcation (green) in the (τ_2, g)-plane for the FML solution. The insets give zoomed views on the areas where the satellite pulses interact with a main pulse. The lower panels show how b) the period, c) the maximal intensity and d) the pulse width evolve along the main fold F_m displayed in a). The pulse width is defined as the full width at half maximum (FWHM). Panel b) shows that the system adapts to the feedback as the period quickly changes around the resonances. Also the intensity and the pulse width are adapted accordingly around the resonance. The solution profile along the main fold can be found in an animation in the supplementary material in appendix A. The used parameters are $(\alpha_g, \alpha_a, \eta, \tau_1, s) = (0.8, 0.5, 0.006, 100, 10)$, other parameters as before.

5. Transition between Coherent and Incoherent Pulses

In section 4.7 it is shown that time delayed feedback can favor the existence and stability of certain harmonic solutions when the feedback is resonant in the sense that the satellite of a pulse corresponds to the next pulse (see fig. 4.14). Via this mechanism a direct link between the pulses can be created which can be used to lock their relative position. This effect is counteracted by external noise which can influence the position of the pulses. A further property of a train of pulses is defined by their phase relation. Two pulses are called *coherent* if they exhibit the same frequency and have a constant phase difference. The coherence can be quantified by the cross-correlation function of the two pulses [LK93]. For the trains of pulses analyzed in this thesis, the phase of each pulse changes arbitrarily when noise is present. Thus, an initially coherent train of pulse can become incoherent after some time. This section focuses on the question whether the coherence of a series of pulses can be maintained by using time delayed feedback and if so, how it is influenced by the system parameters.

A theoretical framework is provided by the *Kuramoto model* [Kur75]. It describes a simple model of N mutually coupled oscillators having different natural frequencies ω_k. The dynamics of the phase of each oscillator ϕ_k is governed by

$$\frac{d\phi_k}{dt} = \omega_k + \frac{\epsilon}{N}\sum_{j=1}^{N}\sin(\phi_j - \phi_k), \tag{5.1}$$

where ϵ is the coupling strength. Note that the coupling is proportional to N^{-1} in order to ensure that with a growing number of oscillators the force on each oscillator remains constant for given ϵ [PRK01].

However, in the case of pulses coupled by time delayed feedback, the coupling only exists between neighboring pulses. Anyways, a measure for the amount of synchronization between the pulses needs to be found. Following the Kuramoto model the order parameter b is introduced. For each round-trip it is defined as

$$b = \frac{1}{N}\sum_{j=0}^{N-1} e^{i(\phi_{j+1}-\phi_j)}, \tag{5.2}$$

where N is the number of pulses per round-trip and ϕ_j is the phase of the j-th pulse. Note that ϕ_0 is the phase of the last pulse in the previous round-trip. For

the order parameter the phase difference $\phi_{j+1} - \phi_j$ is chosen instead of the pure phase ϕ_j because one is only interested in whether the pulses are coherent. For this, only the phase difference and not the value of ϕ_j plays a role. In fact, the value of ϕ_j is strongly influenced by the feedback phase Ω, whereas Ω has no influence on the phase difference.

The order parameter encodes two information. First, $|b|$ is a measure for the amount of synchronization of the pulses in the cavity. In particular, $|b| = 1$ means that a train of pulses is coherent while for $|b| = 0$ the pulses are incoherent. Second, when writing $b = |b|e^{i\varphi}$, φ stands for the median phase difference of all pulses.

5.1. Derivation of Order Parameter Equation

In the following a simplified theoretical framework of coupled oscillators is presented in order to find an explicit expression for the order parameter as a function of feedback and noise. Each oscillator has a certain phase ϕ_i and a location x_i that are coupled by forces A and B, respectively. Here, A and B are functions of the coupling strength η. In a simple model the oscillators can be described as

$$\frac{d\phi_i}{dt} = A(\eta)\cos(x_{i-1} - x_i + \Omega)\sin(\phi_{i-1} - \phi_i + \psi) + \xi(t), \tag{5.3}$$

$$\frac{dx_i}{dt} = B(\eta)\cos(\phi_{i-1} - \phi_i + \psi)\sin(x_{i-1} - x_i + \Omega) + \xi(t), \tag{5.4}$$

where Ω and ψ are constant offsets and $\xi(t)$ is additional noise. To simplify these coupled equations one assumes that the location of each oscillator is constant and thus eqs. (5.3) and (5.4) simplify to

$$\frac{d\phi_i}{dt} = A(\eta)\sin(\phi_{i-1} - \phi_i + \psi) + \xi(t). \tag{5.5}$$

Without noise the steady states of the system would simply be $\phi_j = j\psi$. In the presence of noise it makes sense to express the phase as a deviation θ_j of these steady states:

$$\phi_j = j\psi + \theta_j. \tag{5.6}$$

Plugging this in eq. (5.5) yields for the deviation

$$\begin{aligned}\frac{d\theta_i}{dt} =& A(\eta)\sin(\theta_{i-1}-\theta_i+(i-1)\psi-i\psi+\psi)+\xi(t)\\ =& A(\eta)\sin(\theta_{i-1}-\theta_i)+\xi(t).\end{aligned} \tag{5.7}$$

Next, the deviation can be described as a continuous function θ by expanding eq. (5.7) for shallow modes

$$\begin{aligned}\frac{d\theta_i}{dt} \simeq& A(\eta)(\theta_{i-1}-\theta_i)+\xi(t)\\ \Rightarrow\ \frac{\partial\theta}{\partial t} =& A(\eta)\left(-\Delta x\frac{\partial\theta}{\partial x}+\frac{\Delta x^2}{2}\frac{\partial^2\theta}{\partial x^2}+\mathcal{O}(\Delta x^3)\right)+\xi(t),\end{aligned} \tag{5.8}$$

where $\Delta x = \frac{L}{N}$ and L is the length of the cavity. For simplification, the parameters are rescaled as $v = A(\eta)\Delta x$ and $D = A(\eta)\frac{(\Delta x)^2}{2}$. Also the time is rescaled as $\tilde{t} = Dt$. When dropping the drift $v\partial_x\theta$ one obtains

$$\partial_{\tilde{t}}\theta = \partial_x^2\theta + \frac{\xi(x,t)}{D}. \tag{5.9}$$

The noise is assumed to be δ-correlated, white and of variance σ, i.e., $\xi(x,t) = \sigma\tilde{\xi}(x,t)$, where

$$\langle\tilde{\xi}(x,t),\tilde{\xi}(x',t')\rangle = \delta(t-t')\,\delta(x-x'). \tag{5.10}$$

Next, the coupling force is linearly approximated $A(\eta) = \tilde{A}\cdot\eta$. Plugging everything in eq. (5.9) and dropping all tildes yields

$$\begin{aligned}\partial_t\theta =& \partial_x^2\theta + \frac{\sigma}{D}\xi(x,t)\\ =& \partial_x^2\theta + \underbrace{\frac{2}{A}\frac{\sigma}{\eta}\frac{N^2}{L^2}}_{=:c}\xi(x,t).\end{aligned} \tag{5.11}$$

Equation 5.11 is a linear diffusion equation with noise which can be solved in the Fourier space. The Fourier transforms are denoted by a hat symbol. In Fourier space, 5.11 reads

$$\frac{d\hat{\theta}_k}{dt} = -k^2\hat{\theta}_k + c\hat{\xi}_k. \tag{5.12}$$

for each mode k. However, it is sufficient to consider only one mode as all equations are linear. In the end, the temporal average is of interest which is given by:

$$\bar{X} = \langle X \rangle = \frac{1}{T}\int_0^T X(t)dt. \tag{5.13}$$

It is useful to apply Parseval's theorem together with the fact that $\langle \partial_t \hat{\theta} \rangle = 0$

$$\langle \int dx \left|\theta\left(x\right)\right|^2 \rangle = \langle \int dq \left|\hat{\theta}\left(q\right)\right|^2 \rangle = \int dq \frac{c \cdot \langle \left|\hat{\xi}\right|^2 \rangle}{q^2}. \tag{5.14}$$

If the solution is dominated by the long-wavelength mode, the solution can be found as a convolution integral for the temporal part. Setting the fundamental wavenumber $k_0 = \frac{2\pi}{L}$ yields

$$\theta\left(x,t\right) = f\left(t\right)\sin\left(k_0 x\right) \tag{5.15}$$

with

$$\begin{aligned} f\left(t\right) &= \int_{-\infty}^{t} c\xi_{k_0}\left(t'\right) e^{-k_0^2(t-t')} dt' \\ &= \int_{-\infty}^{t} c\xi_{k_0}(t-t') e^{-k_0^2 t'} dt'. \end{aligned} \tag{5.16}$$

This expression corresponds to a low pass filtering of the spatial component of the white noise spectrum at the frequency k_0. Next, the integral definition of the Bessel function

$$J_n\left(\sigma\right) = \frac{1}{2\pi}\int_{-\pi}^{\pi} e^{i(\sigma\sin\tau - n\tau)} d\tau \tag{5.17}$$

is used. From the approximate solution in eq. (5.15) and by using eq. (5.16), the order parameter b can be expressed as a function of the first Bessel function as

$$
\begin{aligned}
b(t) &= \frac{1}{L}\int_{-L/2}^{L/2} e^{i\theta(x,t)}dx \\
&= \frac{1}{L}\int_{-L/2}^{L/2} e^{if(t)\sin(k_0 x)}dx \\
&= \frac{1}{2\pi}\int_{-\pi}^{\pi} e^{if(t)\sin z}dz \\
&= J_0\left[f(t)\right] \\
&= 1 + J_0^{'} f(t) + \frac{J_0^{''}}{2} f^2(t) + \frac{J_0^{'''}}{6} f^3(t) + \mathcal{O}(f^4) \\
&= 1 - \frac{f^2(t)}{4} + \mathcal{O}\left(f^4\right).
\end{aligned} \tag{5.18}
$$

From this explicit relation between $b(t)$ and $f(t)$, one can find the temporal average of the order parameter as

$$
\begin{aligned}
\bar{b} &= 1 - \frac{1}{4}\langle f^2(t)\rangle \\
&= 1 - \frac{1}{4}\langle\left[\int_0^\infty c\cdot\xi_{k_0}(t-u)\,e^{-k_0^2 u}du\right]\left[\int_0^\infty c\cdot\xi_{k_0}(t-v)\,e^{-k_0^2 v}dv\right]\rangle \\
&= 1 - \frac{1}{4}\langle\iint_0^\infty c^2\cdot\xi_{k_0}(t-u)\,\xi_{k_0}(t-v)\,e^{-k_0^2(u+v)}dudv\rangle \\
&= 1 - \frac{c^2}{4}\iint_0^\infty\langle\xi_{k_0}(t-u),\xi_{k_0}(t-v)\rangle e^{-k_0^2(u+v)}dudv \\
&= 1 - \frac{c^2}{4}\int_0^\infty e^{-2k_0^2 u}du \\
&= 1 - \frac{c^2}{8k_0^2} \\
&= 1 - \frac{1}{8\pi^2 A^2}\frac{\sigma^2 N^4}{\eta^2 L^2}.
\end{aligned} \tag{5.19}
$$

From eq. (5.18) one can see that when considering $|\bar{b}|^2$ up to an order of $\mathcal{O}(f^4)$ one only has to add a factor of two

$$
\begin{aligned}
|\bar{b}|^2 =& 1 - \frac{1}{4\pi^2 A^2}\frac{\sigma^2 N^4}{\eta^2 L^2} \\
=& 1 - a\frac{\sigma^2 N^4}{\eta^2 L^2},
\end{aligned} \tag{5.20}
$$

where a is a constant which needs to be determined.

5.2. Numerical Results

The next step is to analyze whether eq. (5.20) derived in the previous section applies for the full system defined by eqs. (3.26) to (3.28). In order to do so DNSs of harmonic solutions are performed. Finally, one tries to verify the scaling behavior of the order parameter. As the influence of noise on the system is analyzed one can only perform a statistical analysis. Therefore, the simulations need to be reasonably long in order produce significant results. Another difficulty is that noise can lead to the destruction of the harmonic solution and the system might become stuck at another attractor, usually a harmonic solution with fewer pulses per round-trip. To tackle both problems in the following each data point consists of 200 000 round-trips which are split in 10 runs of 20 000 round-trips each. The system is initialized with a set of pulses which are in phase. As the system needs to settle from the initial state to a stable attractor, out of the 20 000 round-trips in each run the first 2000 are discarded. From the rest of the time traces the desired values are obtained and averaged. From the same data the variance is computed.

5.2.1. Influence of Feedback and Noise on the Order Parameter

Figure 5.1 shows time traces of harmonic solutions with five pulses for different values of the feedback strength η. Panels a), b) and c) show the evolution of the relative phase of the pulses, panels d), e) and f) of the relative position and panels g), h) and i) of the order parameter defined in eq. (5.2). Animations of each time are provided in appendix A. For $\eta = 0$ the pulses are not coupled to each other and thus, the relative phase evolves randomly with noise (see fig. 5.1a). The relative position (see fig. 5.1d) is only coupled by the nature of the harmonic solution. Thus, the pulses are confined to $x_j - x_{j-1} = \frac{1}{N} = 0.2$ but the variance is much larger compared to the case with external feedback (see figs. 5.1e,f). Also, figs. 5.1b,c indicate that the relative phase of the pulses can be locked to zero with the introduction of external feedback. As higher the feedback is, the lower are the fluctuations in the relative phase are. Note that in general a relative phase of zero does not mean that the phase of each pulse is zero. The absolute phase is strongly influenced by the feedback phase Ω.

As all the relative phases for $\eta = 0$ evolve randomly, the order parameter decreases over time (see fig. 5.1g). The fact, that it is close to one for some time, is due to the coherent initial state. For nonzero η the order parameter is very

close to one. A stronger feedback also decreases the fluctuations (fig. 5.1h,i). However, the exact value of the order parameter not only depends on η but also on the amplitude of the noise σ. This can be seen in figs. 5.3a,b where the order parameter is plotted against η for different values of σ. For $\sigma = 7 \times 10^{-3}$ a small feedback of around $\eta = 2 \times 10^{-3}$ is already sufficient to reach an order parameter $|b|^2 \approx 1$ while for $\sigma = 7 \times 10^{-2}$ the feedback rate needs to be much higher. At the same time, smaller noise leads to much lower fluctuations on the relative location of the pulses as can be seen in figs. 5.3c,d. The result of plotting the order parameter against the noise amplitude for fixed η (see fig. 5.4) fits to the features described before. When the noise amplitude is small, small feedback is sufficient to provide synchronization. As stronger the feedback strength is, the larger the noise amplitude needs to be in order to destroy coherent states. Regarding the position of the pulses, one can see that increasing the noise amplitude leads to a larger variance. The variance grows quicker when the feedback is smaller.

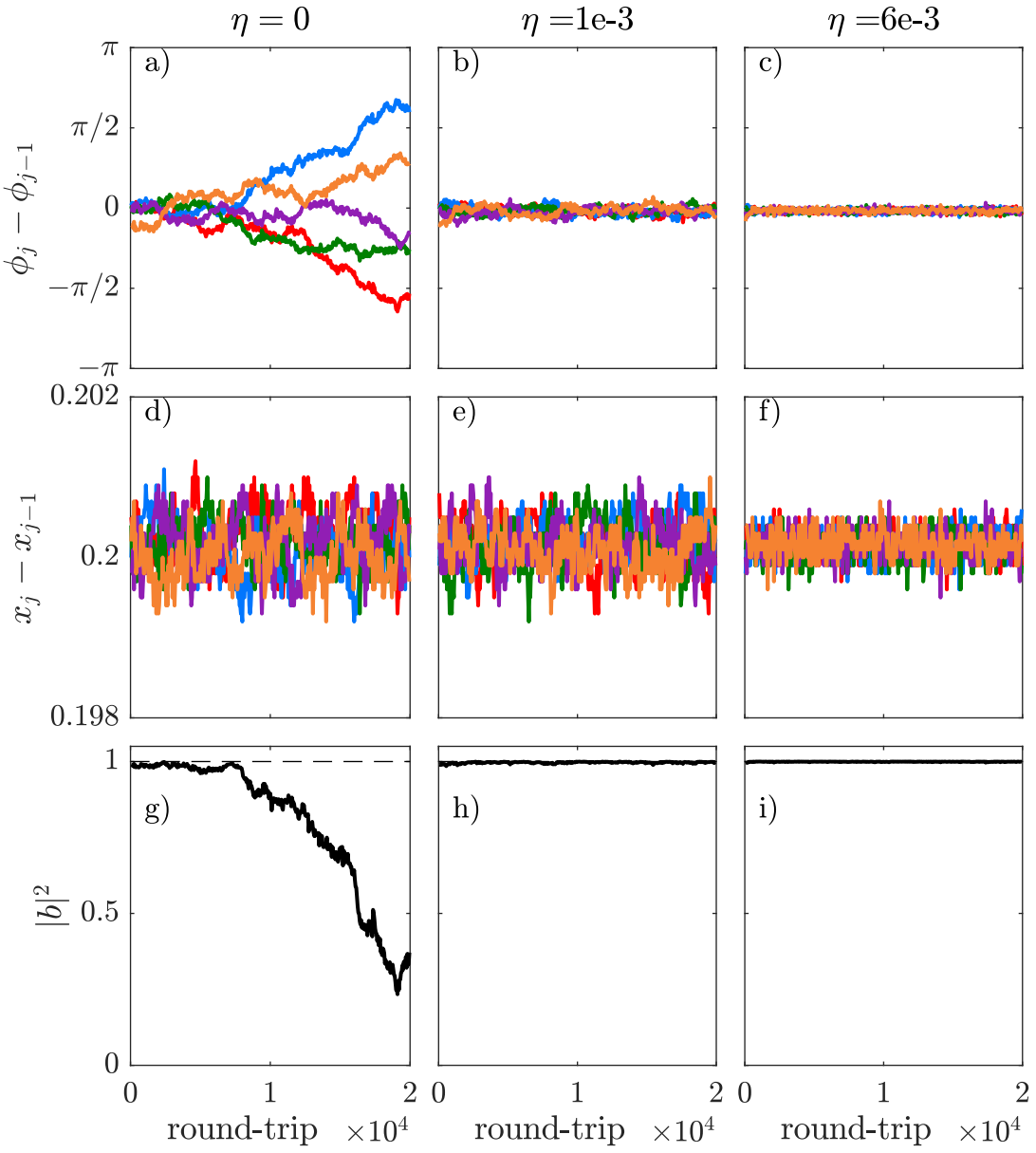

Figure 5.1: Synchronization of a harmonic solution with five pulses for different values of η. The different panels show (first row) the evolution of the relative phase, (second row) the relative position and (third row) the order parameter. Increasing the coupling decreases the fluctuations for all three measures. In the supplementary material in appendix A animations of the time evolution of the phases for each value of η are displayed in form of arrows in the unit circle. The used parameters are $(\alpha_g, \alpha_a, \tau_1, \tau_2, s, g_0, q_0, \sigma) = (1.5, 0.5, 100, 20, 10, 0.027, 0.04, 0.007)$.

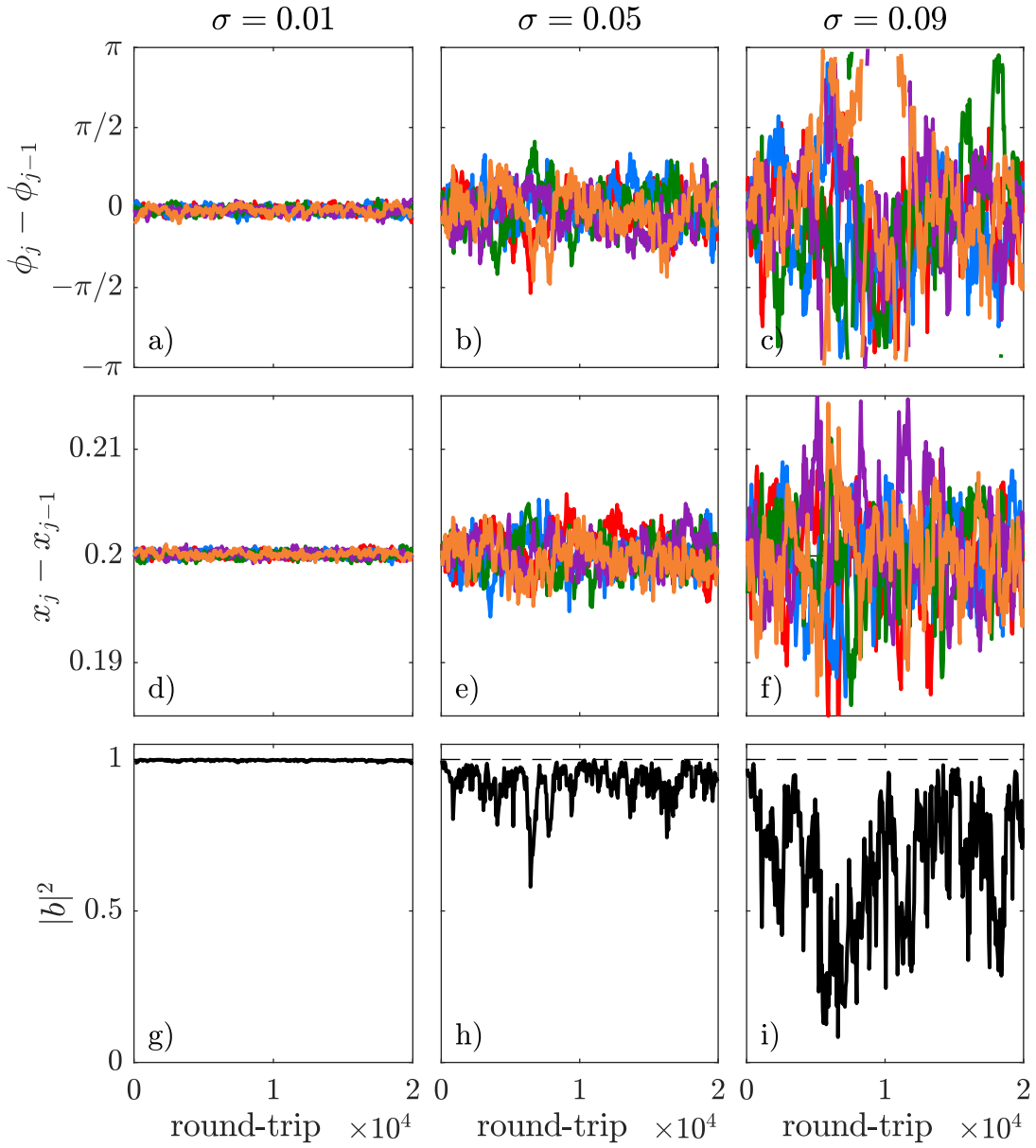

Figure 5.2: Synchronization of a harmonic solution with five pulses for different values of σ, $\eta = 0.002$ and other parameters as in fig. 5.1. The different panels show (first row) the evolution of the relative phase, (second row) the relative position and (third row) the order parameter. In the supplementary material in appendix A animations of the time evolution of the phases for each value of σ are displayed in form of arrows in the unit circle. Increasing the noise increases the fluctuations for all three measures.

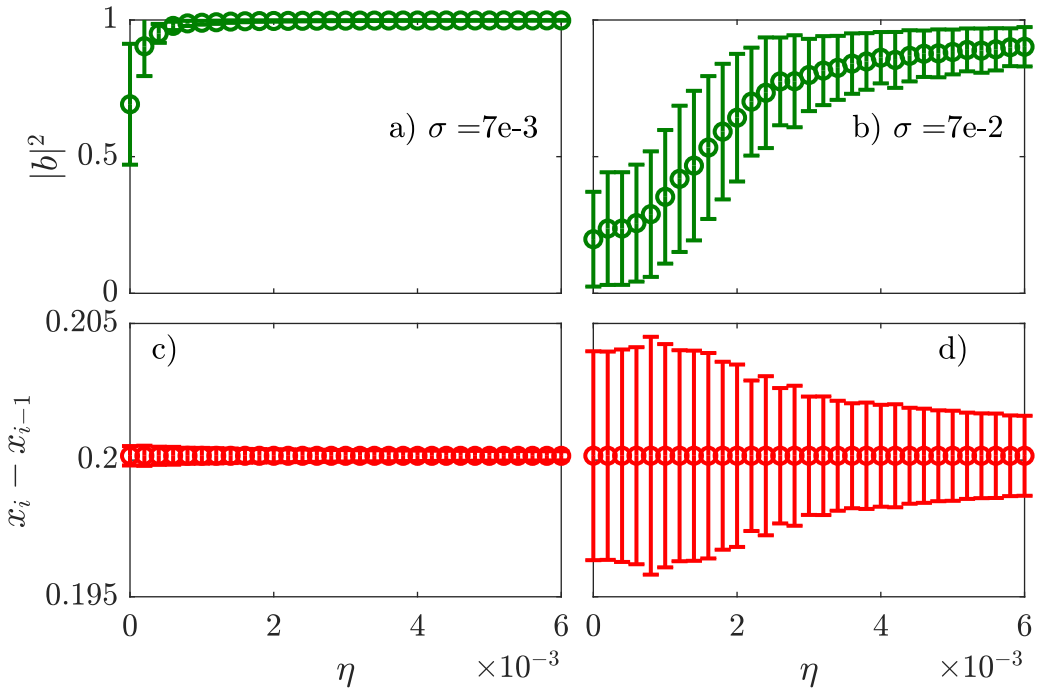

Figure 5.3: Dependence of the order parameter on the feedback rate η for different values of the noise amplitude σ. Other parameters as in fig. 5.1.

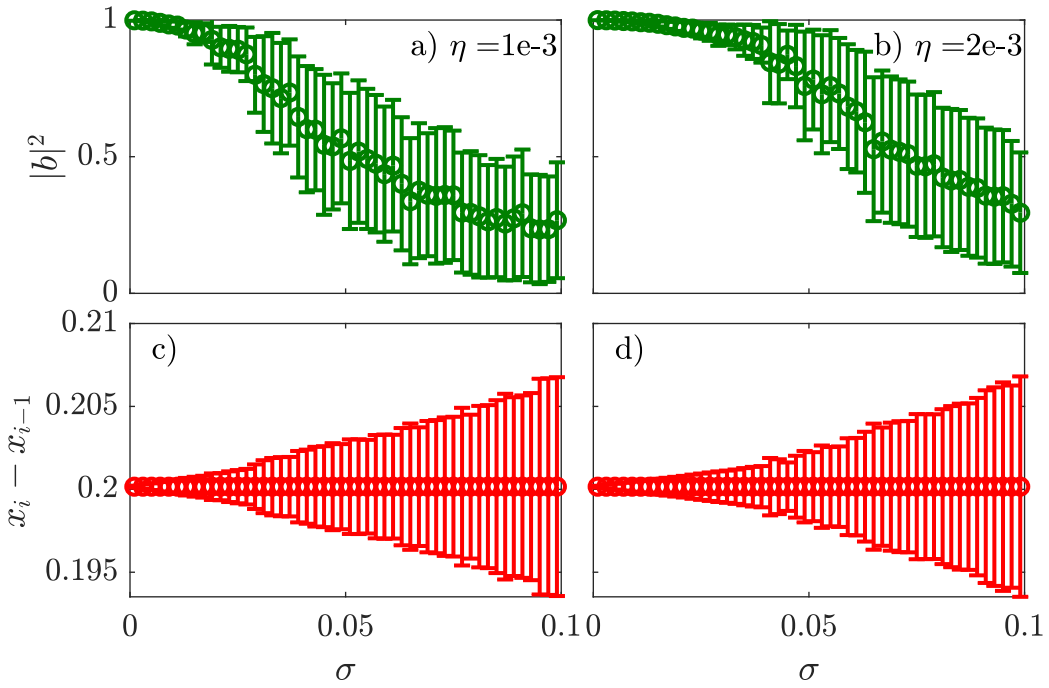

Figure 5.4: Dependence of the order parameter on the noise amplitude σ for different values of the feedback rate η. Other parameters as in fig. 5.1.

5.2.2. Scaling Behavior of the Order Parameter

In section 5.2.1 it is shown that the presence of external feedback can increase the coherence of a train of pulses while more noise leads to less order. Equation 5.20 derived in section 5.1 suggests that the order parameter scales linearly with σ^2 and η^{-2}, respectively, in the vicinity of $|b|^2 = 1$. First, this scaling behavior needs to be verified for the full system and second, one can try to obtain the proportionality constant a introduced in eq. (5.20) from the results.

Figure 5.5 shows the dependence of $|b|^2$ on σ^2 for different values of η. In both cases, a linear relationship can be seen indicated by the orange line representing a linear fit. The fit parameters can be found in table 5.1. Further, the intercept with the ordinate is very close to one which is expected as in a system with no noise and nonzero coupling the coherence between the pulses is expected to be high. This is underlined by the fact that the variance of the order parameter is very small for small noise values. With increasing noise also the variance of the order parameter increases. The last few data points in fig. 5.5a exhibit very large variances and also slightly deviate from the linear behavior. This can be explained by the fact that eq. (5.20) is derived only for values in the vicinity of $|b|^2 = 1$.

The same analysis is conducted for the relationship between $|b|^2$ and η^{-2} and is displayed in fig. 5.6 for different values of σ. The data in figs. 5.6a,b matches the linear fit very well as the noise amplitude in both cases is low. As a consequence even for small couplings ($\eta^{-2} \gtrsim 3 \times 10^5$) high synchronization can be achieved. For large noise values as in fig. 5.6c the linear relationship still holds in the vicinity of $|b|^2 = 1$ and only starts to deviate from it at below around $|b|^2 \approx 0.5$. However, the effect of strong noise can be seen in large variances (note the different scaling of the ordinate compared to fig. 5.6a,b). Another effect of the noise is, that even for large coupling, i.e., η^{-2} small, the pulses are not perfectly coherent which results in the intercept with the ordinate not being one. The fit parameters of all conducted runs are summarized in table 5.1. From the slope, one can also compute the constant a via eq. (5.20). The results show, that the value of a differs between the runs but all values lie in the same order of magnitude. This is particularly significant when comparing the results from fitting σ^2 and η^{-2}, respectively. The statistics might be improved by performing simulations for more round-trips or to perform simulations with more pulses per round-trip. However, in order to show the scaling behavior of the order parameter, these results are sufficient.

Table 5.1: Fit parameters from figs. 5.5 and 5.6 and further runs which are not displayed in this thesis. The fits have the form $|b|^2 = mx + y_0$ where x is either σ^2 or η^{-2}. Note that uncertainties of the order parameter are not considered. In the last column the resulting value for a (see eq. (5.20)) is computed. The intervals indicated by the brackets show in which range the considered values of η and σ lie. The fact that the intercept is not one precisely is neglected when computing the constant a.

η	σ	m	y_0	a
$[5.0 \times 10^{-4}, 6.0 \times 10^{-3}]$	2×10^{-3}	-1.19×10^{-9}	0.9998	7.46×10^{-11}
$[3.8 \times 10^{-4}, 6.0 \times 10^{-3}]$	3×10^{-3}	-1.70×10^{-9}	0.9993	4.73×10^{-11}
$[5.7 \times 10^{-4}, 6.0 \times 10^{-3}]$	3×10^{-3}	-1.43×10^{-9}	0.9996	3.98×10^{-11}
$[6.0 \times 10^{-4}, 6.0 \times 10^{-3}]$	4×10^{-3}	-3.04×10^{-9}	0.9994	4.75×10^{-11}
$[1.1 \times 10^{-3}, 6.0 \times 10^{-3}]$	7×10^{-3}	-9.07×10^{-9}	0.9987	4.63×10^{-11}
1×10^{-3}	$[0, 2.1 \times 10^{-2}]$	-201.73	1.0007	5.04×10^{-11}
2×10^{-3}	$[0, 4.0 \times 10^{-2}]$	-59.31	0.9992	5.93×10^{-11}
3×10^{-3}	$[0, 4.5 \times 10^{-2}]$	-36.17	0.9994	8.14×10^{-11}
3×10^{-3}	$[0, 4.5 \times 10^{-2}]$	-37.60	0.9992	8.46×10^{-11}

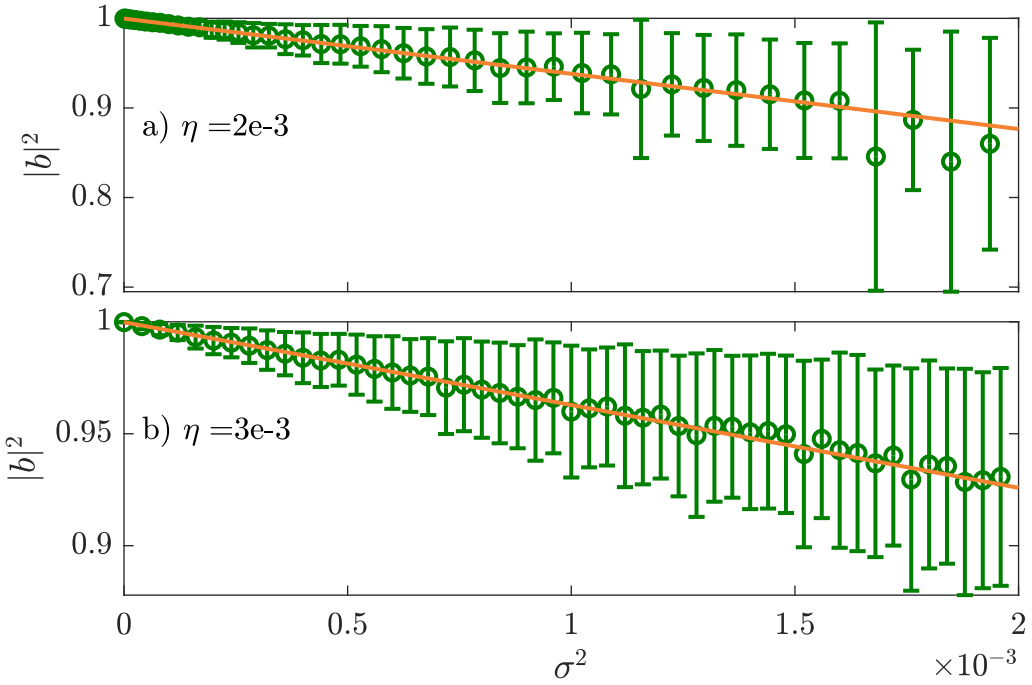

Figure 5.5: A linear dependence can be seen when $|b|^2$ is plotted against σ^2 as suggested by eq. (5.20). The orange line is obtained from a linear fit. The fit parameters can be found in table 5.1. Other parameters as in fig. 5.1.

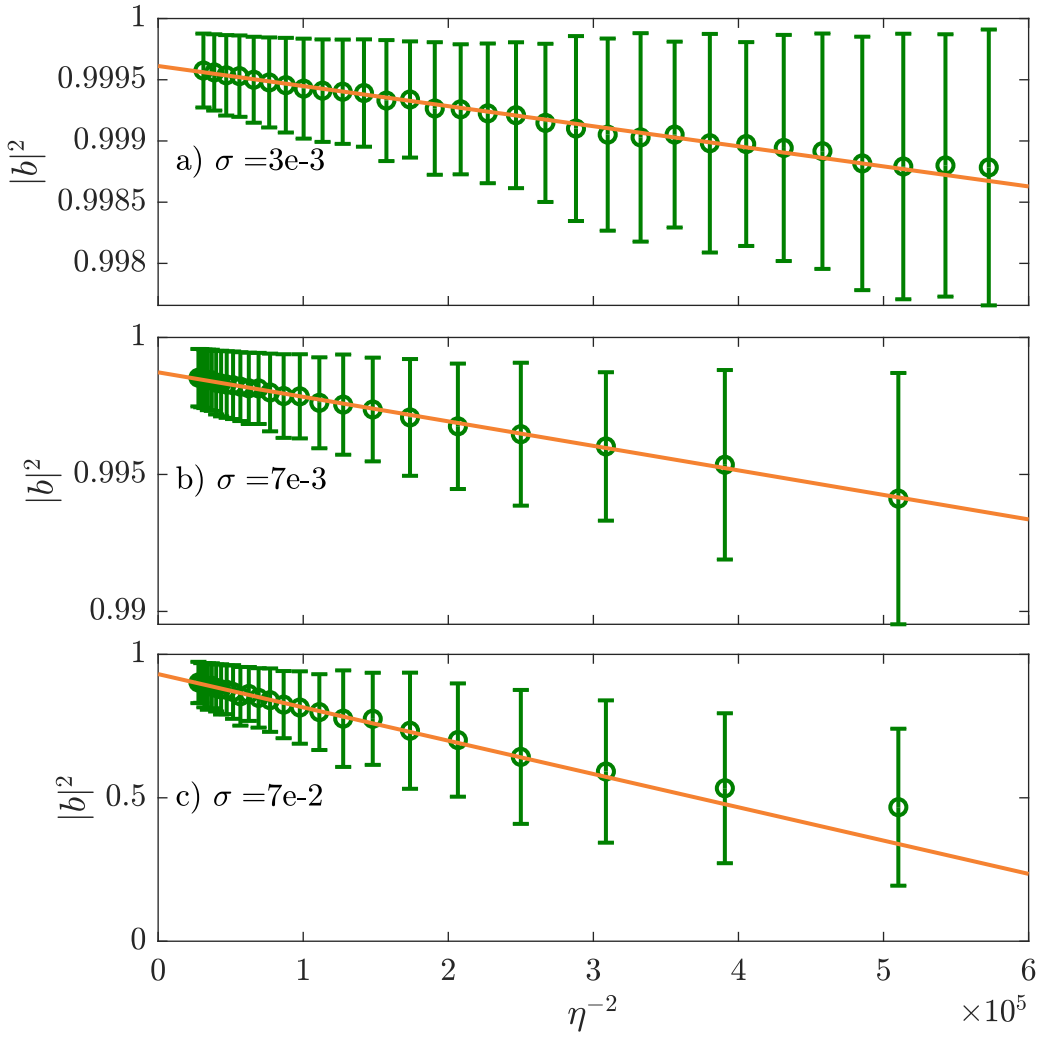

Figure 5.6: A linear dependence can be seen when $|b|^2$ is plotted against η^{-2} as suggested by eq. (5.20). The orange line is obtained from a linear fit. The fit parameters can be found in table 5.1. Other parameters as in fig. 5.1. Note the different scaling of the ordinates, in particular, in panel c) where noise is much stronger than in the other two panels.

5.2.3. Limits of the Simplified Order Parameter Equation

In the previous section the scaling behavior of eq. (5.20) with respect to the coupling strength η and the noise amplitude σ is confirmed. Next, η and σ are kept constant while the number of pulses N and the length of the cavity which corresponds to τ_1 is varied. Here, N and τ_1 need to be varied simultaneously in order to keep $\tau_2 = 20$ constant. Hence, the length of the cavity is $\tau_1 = N \cdot \tau_2$. Figure 5.7 shows the order parameter and the distance between pulses as a function of N. In this case the pulse distance is normalized by subtracting $1/N$, which is the distance of pulses when they are equidistant, in order to see the fluctuations around this theoretical value. The data indicates that despite of the first few data points for $N \lesssim 5$ the order parameter is approximately constant and no dependence on N can be seen. These results stand in contrast to eq. (5.20) which claims that $|b|^2 \propto 1 - \frac{N^4}{L^2}$. On the other hand, one can see the effects of better statistics as for large N the variance of $|b|^2$ becomes smaller. The same applies for the pulse position. For larger N it settles around zero and also its variance becomes negligible.

DNSs of the simplified model presented in eq. (5.5) confirm that the order parameter is independent of the number of pulses in the cavity. The results are shown in fig. 5.8 where simulations for up to 100 000 pulses per round-trip are displayed. As expected, one can see that for larger N the variance of $|b|^2$ decreases. Figure 5.9 shows how the order parameter scales against the noise amplitude and the feedback rate in the simplified model. The results fit to the simulations of the full system in terms of the scaling behavior. The respective diagrams for the full system are displayed in figs. 5.3 and 5.4. A further question is whether the system exhibits a phase transition, i.e., a singularity in the bifurcation diagram. According to the results in fig. 5.9 this is not the case as the curves are smooth for all presented cases.

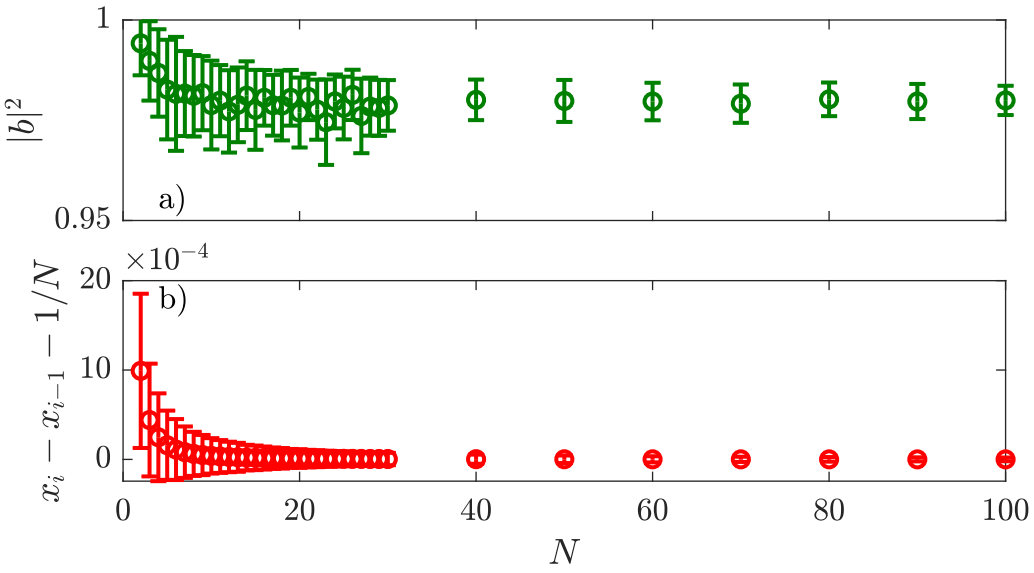

Figure 5.7: Dependence of the order parameter and the distance between pulses on the number of pulses in the cavity for the parameters $\tau_2 = 20, \tau_1 = N \cdot \tau_2, \eta = 0.001, \sigma = 0.01$, other parameters as in fig. 5.1. For the first few data points the order parameter decreases while for $N \gtrsim 5$ the order parameter is approximately constant. At the same time also the pulse distance settles around zero.

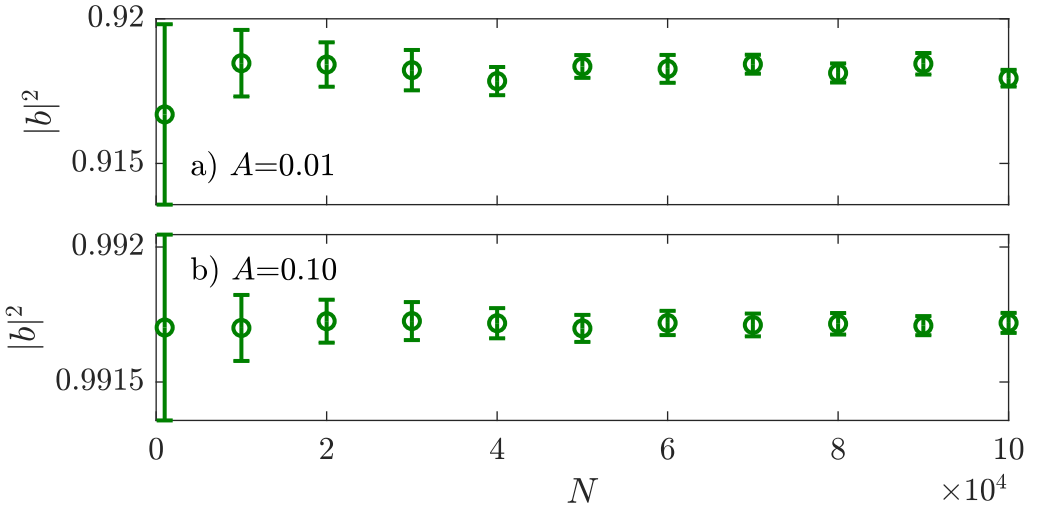

Figure 5.8: Result of DNSs of the simplified model in eq. (5.5) for different values of the coupling A. The order parameter $|b|^2$ defined in eq. (5.2) is plotted against the number of pulses N in the cavity. For each data point a simulation of 2e6 steps with a step size of $h = 0.01$ via an Euler method has been conducted. The value of the order parameter is averaged over the last 2e5 steps of these simulations. The results show that the order parameter is independent of the number of pulses, even for extremely large N.

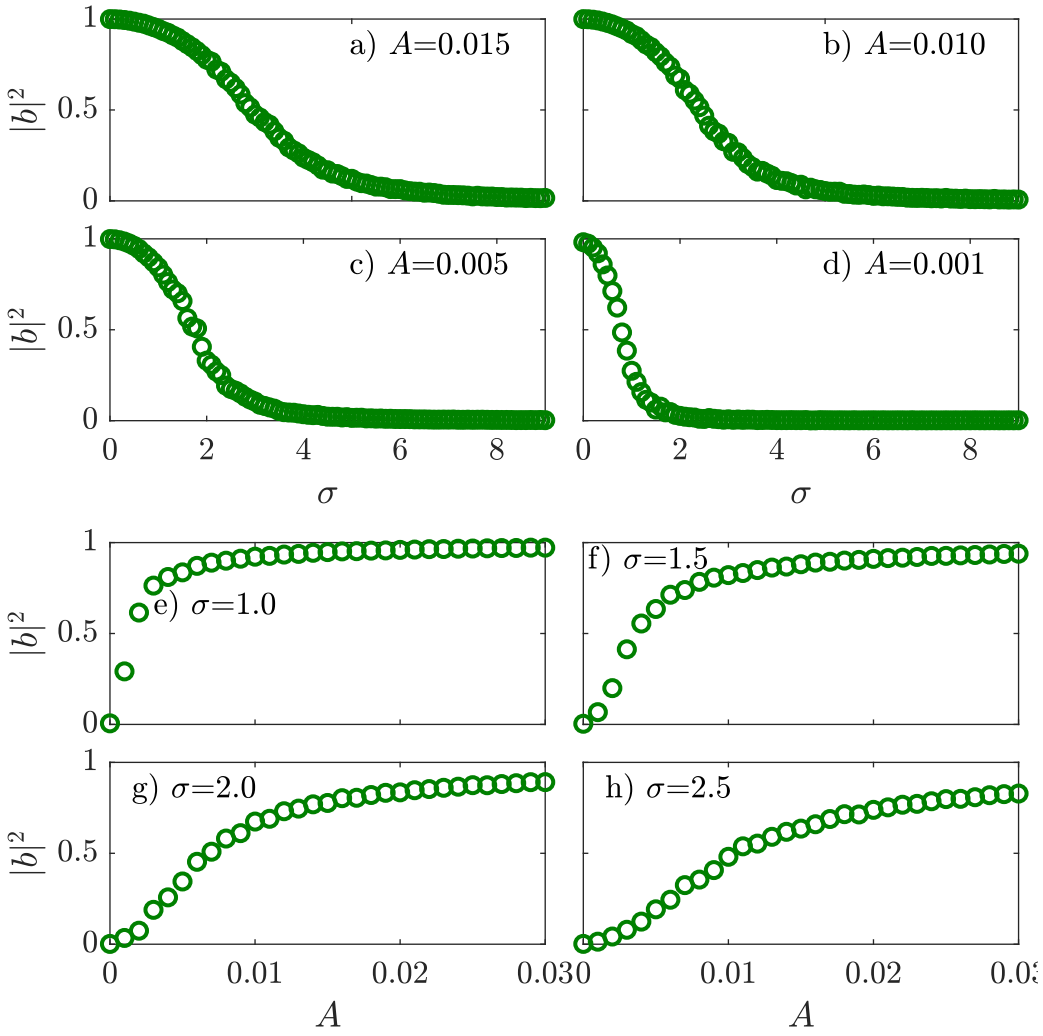

Figure 5.9: Results of DNSs of the simplified model in eq. (5.5) for different values of the coupling A and the noise amplitude σ. The order parameter $|b|^2$ defined in eq. (5.2) is plotted against (a,b,c,d) the amplitude of the added noise and (e,f,g,h) the coupling rate. For each data point a simulation of 5e5 steps with a step size of $h = 0.01$ via an Euler method has been conducted. The value of the order parameter is averaged over the last 2e5 steps of these simulations. The variance is not displayed as it is small. The results fit to DNSs of the full system in fig. 5.4. Further, one can see that no phase transition occurs in the plotted curves as they are smooth and do not exhibit a singularity.

5.2.4. Range of Resonance

So far in this chapter, the feedback is perfectly resonant with the pulses in the sense that $\tau_2 = \tau_1/N$. However, in fig. 4.17 it is shown that the system adapts its period and pulsewidth to slight variations to resonant feedback by generating wider pulses. In this section, DNSs are performed around the resonance in order to analyze the area in which coherent pulses exist, i.e., the range where the system is still able to adapt to non-resonant feedback. This is visualized in fig. 5.10 for a HML_4 solution for two different values of η. The panels show the order parameter on a logarithmic scale, the relative position, the averaged intensity and the respective variances. Each panel has a resolution of 100×100 values for g and τ_2, respectively. First, a preparation run without time delayed feedback is conducted for $g = 1.4$. This creates a stable HML_4 solution with no satellites which will be used as an initial state in the following. Next, this initial state is used and time delayed feedback is turned on at $\tau_2 = 30$. Then the simulations are conducted column-wise, i.e., if a simulation ends on a stable HML_4 solution the endpoint of the simulation is used as the initial state for the next simulation. Otherwise the system is initialized with the state obtained in the preparation run. For each data point a DNSs is conducted for 4000 round-trips. Only the last 2000 round-trips are used to obtain the data to make sure that the system is settled.

In panels i) and ii) one can see the range in which synchronization between pulses occurs. In this range the order parameter is close to one and its variance is small. This only occurs in the vicinity of the resonance. When comparing the results for $\eta = 5\mathrm{e}{-3}$ and $\eta = 10\mathrm{e}{-3}$ it can be observed that for stronger feedback rates also the region in which pulses are coherent is larger.

Panel iii) shows which harmonic solution is favored in which parameter range, i.e., in the dark blue areas no stable pulsed states exist, in the yellow/orange area solutions with one pulse, in the cyan areas solutions with two pulses and in the blue area solutions with four pulses are favored when starting the simulation with four pulses. With the help of panels iv) and vi) one can understand where these solutions are stable. In these regions the variance of the pulse distance and the intensity fluctuations are small. For obvious reasons, the coherent region visible in panel i) is stable but there are further stable regions above and below the resonance. Here, the satellites are too far away from the pulses such that the system cannot adapt to this. In the areas where fluctuations are present pulses

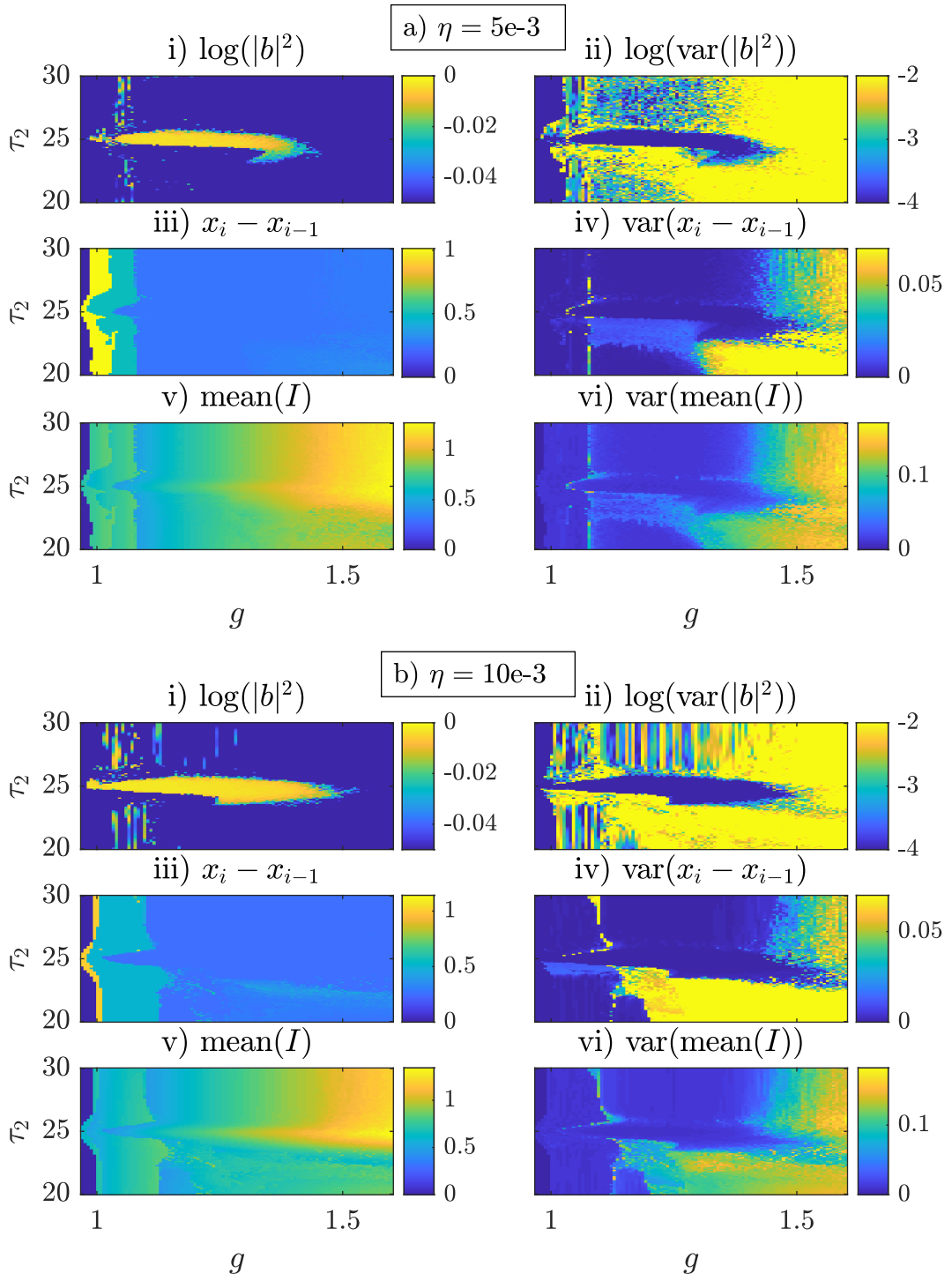

Figure 5.10: Results of DNSs in the (τ_2, g)-plane for different values of η for HML_4 solution. The area around $\tau_2 = \tau_1/4 = 25$ is scanned in order to analyze the influence of resonant feedback. The panels show i) the order parameter (see eq. (5.2), iii) the distance between two pulses and v) the mean intensity of the pulses. Panels ii), iv) and vi) show the according variances. The simulation is conducted column-wise starting at $\tau_2 = 30$. If the system ended on a solution with four pulses the next simulation is continued from that point. Otherwise, the system is initialized with four pulses. Parameters are $(\alpha_g, \alpha_a, \tau_1, s) = (1.5, 0.5, 100, 10)$.

are replaced consecutively by its satellite as shown in fig. 4.4. Combining the information from all panels gives a clear view on where stable harmonic solutions with four pulses exist. In particular, one can see that there is a small range in τ_2 just below the resonance where these solutions are stable. However, this region is not connected to the resonant region. The gap occurs when the satellite is close to the main pulse but not close enough for it to merge with the main pulse. This region is also analyzed via path continuation for a HML_2 solution in fig. 4.16. In figs. 4.16c,d where τ_2 is close but below the resonance for the HML_2 solution one only finds unstable branches. This corresponds to the gap found in fig. 5.10.

6. Conclusion and Outlook

In order to analyze the influence of time delayed feedback on the behavior of temporal LSs in the output of a PML laser, a DDE model with two delays is used. The lasing threshold is analytically calculated for this model. The further analysis consists of two steps. First, a bifurcation analysis of the DDE model is performed and second, it is investigated how resonant feedback can influence the coherence of a train of pulses. For the analysis, a combination of numerical path continuation conducted with the package `DDE-BIFTOOL` and DNSs using a Runge-Kutta-4 or Euler scheme are used.

In the time trace, time delayed feedback becomes visible in form of small satellite pulses for each main pulse. The location of the satellite can be controlled by the length of the delay τ_2 and the size is determined by the feedback rate η. When the satellite is placed sufficiently close to the main pulse, time delayed feedback has a destabilizing influence on the system when increasing the gain. Above the critical gain value where the instability occurs the satellites successively replace the main pulses after a certain pulse lifetime. By analyzing the scaling behavior of the lifetime it is shown that the instability occurs in a SNIPER bifurcation of limit cycles. A similar satellite instability is described in [Sch+20] where the dynamics of passively mode-locked integrated external-cavity surface-emitting lasers (MIXSELs) are analyzed using a first-principle dynamical model based upon delay algebraic equations. Here, third order dispersion stemming from the lasing micro-cavity induces a train of decaying satellites similar to the effects of time delayed feedback discussed in this thesis. Remarkably, the behavior in the (α_g, g)-plane, in particular the instability in a SNIPER bifurcation, is the same for both models.

When introducing noise to the system, it can be excited and the instability can be triggered to occur earlier. In a statistical distribution it is shown that the probability of longer lifetimes decays exponentially. Next, it is analyzed in which regime the global instability exists. Besides the feedback strength the linewidth enhancement factors of the gain and absorber regions – α_g and α_a, respectively – play an important role. Increasing α_a shifts the region of the SNIPER bifurcation towards larger α_g. Finally, harmonic solutions consisting of multiple pulses per round-trip are considered. When applying resonant feedback, i.e., the location of pulse coincide with a satellite, the range of stability of this solution is increased. It is also shown, that around the resonance the pulses

adapt their period, intensity and pulse width in order to include the satellite in the pulse. Furthermore, branches of different solutions are connected around the resonance by period doubling bifurcations. A further type of solution that emerges in this regime consists of multiple pulses which are not equidistant. As a result some satellites coincide with pulses while others are separated. It is found that these solutions are unstable, however, the analysis of these solutions needs further work, especially on how they emerge and in which arrangements they can occur.

It is shown by DNSs that time delayed feedback in the resonant regime can transfer phase information from one pulse to another. While noise destroys the coherence in a train of pulses, increasing the feedback strength counters this effect. To quantify the degree of coherence in a train of pulses, an order parameter is introduced. In a simple model of next-neighbor-coupled oscillators an explicit formula for the order parameter in the vicinity of perfect coherence is deduced. According to this equation, the order parameter depends on the feedback strength, the noise amplitude, the number of pulses in the cavity and the length of the cavity. By performing DNSs the scaling behavior is verified with respect to the feedback strength and the noise amplitude. However, the scaling behavior for the number of pulses can not be verified. This leads to the assumption that the simplified equation for the order parameter does not cover the dynamics of the full system and needs further refinement. When trying to analyze the behavior of the system with respect to the length of the cavity, the added noise often leads to a destruction of the state, especially for very long cavities. Further, the analysis of the scaling behavior is conducted for $N = 5$ pulses. The statistics can be much improved by using more pulses, however, this would come at the cost of increased computation times.

The experimental realization of the presented model is currently worked on. It is analyzed whether the predictions of this thesis such as the satellite instability and the synchronization of pulses hold for a real world system. Further, experimental results that need theoretical explanations might come up in the mean time.

Appendix A Supplementary Material

In the following, a list of figures is presented for which supplementary animations are provided for a better visualization. The animations are stored in a cloud storage and can be accessed via the link `http://uni-muenster.sciebo.de/s/1EcD1uOMkGYlueL`.

- Figure 4.3
- Figure 4.4
- Figure 4.16
- Figure 4.17
- Figure 5.1
- Figure 5.2

References

[AA05] Nail Akhmediev and Adrian Ankiewicz. *Dissipative Solitons*. Springer, 2005.

[AO89] Govind P. Agrawal and Nils A. Olsson. "Amplification and compression of weak picosecond optical pulses by using semiconductor-laser amplifiers". In: *Opt. Lett.* 14.10 (May 1989), pp. 500–502. DOI: 10.1364/OL.14.000500.

[AP01] Yuri Astrov and Hans-Georg Purwins. "Plasma spots in a gas discharge system: Birth, scattering and formation of molecules". In: *Physics Letters A* 283 (May 2001), pp. 349–354. DOI: 10.1016/S0375-9601(01)00257-2.

[Arg+15] John Argyris, Gunter Faust, Maria Haase, and Rudolf Friedrich. *An Exploration of Dynamical Systems and Chaos*. Springer, 2015.

[Bim+06] D. Bimberg, G. Fiol, M. Kuntz, C. Meuer, M. Lämmlin, N. N. Ledentsov, and A. R. Kovsh. "High speed nanophotonic devices based on quantum dots". In: *physica status solidi (a)* 203.14 (2006), pp. 3523–3532. DOI: 10.1002/pssa.200622488.

[Der+92] Dennis J. Derickson, Roger J. Helkey, Alan Mar, Judy R. Karin, John G. Wasserbauer, and John E. Bowers. "Short pulse generation using multisegment mode-locked semiconductor lasers". In: *IEEE Journal of Quantum Electronics* 28.10 (1992), pp. 2186–2202.

[DHA91] Peter J. Delfyett, Davis H. Hartman, and S. Zuber Ahmad. "Optical clock distribution using a mode-locked semiconductor laser diode system". In: *Journal of Lightwave Technology* 9.12 (1991), pp. 1646–1649.

[ELR02] Koen Engelborghs, Tatyana Luzyanina, and Dirk Roose. "Numerical bifurcation analysis of delay differential equations using DDE-BIFTOOL". In: *ACM Transactions and Mathamatical Software* 28 (1) (2002), pp. 1–21.

[GA12] Philippe Grelu and Nail Akhmediev. "Dissipative solitons for mode-locked lasers". In: *Nature Photonics* 6 (Feb. 2012), pp. 84–92. DOI: 10.1038/nphoton.2011.345.

[GH83] John Guckenheimer and Philip Holmes. *Nonlinear Oscillations, Dynamical Systems, and Bifurcations of Vector Fields*. Applied mathematical sciences. Springer, 1983. ISBN: 9787506212830.

[Gur18] Svetlana Gurevich. *Runge-Kutta methods*. Lecture on numerical methods for complex systems. 2018. URL: https://www.uni-muenster.de/Physik.TP/teaching/courses/numerical_methods_for_complex_systems_ii_ss2018.html.

[Hal77] Jacl K. Hale. *Theory of Functional Differential Equations*. Applied Mathematical Sciences. Springer, 1977. ISBN: 9780387902036.

[Hau00] Hermann A. Haus. "Mode-locking of lasers". In: *IEEE Journal of Selected Topics in Quantum Electronics* 6.6 (2000), pp. 1173–1185.

[Hau75] Hermann A. Haus. "Theory of mode locking with a slow saturable absorber". In: *IEEE Journal of Quantum Electronics* 11.9 (Sept. 1975), pp. 736–746. ISSN: 1558-1713. DOI: 10.1109/JQE.1975.1068922.

[Jau16] Lina Jaurigue. "Dynamics and stochastic properties of passively mode-locked semiconductor lasers subject to optical feedback". Doctoral Thesis. Berlin: Technische Universität Berlin, 2016. DOI: 10.14279/depositonce-5543.

[Jav+07] Julien Javaloyes, Josep Mulet, Massimo Giudici, and Salvador Balle. "Passive mode-locking of lasers by crossed-polarization gain modulation". In: *2007 European Conference on Lasers and Electro-Optics and the International Quantum Electronics Conference*. 2007. URL: http://www.osapublishing.org/abstract.cfm?URI=CLEO_Europe-2007-CB13_6.

[Jav+16] Julien Javaloyes, Patrice Camelin, Mathias Marconi, and Massimo Giudici. "Dynamics of Localized Structures in Systems with Broken Parity Symmetry". In: *Phys. Rev. Lett.* 116 (13 Mar. 2016), p. 133901. DOI: 10.1103/PhysRevLett.116.133901.

[Jus+00] Wolfram Just, Ekkehard Reibold, Krzysztof Kacperski, Piotr Fronczak, Janusz Hołyst, and Hartmut Benner. "Influence of stable Floquet exponents on time-delayed feedback control". In: *Physical review. E, Statistical physics, plasmas, fluids, and related interdisciplinary topics* 61 (June 2000), pp. 5045–56. DOI: 10.1103/PhysRevE.61.5045.

[Kel03] Ursula Keller. "Keller, U. Recent developments in compact ultrafast lasers. Nature 424, 831-838". In: *Nature* 424 (Sept. 2003), pp. 831–8. DOI: 10.1038/nature01938.

[Kun+07] M. Kuntz, G. Fiol, M. Laemmlin, C. Meuer, and D. Bimberg. "High-Speed Mode-Locked Quantum-Dot Lasers and Optical Amplifiers". In: *Proceedings of the IEEE* 95.9 (2007), pp. 1767–1778.

[Kur75] Yoshiki Kuramoto. "Self-entrainment of a population of coupled non-linear oscillators". In: *Lecture Notes Physics* 39 (1975). Ed. by Huzihiro Araki, pp. 420–422. DOI: 10.1007/BFb0013365.

[LK80] R. Lang and K. Kobayashi. "External optical feedback effects on semiconductor injection laser properties". In: *IEEE Journal of Quantum Electronics* 16.3 (1980), pp. 347–355.

[LK93] Werner Lauterborn and Martin Kurz Thomas Wiesenfeldt. *Kohärente Optik – Grundlagen für Physiker und Ingenieure*. Springer, 1993.

[Loe+96] F. H. Loesel, M. H. Niemz, J. F. Bille, and T. Juhasz. "Laser-induced optical breakdown on hard and soft tissues and its dependence on the pulse duration: experiment and model". In: *IEEE Journal of Quantum Electronics* 32.10 (1996), pp. 1717–1722.

[LWY11] Mark Lichtner, Matthias Wolfrum, and Serhiy Yanchuk. "The Spectrum of Delay Differential Equations with Large Delay". In: *SIAM J. Math. Analysis* 43 (Jan. 2011), pp. 788–802. DOI: 10.1137/090766796.

[Mad+19] L. Madail, S. Flannigan, A. M. Marques, A. J. Daley, and R. G. Dias. "Enhanced localization and protection of topological edge states due to geometric frustration". In: *Phys. Rev. B* 100 (12 Sept. 2019), p. 125123. DOI: 10.1103/PhysRevB.100.125123.

[Mar+14] Mathias Marconi, Julien Javaloyes, Salvador Balle, and Massimo Giudici. "How Lasing Localized Structures Evolve out of Passive Mode Locking". In: *Phys. Rev. Lett.* 112 (22 June 2014), p. 223901. DOI: 10.1103/PhysRevLett.112.223901.

[Mer+04] Ehud Meron, Erez Gilad, Jost von Hardenberg, Moshe Shachak, and Yair Zarmi. "Vegetation patterns along a rainfall gradient". In: *Chaos, Solitons & Fractals* 19.2 (2004). Fractals in Geophysics, pp. 367–376. ISSN: 0960-0779. DOI: 10.1016/S0960-0779(03)00049-3.

[MFS87] Elisha Moses, Jay Fineberg, and Victor Steinberg. “Multistability and confined traveling-wave patterns in a convecting binary mixture”. In: *Physical review. A* 35 (Apr. 1987), pp. 2757–2760. DOI: 10.1103/PhysRevA.35.2757.

[New74] Geoff New. “Pulse evolution in mode-locked quasi-continuous lasers”. In: *IEEE Journal of Quantum Electronics* 10.2 (1974), pp. 115–124.

[Nie+92] F.-J. Niedernostheide, M. Arps, R. Dohmen, H. Willebrand, and H.-G. Purwins. “Spatial and Spatio-Temporal Patterns in pnpn Semiconductor Devices”. In: *physica status solidi (b)* 172.1 (1992), pp. 249–266. DOI: 10.1002/pssb.2221720123.

[Pes+04] M. Pesch, E. Westhoff, T. Ackemann, and W. Lange. “Vectorial solitons, higher-order localized states and compound states in a single-mirror feedback system”. In: *InternationalQuantum Electronics Conference, 2004. (IQEC).* 2004, pp. 155–156.

[PRK01] Aarkady Pikovsky, Michael G. Rosenblum, and Jürgen Kurths. *Synchronization, A Universal Concept in Nonlinear Sciences*. Cambridge University Press, 2001.

[RP04] Michael Rosenblum and Arkady Pikovsky. “Delayed feedback control of collective synchrony: An approach to suppression of pathological brain rhythms”. In: *Physical review. E, Statistical, nonlinear, and soft matter physics* 70 (Nov. 2004), p. 041904. DOI: 10.1103/PhysRevE.70.041904.

[Sch+20] Christian Schelte, Denis Hessel, Julien Javaloyes, and Svetlana V. Gurevich. “Dispersive Instabilities in Passively Mode-Locked Integrated External-Cavity Surface-Emitting Lasers”. In: *Phys. Rev. Applied* 13 (5 May 2020), p. 054050. DOI: 10.1103/PhysRevApplied.13.054050.

[Sei+20] Thomas G. Seidel, Auro M. Perego, Julien Javaloyes, and Svetlana V. Gurevich. “Discrete light bullets in passively mode-locked semiconductor lasers”. In: *Chaos: An Interdisciplinary Journal of Nonlinear Science* 30.6 (2020), p. 063102. DOI: 10.1063/5.0002989.

[Sie+14] Jan Sieber, Koen Engelborghs, Tatyana Luzyanina, Giovanni Samaey, and Dirk Roose. "DDE-BIFTOOL Manual - Bifurcation analysis of delay differential equations". In: (July 2014). URL: http://arxiv.org/abs/1406.7144.

[SJG18] Chrsitian Schelte, Julien. Javaloyes, and Svetlana V. Gurevich. "Dynamics of temporally localized states in passively mode-locked semiconductor lasers". In: *Phys. Rev. A* 97 (5 May 2018), p. 053820. DOI: 10.1103/PhysRevA.97.053820.

[SKH16] Eckehard Schöll, Sabine H. L. Klapp, and Philipp Hövel. *Control of Self-Organizing Nonlinear Systems*. Springer, 2016.

[SL93] O. Solgaard and K. Y. Lau. "Optical feedback stabilization of the intensity oscillations in ultrahigh-frequency passively modelocked monolithic quantum-well lasers". In: *IEEE Photonics Technology Letters* 5.11 (1993), pp. 1264–1267.

[Str94] Steven H. Strogatz. *Nonlinear Dynamics and Chaos*. 1994.

[TEK88] R. S. Tucker, G. Eisenstein, and S. K. Korotky. "Optical time-division multiplexing for very high bit-rate transmission". In: *Journal of Lightwave Technology* 6.11 (1988), pp. 1737–1749.

[Thi17] Uwe Thiele. *Numerical Continuation - A step by step introduction Prelude to the Münsteranian Torturials*. 2017. URL: http://www.uni-muenster.de/CeNoS/Lehre/Tutorials/continuation.html.

[Thi18] Uwe Thiele. *Dynamical Systems*. Lecture on Theoretical Nonliniear Physics I. 2018. URL: https://www.uni-muenster.de/Physik.TP/teaching/courses/theoretical_nonlinear_physics_i_ws2018-2019.html.

[TLO94] B. Tromborg, H. E. Lassen, and H. Olesen. "Traveling wave analysis of semiconductor lasers: modulation responses, mode stability and quantum mechanical treatment of noise spectra". In: *IEEE Journal of Quantum Electronics* 30.4 (1994), pp. 939–956.

[UHH02] Thomas Udem, Ronald Holzwarth, and Theodor Haensch. "Optical Frequency Metrology". In: *Nature* 416 (Apr. 2002), pp. 233–7. DOI: 10.1038/416233a.

[UMS96] P. B. Umbanhowar, F. Melo, and H. L. Swinney. “Localized excitations in a vertically vibrated granular layer”. In: *Nature* 382 (Jan. 1996), pp. 793–796. DOI: 10.1038/382793a0.

[VT05] Andrei G. Vladimirov and Dmitry Turaev. “Model for passive mode locking in semiconductor lasers”. In: *Phys. Rev. A* 72 (3 Sept. 2005), p. 033808. DOI: 10.1103/PhysRevA.72.033808.

[WKR84] Junru Wu, Robert Keolian, and Isadore Rudnick. “Observation of a Nonpropagating Hydrodynamic Soliton”. In: *Phys. Rev. Lett.* 52 (16 Apr. 1984), pp. 1421–1424. DOI: 10.1103/PhysRevLett.52.1421.

[YG14] Serhiy Yanchuk and Giovanni Giacomelli. “Pattern Formation in Systems with Multiple Delayed Feedbacks”. In: *Physical review letters* 112 (Mar. 2014). DOI: 10.1103/PhysRevLett.112.174103.

[YG17] Serhiy Yanchuk and Giovanni Giacomelli. “Spatio-temporal phenomena in complex systems with time delays”. In: *Journal of Physics A: Mathematical and Theoretical* 50 (Mar. 2017), p. 103001. DOI: 10.1088/1751-8121/50/10/103001.

Declaration of Academic Integrity

Hereby, I confirm that this thesis on *Influence of time delayed feedback on the dynamics of temporal localized structures* is solely my own work and that I have used no sources or aids other than the ones stated. All passages in my thesis for which other sources, including electronic media, have been used, be it direct quotes or content references, have been acknowledged as such and the sources cited.

Münster, September 14, 2020 _____

Thomas Seidel

I agree to have my thesis checked in order to rule out potential similarities with other works and to have my thesis stored in a database for this purpose.

Münster, September 14, 2020 _____

Thomas Seidel